Search for Physics beyond the Standard Model in Events with a Z Boson and Missing Transverse Momentum in pp Collisions at $\sqrt{s} = 13$ TeV

Kota Kasahara

February 2017

Search for Physics beyond the Standard Model in Events with a Z Boson and Missing Transverse Momentum in pp Collisions at $\sqrt{s} = 13$ TeV

Kota Kasahara
Doctoral Program in Physics

Submitted to the Graduate School of
Pure and Applied Sciences
in Particle Fulfillment of the Requirements
for the Degree of Doctor of Philosophy in
Science

at the
University of Tsukuba

Abstract

We have searched for physics beyond the standard model of elementary particles in proton-proton collisions with a final state containing a Z boson and invisible particles. In 2012, a new particle was discovered at a mass of 125 GeV/c^2 by the ATLAS and CMS experiments at the CERN Large Hadron Collider (LHC). Subsequent measurements have shown that the particle possesses the properties consistent with the Higgs particle predicted by the standard model. However, it remains to be seen whether it indeed is *the* Higgs particle of the standard model.

The standard model has been highly successful in explaining almost all experimental results. However, few think it is the ultimate theory of elementary particles, and it is generally believed that at least some kind of extension is necessary. For example, we know dark matter exists in the universe, but we do not know its particle nature, or the standard model does not account for it. Theoretically, many are unsatisfied with the fact that the electroweak scale is 10^{16} times smaller than the Planck scale, which leads to an enormous quantum corrections to the Higgs boson mass due to virtual particles in the loop. One of the urgent tasks of experimental particle physics after the Higgs boson discovery is to obtain a clue to possible extensions of the standard model and to search for new particles and phenomena.

At the LHC experiments, dark matter particles cannot be directly detected. However, they can be inferred from a momentum imbalance measured in the plane transverse to the beam axis. We call it the "missing transverse momentum". The missing transverse momentum can also be used to infer neutrinos, which do not leave detectable signals in the detector, either. Searches using the Z boson and the missing transverse momentum in the final state have clean signature with relatively low background, and provide a means to address comprehensively the issues mentioned above. To be specific, we have performed the following three searches: (1) new heavy particle resonances decaying to the $ZZ \to \ell\ell\nu\nu$ final state; (2) the decay of the 125 GeV/c^2 Higgs boson to invisible particles in the production channel $pp \to ZH$ with $Z \to \ell\ell$; and (3) production of dark matter particles in association with a Z boson with $Z \to \ell\ell$. The ZZ transverse mass distribution is examined in search (1), while the missing transverse momentum distributions are examined in searches (2) and (3).

The analysis has been performed using proton-proton collisions at a center-of-mass energy of 13 TeV corresponding to an integrated luminosity of 13.3 fb^{-1} collected with the ATLAS detector at the LHC. No significant deviations from the standard model expectations are observed. We thus have placed constraints on new physics effects. For the new heavy resonance search, we have set upper limits on the production cross section of a bulk Randall-Sumdrum graviton, and the masses smaller than 1.03 TeV are excluded at the 95% confidence level (CL). An upper limit is also set on the branching fraction of the Higgs boson decays to invisible particles to be 98.2% at the 95% CL. Finally exclusion limits are placed on the dark matter production through a vector mediator in a 2-dimensional phase space of dark matter and mediator masses.

Acknowledgements

I would like to thank all people who have supported my research and give me an opportunity for growth during the Ph.D program. I could not execute my research without their helps.

First of all, I would like to convey my gratitude to Prof. Fumihiko Ukegawa and Prof. Shinhong Kim. They gave me much advice on physics and provided me an opportunity to work at CERN. I would also like to express appreciation to Prof. Hideki Okawa. He introduced me to the ATLAS $\ell\ell + inv.$ group and strongly supported my analysis. I can not carry out all my achievements without your helps. I also would like to thank Prof. Kazuhiko Hara and Prof. Koji Sato. They gave me very useful comments to progress my study, and helped me when I was in a pinch. I also would like to express my appreciation for Prof. Yuji Takeuchi. He always greatly encouraged me and made me grow as a scientist.

I would like to thank HEP tsukuba members, Kenji Kiuchi, Rysouke Fuchi, Kazuki Nagata, Fumiaki Ito, Takuya Okudaira, Shunsuke Honda, Mutsuto Hagihara, Shunsuke Yagi, Daisuke Sekigawa, Endo Shun and Rena Wakasa. I talked to them about my worries, and they always gave me advice. I will not forget the days which we spent with you.

I also would like to thank all people who I met in CERN. Masato Aoki supported me during my work on the muon trigger signature group. I spent fun time and painful time with my office colleagues, Naoki Kimura, Takashi Mitani, Tomoya Izawa and Toshiaki Kaji.

ATLAS $\ell\ell + inv.$ group gave a lot of advice. I would like to express gratitude to all the ATLAS $\ell\ell + inv.$ group members : G.Artoni, D.Axen, A.Basalaev, E.Benhar, D.Bortoletto, R. Di Nardo, A.Elliot, O.Fedin, C.Geng, W.Guo, K.Hamano, S.Heim, R.Keeler, M.Lefebvre, B.Liu, V.Maleev, R.Mazini, K.McLean, R.McPherson, J.Meyer, E.Mountricha, I.Naryshkin, H.Okawa, M.Petrov, G.Sabato, I.Shipsey, M.Trovatelli, L.Vigani, Y.Wu, B.Zhou. I am really glad to have been able to work together with you.

Finally, I would like to thank my parents and my sister. They always encouraged me greatly.

Contents

List of Figures

List of Tables

Chapter 1

Introduction

Particle physics describes fundamental structure of matter. The Standard Model has been believed to be the best model in particle physics for more than forty years, and continuously confirmed by many experiments. In 2012, a Higgs boson, the last missing piece of the standard model, was discovered in the ATLAS and CMS experiments [2, 3].

However, the experimental facts and the unnatural issues, which can not be explained by the Standard Model, exist, e.g. the existence of dark matter and the hierarchy problem. The hierarchy problem is the question that asks why the electroweak scale is 10^{16} times smaller than the Planck scale, and enormous quantum corrections are in effect on the Higgs boson mass from the virtual effects. Therefore, the Standard Model has a potential to be extended to describe such mysteries. One of the next biggest tasks of experimental particle physics is to obtain a clue to the extension of Standard Model to explain these experimental facts and unnatural points.

This thesis reports the results of searches for physics beyond the Standard Model using a Z boson and invisible particle final states obtained by the ATLAS detector in pp collisions at $\sqrt{s} = 13$ TeV. Invisible particle means a particle which can not be detected with the detector. The Z boson and invisible particle final state has a relationship to various new physics models, and can shed light on the existence of dark matter and the hierarchy problem. The following sections briefly describe the theoretical and experimental background and the targets of these searches.

1.1 The Standard Model

This world consists of fermions, gauge bosons and the Higgs boson. The gauge bosons, which have integer spin in unit of $\hbar$ and follow the Bose-Einstein statistics, mediate the interactions between particles. Fermions, which have half-integer spin and are governed by the Fermi-Dirac statistics, constitute matter. The Higgs boson, which is a spin-0 particle, gives masses to all the particles.

The list of observed particles is shown in Figure 1.1. Three kinds of gauge bosons carry different interactions respectively. The photon carries the electromagnetic force and couples to all particles which have electromagnetic charge. The gluon is the mediator of the strong interaction, and couples to all particles which have color charge. Since the gluon also has color charge, it can interact with itself. The $W^{\pm}$ and Z bosons mediate the weak interaction. They have large masses, while the photon and the gluon have zero mass. The $W^{\pm}$ boson has the electromagnetic charges of ± 1, and carries the weak charged current. The Z boson does not have the electromagnetic charge, and carries the weak neutral current. The fermions are grouped into quarks and leptons, and come in three generations. The first generation particles constitute ordinary matter, namely the proton and the neutron. The second and third generation particles have higher masses than the first generation particles and are not stable decaying into first generation particles. The quarks feel the strong interaction due to having a color charge in addition to the electromagnetic charge. However, the leptons do not have a color charge.

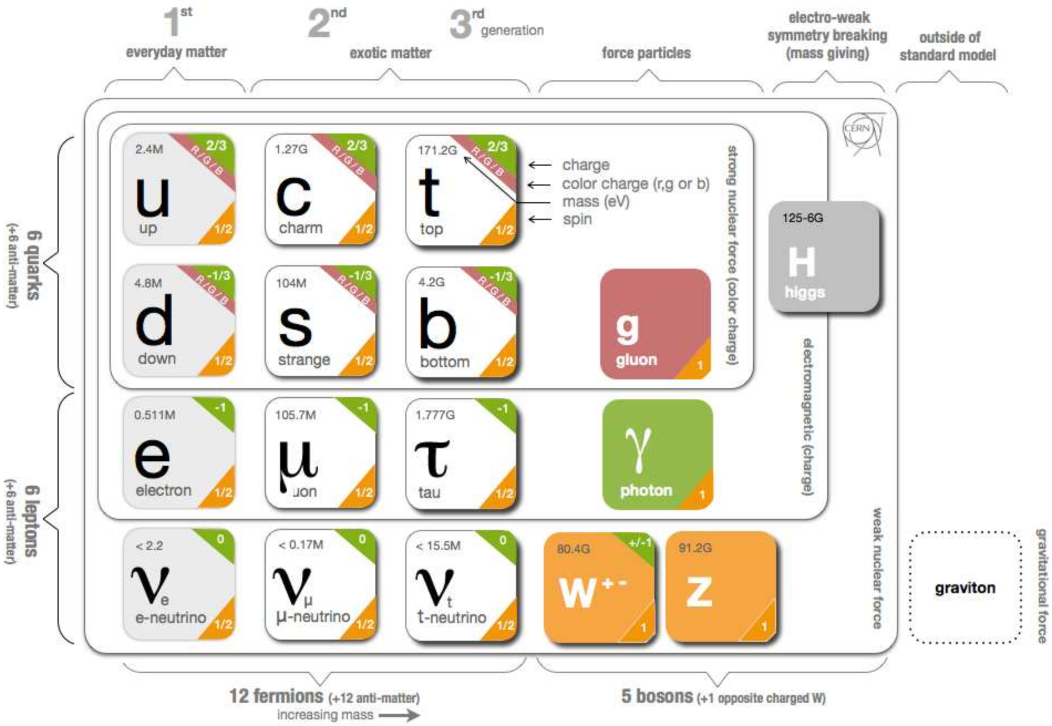

Figure 1.1: List of observed particles[1].

The Standard Model is a gauge theory based on the symmetry group $SU(3)_C \times SU(2)_L \times U(1)_Y$, and describes the interactions between quarks and leptons via the force carriers. The Standard Model is based on the Glashow-Weinberg-Salam electroweak theory in $SU(2)_L \times U(1)_Y$ and the QCD gauge theory in $SU(3)_C$. The Glashow-Weinberg-Salam electroweak theory unifies the electromagnetic and weak interactions. The QCD gauge theory describes the strong interaction among quarks. The electroweak gauge symmetry $(SU(2)_L \times U(1)_Y)$ is broken spontaneously to the electromagnetic subgroup $(U(1)_{\mathrm{em}})$. The following subsections describe the Standard Model in more detail.

1.1.1 An Abelian gauge theory

The theory of the electromagnetic interaction is called Quantum Electrodynamics, and is an Abelian gauge theory with the symmetry group U(1). This section describes the Abelian gauge theory.

The Lagrangian of the free Dirac fermion is written as

$$\mathcal{L}_0 = i\bar{\psi}(x)\gamma^\mu\partial_\mu\psi(x) - m\bar{\psi}(x)\psi(x), \tag{1.1}$$

where ψ is a bi-spinor field of the fermion and m is the fermion mass. Here let us consider the Lagrangian under the U(1) gauge transformation

$$\psi(x) \to \psi'(x) = e^{i\alpha(x)}\psi(x), \tag{1.2}$$

where α is a function of $x = (t, \vec{r})$. This transformation is a phase shift, and is classed as a one-dimensional unitary transformation U(1). The Lagrangian is not invariant under the above gauge transformation due to the additional term $i\partial_\mu\alpha(x)$. A new spin-1 field $A_\mu(x)$ is introduced to keep the gauge invariance. Then new Lagrangian is written as follows :

$$\begin{aligned}
\mathcal{L} &= i\bar{\psi}(x)\gamma^\mu D_\mu\psi(x) - m\bar{\psi}(x)\psi(x) && (1.3)\\
&= i\bar{\psi}(x)\gamma^\mu(\partial_\mu + ieA_\mu(x))\psi(x) - m\bar{\psi}(x)\psi(x) && (1.4)\\
D_\mu &= \partial_\mu + ieA_\mu(x), && (1.5)
\end{aligned}$$

and A_μ is also transformed under the gauge transformation as follows :

$$A_\mu \to A'_\mu(x) = A_\mu - \frac{1}{e}\partial_\mu\alpha(x). \tag{1.6}$$

Adding the new fields, the Lagrangian becomes

$$\mathcal{L} = \mathcal{L}_0 - eA_\mu(x)\bar{\psi}(x)\gamma^\mu\psi(x). \tag{1.7}$$

The Lagrangian is now an invariant under the U(1) gauge transformation since the additional term $i\partial_\mu \alpha(x)$ is canceled. Here, the new interaction term in Eq. (1.7) is written as $-j^\mu A_\mu$, where j^μ is the Noether current.

Furthermore the kinetic term of the gauge field A_μ should be added to the Lagrangian. The kinetic term should be also formed to be the gauge invariant under the U(1) gauge transformation. The kinetic term of the gauge field can be written as

$$\mathcal{L}_{\text{Kinetic}} = -\frac{1}{4} F_{\mu\nu}(x) F^{\mu\nu}(x), \tag{1.8}$$

where $F_{\mu\nu} = \partial_\mu A_\nu - \partial_\nu A_\mu$ is the gauge field strength tensor. The Lagrangian is finally written as the following equation :

$$\mathcal{L}_{\text{fin}} \;\; = \;\; i\bar{\psi}(x)\gamma^\mu D_\mu \psi(x) - m\bar{\psi}(x)\psi(x) - \frac{1}{4} F_{\mu\nu}(x) F^{\mu\nu}(x). \tag{1.9}$$

With this Lagrangian, the Euler-Lagrangue equation is given as follows :

$$\partial_\mu F^{\mu\nu} = e\bar{\psi}(x)\gamma^\nu \psi(x). \tag{1.10}$$

This is the well-known Maxwell equation. Here an additional field A_μ describes the electric scalar potential ($\nu = 0$) and the magnetic vector potential ($\nu = 1$, 2, 3).

1.1.2 Yang-Mills gauge theory

This section describes non-Abelian gauge theory. The strong interaction, which explains the interaction between quarks and gluons, is described by a non-Abelian SU(3) gauge theory. Basically the reason why the gauge fields are introduced is the same as the Abelian gauge theory. The Lagrangian is written as

$$\mathcal{L} = \sum_f \bar{q}_f (i\gamma^\mu D_\mu - m_f) q_f - \frac{1}{4} F^a_{\mu\nu} F^{a\mu\nu}, \tag{1.11}$$

where q is the quark field and f denotes a flavor state and m_f is a mass of quark. The field strength is also changed to keep the gauge invariance under SU(3) gauge transformation :

$$D_\mu = \partial_\mu - i g_s \left(\frac{\lambda^a}{2}\right) A^a_\mu \tag{1.12}$$

$$F^a_{\mu\nu}(x) = \partial_\mu A^{\mathrm{a}}_\nu(x) - \partial_\nu A^{\mathrm{a}}_\mu(x) + g_s f_{\mathrm{abc}} A^{\mathrm{b}}_\mu A^{\mathrm{c}}_\nu. \tag{1.13}$$

Here, g_s is the strong coupling constant, A^{a}_μ is the gluon field (a = 1, ...8) and f^{abc} is the structure constant of the group.

1.1.3 Glashow-Weinberg-Salam theory

The weak interaction seems to be described by an SU(2) gauge invariance since two particles within the same generation are transformed to each other. However, the mass term $m^2 A_\mu A^\mu$ is not gauge invariant as the Z boson and the W boson have masses. The Glashow-Weinberg-Salam theory can describe the experimental observations under unified interpretation of the weak and electromagnetic interactions. This subsection explains the Glashow-Weinberg-Salam theory. The Glashow-Weinberg-Salam theory is based on the gauge group $SU(2)_L \times U(1)$. Here, the subscript L is attached since the SU(2) affects on the left-handed components, meaning the current of the weak interaction being left-handed. In addition, neutrino is only left-handed. Thus we have to consider the gauge transformation differently for the left-handed and right-handed components.

In this case, the Lagrangian is written as

$$\mathcal{L} = i\bar{\psi_L}\gamma^\mu \left(\partial_\mu + \frac{ig'}{2}B_\mu Y + \frac{ig}{2}\boldsymbol{W_\mu}\cdot\boldsymbol{\sigma}\right)\psi_L + i\bar{\psi_R}\gamma^\mu\left(\partial_\mu + \frac{ig'}{2}B_\mu Y\right)\psi_R - \frac{1}{4}\boldsymbol{W_{\mu\nu}}\cdot\boldsymbol{W^{\mu\nu}} - \frac{1}{4}B_{\mu\nu}B^{\mu\nu} \tag{1.14}$$

$$\psi_L = \left(\begin{array}{c} \nu_L \\ l_L \end{array}\right) = \left(\begin{array}{c} \frac{1}{2}(1-\gamma^5)\psi_\nu \\ \frac{1}{2}(1-\gamma^5)\psi_l \end{array}\right), \psi_R = \frac{1}{2}(1+\gamma^5)\psi_l \tag{1.15}$$

$$B_{\mu\nu} = \partial_\mu B_\nu - \partial_\nu B_\mu \tag{1.16}$$

$$\boldsymbol{W_{\mu\nu}} = \partial_\mu \boldsymbol{W_\nu} - \partial_\nu \boldsymbol{W_\mu} - g\boldsymbol{W_\mu}\times\boldsymbol{W_\nu}, \tag{1.17}$$

where $\boldsymbol{W_\mu}$ and B_μ are the SU(2) and U(1) gauge fields, respectively. Y is a generator of U(1) Lie algebra defined as $Q = T^3 + \frac{Y}{2}$. g and g' are the SU(2) and U(1) coupling constants between gauge fields and fermions. $\boldsymbol{W_\mu}$ and B_μ are massless at this point to keep the gauge invariance.

We introduce the BEH (Brout-Englert-Higgs) mechanism to explain the W and the Z masses while keeping the gauge invariance.

In the BEH mechanism, a complex scalar field $\phi(x)$ is introduced. $\phi(x)$ is defined as follows :

$$\phi(x) = \left(\begin{array}{c} \phi_+ \\ \phi_0 \end{array}\right) = \left(\begin{array}{c} \phi_{R+} + i\phi_{I+} \\ \phi_{R0} + i\phi_{I0} \end{array}\right). \tag{1.18}$$

Here, the complex scalar field is subjected to the same gauge transformation as the lepton doublet ψ_L where ϕ_+ and ϕ_0 construct on SU(2) doublet. Thus, the Lagrangian of the scalar field is written as the following equation with requiring gauge invariance :

$$\mathcal{L}_{\text{Higgs}} = (D^\mu\phi)^\dagger(D_\mu\phi) - \mu^2\phi^\dagger\phi - \lambda(\phi^\dagger\phi)^2 \tag{1.19}$$

$$D_{\mu} \quad = \quad \partial_{\mu} + \frac{ig'}{2} B_{\mu} Y + \frac{ig}{2} \boldsymbol{W_{\mu}} \cdot \boldsymbol{\sigma}. \tag{1.20}$$

The first term and the other terms in the Lagrangian describe kinetic energy and potential energy, respectively. If the potential energy term is expanded with Eq. (1.18), it is written as follows :

$$V(\phi) = \frac{1}{2}\mu^2[(\phi_{R+})^2+(\phi_{I+})^2+(\phi_{R0})^2+(\phi_{I0})^2]+\frac{1}{4}\lambda[(\phi_{R+})^2+(\phi_{I+})^2+(\phi_{R0})^2+(\phi_{I0})^2]^2. \tag{1.21}$$

Here, Figure 1.2 shows the potential energy term regarding $(\phi_{R+})^2+(\phi_{I+})^2+(\phi_{R0})^2+(\phi_{I0})^2$ as a function Φ. The shape of the potential energy is characterized by the sign of μ^2. For $\mu^2 > 0$ the stable point is at $\Phi = 0$. However, for $\mu^2 < 0$ $\Phi = 0$ point is not stable. In the case of $\mu^2 < 0$ the stable point v is $\sqrt{\frac{-\mu^2}{\lambda}}$. To understand the Lagrangian around the stable point of potential energy v, the following ϕ definition is useful (Lorentz gauge) :

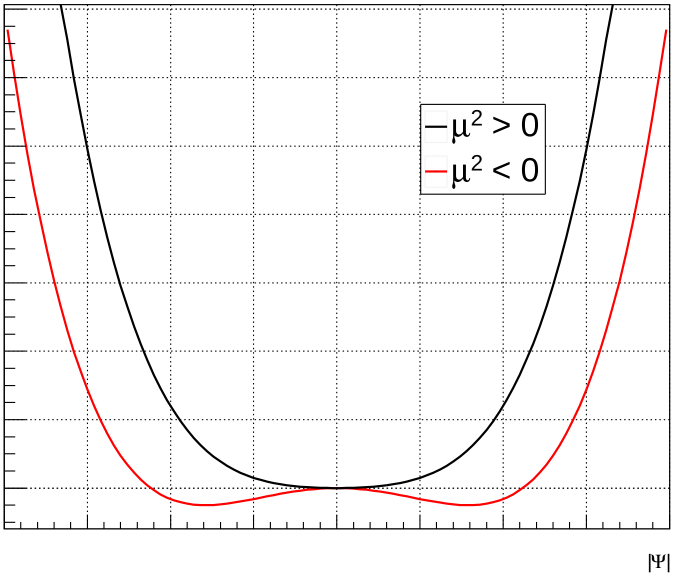

Figure 1.2: The potential of additional scalar field

$$\phi(x) = \frac{1}{\sqrt{2}} \begin{pmatrix} 0 \\ v + \eta(x) \end{pmatrix}. \tag{1.22}$$

Here, $\eta(x)$ is the unique degree of freedom of the ϕ_{R0}, called Higgs field. The potential energy and the kinetic energy terms are written as follows with the above definition :

$$\mathcal{L}_{\text{kinetic}} = \frac{1}{2}\left(\frac{gv}{2}\right)^2 \left(W^{+\mu}W^-_\mu + W^{-\mu}W^+_\mu\right) + \frac{1}{2}\left(\frac{\sqrt{g^2+g'^2}v}{2}\right)^2 Z^\mu Z_\mu + (\text{terms of } \eta) \quad (1.23)$$

$$W^\pm_\mu = \frac{1}{\sqrt{2}}(W^1_\mu \mp iW^2_\mu), \quad Z_\mu = \frac{gW^3_\mu - g'B_\mu}{\sqrt{g^2+g'^2}} \quad (1.24)$$

$$\mathcal{L}_{\text{potential}} = -\frac{1}{4}\frac{\mu^4}{\lambda} - \mu^2\eta^2 + \lambda v\eta^3 + \frac{1}{4}\lambda\eta^4. \quad (1.25)$$

Here, when new fields $W^\pm_\mu$ and Z_μ are defined using gauge fields $\boldsymbol{W_\mu}$ and B_μ, $\mathcal{L}_{\text{kinetic}}$ means the mass terms of new fields $W^\pm_\mu$ and Z_μ. $W^\pm_\mu$ and Z_μ masses are $\frac{gv}{2}$ and $\frac{\sqrt{g^2+g'^2}v}{2}$, respectively. If Eq.(1.14) is written using new fields $W^\pm_\mu$ and Z_μ, the weak interaction can be found the $W^\pm_\mu$ and Z_μ bosons to be the force carriers. The second term of $\mathcal{L}_{\text{potential}}$ $(-\mu^2\eta^2)$ suggests that new Higgs field η has a mass $M_\eta = \sqrt{-2\mu^2}$.

The BEH mechanism predicts a new Higgs boson. Thus the Higgs boson has been searched all over the world for a long time. In 2012, the Higgs boson was discovered, and the Glashow-Weinberg-Salam theory was perfectly proved. Figure 1.3 shows the invariant mass distribution of $h \to \gamma\gamma$. Figure 1.4 shows the local p0 value in the combined $h \to ZZ* \to 4\ell$, $h \to \gamma\gamma$ and $h \to WW* \to e\nu\mu\nu$ channels with the amount of the data collected in 2011 and 2012 of 4.6-4.8 fb^{-1} and 5.8-5.9 fb^{-1} at the center-of-mass energy 7 TeV and 8 TeV. The observation, which has a significance of 5.9 standard deviations, corresponding to a background fluctuation probability of 1.7 $\times 10^{-9}$, is compatible with the production and decay of the Standard Model Higgs boson.

1.2 Mysteries in the universe

The Standard Model has been examined to every details, resulting what it describes all correctly. However, there exists experimental observations that are not described by the Standard Model. For example, the existence of dark matter. Furthermore, the Higgs boson mass receives enormous quantum corrections from the virtual effects of every particles. Thus many theories have been proposed to deal with the dark matter and to avoid Higgs boson enormous quantum corrections. This section describes these experimental observations and the current leading models.

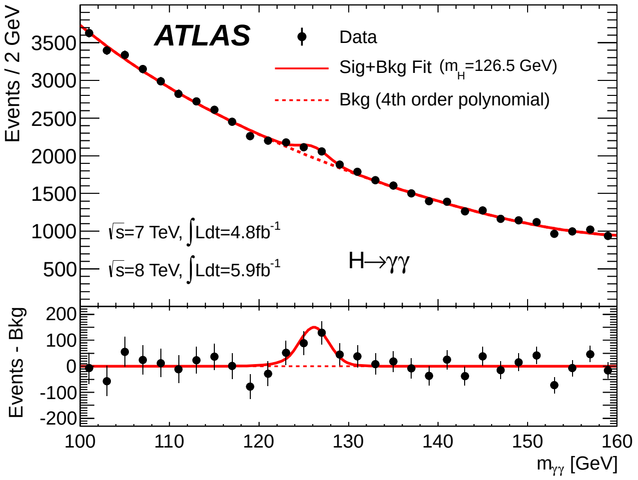

Figure 1.3: Invariant mass distribution of diphoton candidates for the combined $\sqrt{s} = 7$ TeV and $\sqrt{s} = 8$ TeV data samples. The result of a fit to the data of the sum of a signal component fixed to $m_H = 126.5$ GeV and a background component described by a fourth-order Bernstein polynomial is superimposed. The bottom inset displays the residuals of the data with respect to the fitted background component[2].

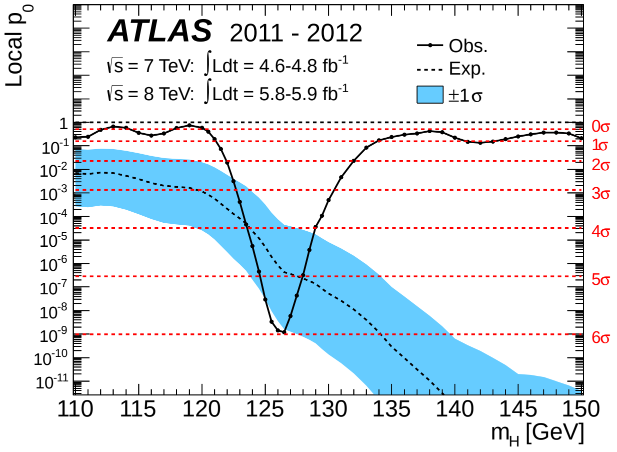

Figure 1.4: The observed (solid) local p0 as a function of m_H. The dashed curve shows the expected local p0 under the hypothesis of a standard model Higgs boson signal at that mass with its plus/minus one sigma band. The horizontal dashed lines indicate the p-values corresponding to significances of 1 to 6 sigma.[2]

1.2.1 Experimental observations of dark matter

Dark matter is necessary to explain some experimental observations, which is massive to feel gravitational force but no the electromagnetic nor strong interactions.

The most convincing evidence for dark matter is the rotating velocities of galaxies measured as a function of the radius from the galactic cluster center. Figure 1.5 shows the observed rotation curve at NGC 6503 spiral galaxy from Ref. [4]. The rotation velocity is written as $v^2 = \frac{M(r)G}{r}$ by Kepler's law. Here, G is the gravitational constant. The contribution from visible matter was like luminous (dashed line). However, the observed rotation curve exhibits a flat behavior at large distance. This result implies that invisible matter, which can not be observed with the electromagnetic interaction, distributes uniformly in the galaxy.

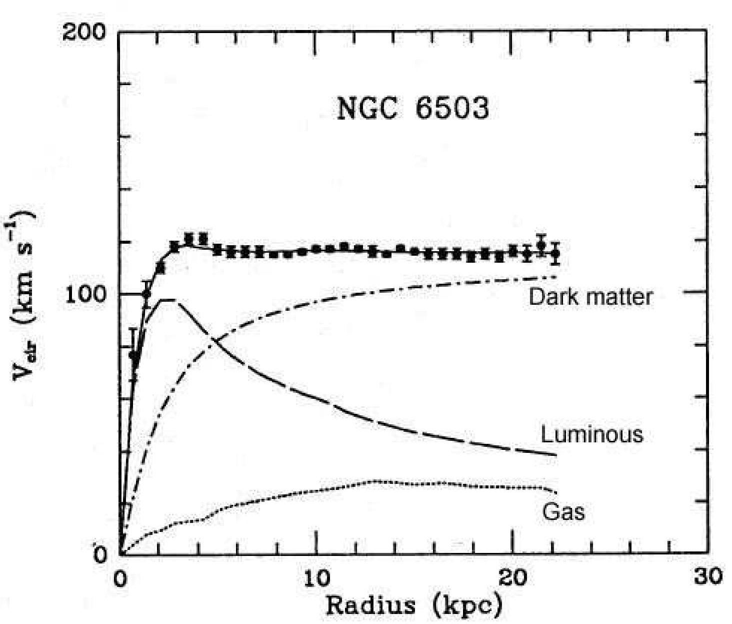

Figure 1.5: Three-parameter dark-halo fits (solid curve) to the rotation curve of NGC6503. The rotation curves of the individual components are also shown : the dashed curve is for the visible components, the dotted curve for the gas, and the dash-dot curve for the dark halo.[4]

Another evindence for dark matter is shown via the gravitational lensing effect as described by the general relativity. The path of a light ray is bent due to massive matter since matter can curve the spacetime in the general relativity. This effect is called the gravitational lensing. Figure 1.6 shows the image of the Abel2218 cluster taken by NASA/ESA. The real galaxies do not have such projected shapes. However, the shape is distorted by the gravitational lensing effect. This result involves the evindence of large massive matter that can not be seen by the electromagnetic interaction.

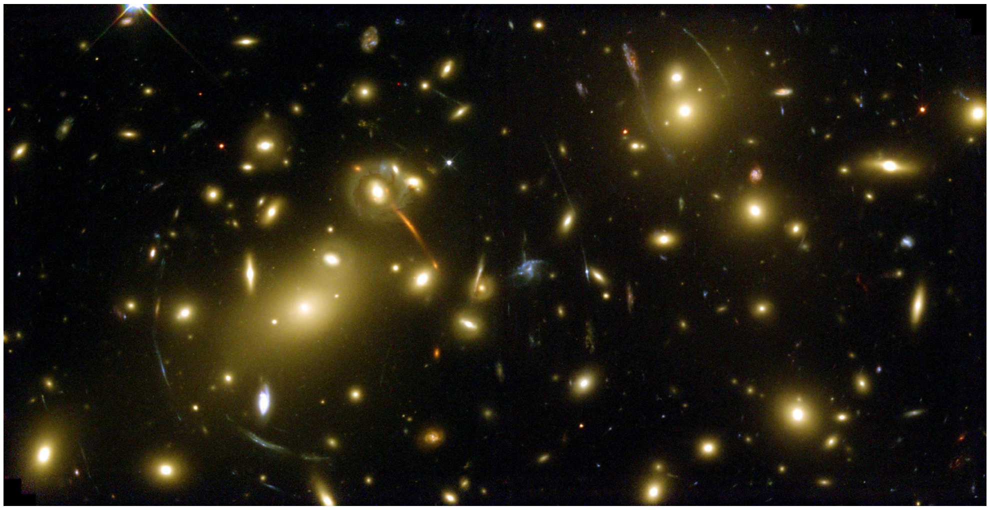

Figure 1.6: Image of the galaxy cluster Abel2218.

The third experimental evindence is from the result of the cosmic microwave background measurement. After the Big Bang, the universe was filled with an very dense plasma of charged particles and photons. The plasma went through an initial rapid expansion, and was cooled for about 380,000 years until the time of recombination in the Big Bang cosmology[6]. At this time, neutral atoms were formed, and the photons below certain energy were able to pass through the universe without any interruption from charged particles. Today, these photons have a thermal black body spectrum at a temperature of 2.7 K, and are known as the Cosmic Microwave Background. The CMB has an information of the composition of the universe because it represents the distribution at the point when the decoupling occurred in the early universe. The CMB measurement shows that the fluctuation of the baryon density only in the early universe was not enough to reproduce the present observation of large structure in the galaxy distribution. WMAP (Wilkinson Microwave Anisotropy Probe) was launched in 2001 with the mission to precisely measure the anisotropies in the CMB. The satelite is able to detect temperature variations as small as one millionth of a degree and know the total and baryonic matter desnsities [5]. The total and baryonic matter densities are measured as follows :

$$\Omega_m h^2 = 0.1334^{+0.0058}_{-0.0055} \tag{1.26}$$

$$\Omega_b h^2 = 0.02260 \pm 0.00053, \tag{1.27}$$

where $\Omega_m h^2$ is the total matter density, and $\Omega_b h^2$ is the baryonic density. The observation shows that these two numbers are different. This difference implies the existence of dark matter, and its density is $\Omega_{\rm dm} h^2 = 0.1123 \pm 0.0035$.

1.2.2 Mystery of Higgs boson mass and super symmetry model

It is believed that the mass of the Higgs boson of 125 GeV implies the existence of new physics. This section describes the reason why Higgs boson mass implies new physics, and explain the most popular theory for understanding strange Higgs mass of 125 GeV.

The Higgs boson mass of the Standard Model is affected by the quantum corrections from the virtual effects of every particle. The quantum corrections is written as Eq. (1.28)

$$M^2_{\text{Higgs}} = M^2_{\text{bare}} + \Delta M^2_{\text{Higgs}}, \tag{1.28}$$

where M^2_{Higgs}, M^2_{bare} and $\Delta M^2_{\text{Higgs}}$ are the observed mass squared, mass without the quantum correction and term of quantum correction, respectively. For example, Figure 1.7a shows an example of the quantum correction to M^2_{Higgs} from a loop containing a Dirac fermion. The quantum correction for the Dirac fermion is written as

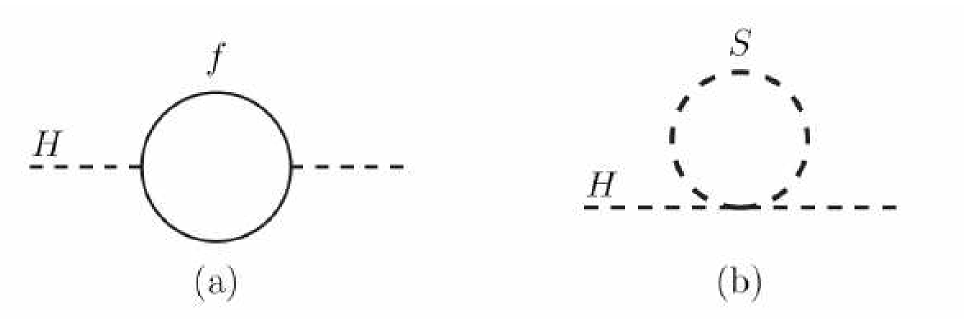

Figure 1.7: One-loop quantum corrections to the Higgs boson mass : (a) is for a dirac fermion f, and (b) is for a scalar particle S.

$$\Delta M^2_{\text{Higgs,fermion}} = -\frac{|\lambda_f|^2}{8\pi^2}\Lambda^2_{\text{UV}} + \cdots, \tag{1.29}$$

where λ_f is a coupling strength between the Higgs boson and the Dirac fermion, and Λ_{UV} is an ultraviolet momentum cutoff that is an energy scale at which the Standard Model can not be applied. The problem is that the quantum correction to the squared Higgs mass is some 30 orders of magnitude larger than the required value of $M^2_{\text{Higgs}} = O(100GeV)^2$ if Λ_{UV} is of order the Plank scale $M_{\text{P}} = 2.4 \times 10^{18}$ GeV. This problem is called the fine-tuning problem.

The most popular solution of the fine-tuning problem is a super symmetry that is a symmetry relating boson and fermion. The SuperSymmetry requires that all the Standard Model particles have a superpartner. The superpartner has the spin of which differs by a half-integer of the Standard Model particles. If a superpartner has the same mass with the Standard Model particles ($\lambda_f = \lambda_S$), the quantum correction by a superpartner is written as

:

$$\Delta M^2_{\text{Higgs,fermion partner}} = 2 \times \frac{|\lambda_f|^2}{16\pi^2}\Lambda^2_{\text{UV}} + \cdots. \tag{1.30}$$

If the superpartner exists in addition to the Standard Model particles, the fine-tuning problem is solved since Eq. (1.29) and Eq. (1.30) are canceled.

Figure 1.8 shows the list of particles of Minimal Supersymmetric Standard Model (MSSM) that is the simplest super symmetric model. In the super symmetry, two Higgs doublets are needed. Thus some other Higgs bosons exist in addition to the Standard Model Higgs boson. In addition, lightest stable particle neutralino, which is a mixed state of the bino, the neutral wino and the neutral higgsino, is present. The neutralino is considered to be the dark matter candidate.

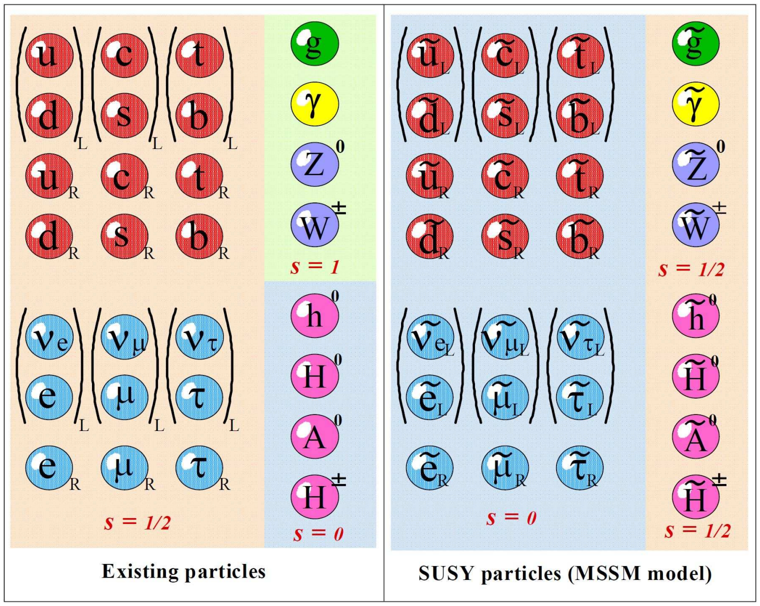

Figure 1.8: List of particles in the MSSM.

1.3 Searches using the Z boson and missing transverse momentum final states

In this thesis, results of three analyses that are shed light on the above mysteries are presented. Three searches are the search for heavy resonance decaying to ZZ pairs, the search for Higgs boson decaying to invisible particles and the search for dark matter produced in association with a leptonically decaying Z boson. The final states of the two searches are the same, namely $\ell\ell +$ invisible particles, and the three analyses are illustrated by the common background estimations. With the ATLAS detector, we can use an imbalance in transverse

Table 1.1: The branching fraction of the Z boson decay

Particles	Branching ratio
Neutrinos (all)	20.00 ± 0.06 %
$e\bar{e}$	3.363 ± 0.004 %
$\mu\bar{\mu}$	3.366 ± 0.007 %
$\tau\bar{\tau}$	3.367 ± 0.008 %
Quarks (all)	69.91 ± 0.06 %

momentum sum as an information of invisible particle. Thus, we define missing momentum in the transverse plane, called "missing transverse momentum"(MET, $E_{\mathrm{T}}^{\mathrm{miss}}$). This section describes the motivation of these three searches.

1.3.1 Search for the ZZ resonance

The Standard Model can be now regarded as an established theory to explain various behavior of elementary particles. However, some extensions to the Standard Model are required to exlpain unresolved problems such as dark matter, the hierarchy problem, the neutrino mass and so on (see section 1.2). Many theories are proposed to explain these problems, and suggest the existence of additional heavy resonance with properties similar to recently discovered Higgs boson. The two-Higgs-doublet-model(2HDM)[7], which is assumed in the MSSM, is one of the popular models. The 2HDM predicts the existence of an additional heavy Higgs boson decaying to two on-shell Z bosons. Thus we have searched for an additional heavy Higgs bosons decaying to the ZZ pair.

The Z boson decays into a fermion and its antiparticle. The list of branching ratio is shown in Table 1.1. The branching fraction of the Z boson decay differs substantially among the kind of particles due to the mixing between SU(2) and U(1) couplings. In the case of the ZZ resonance analysis, $ZZ \to \ell\bar{\ell}\nu\bar{\nu}$ decay channel, where one of Z boson decays to two charged leptons and the other Z boson decays to two neutrinos, provides complementary sensitivity, as shown in Figure 1.9[8], because $\ell\ell + \nu\nu$ channel has the larger branching fraction than 4ℓ channel, and cleaner event topology than $\ell\bar{\ell}q\bar{q}$ and $\nu\bar{\nu}q\bar{q}$.

Thus we chose the $H \to ZZ \to \ell\bar{\ell}\nu\bar{\nu}$ channel. Since the neutrino can not be detected with the ATLAS detector, the final objects in the analysis are two charged lepton and a large missing transverse momentum. Figure 1.10 shows the Feynman diagram of the signal in this analysis.

An advantage of this resonance search is that a comprehensive search is possible for a new heavy particle regardless of the physics model under examination. In the current accumulation of experimental data, we do not have a definite clue how to extend the Standard Model. Thus the resonance search is a very useful way to approach new physics. Furthermore, the

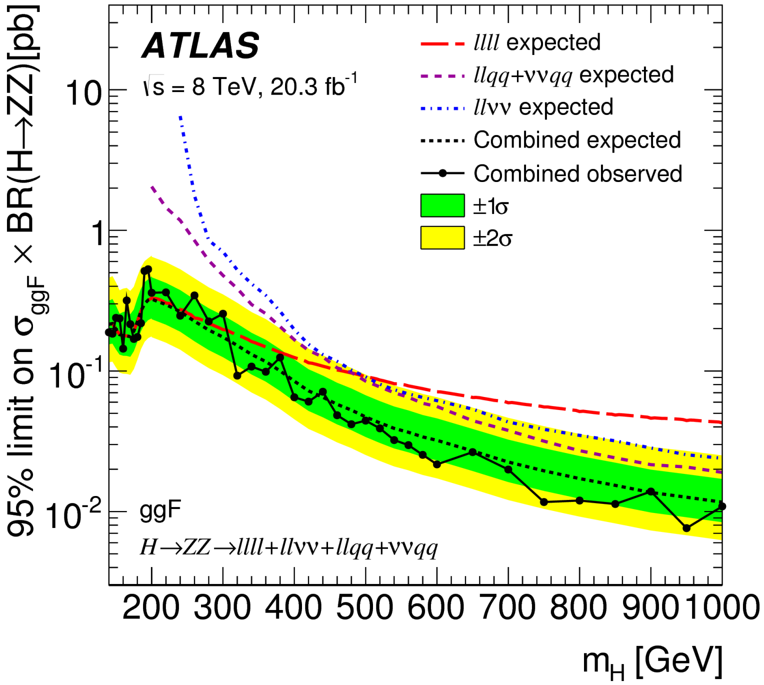

Figure 1.9: 95% upper limit on $\sigma \times BR(H \rightarrow ZZ)$ as a function of m_H in Run-1 ATLAS analysis in Ref.[8]. The solid black line and points indicate the observed limit. The dashed black line indicates the expected limit and the bands the 1-σ and 2-σ uncertainty ranges about the expected limit. The dashed colored lines indicate the expected limits obtained from the individual searches; for $\ell\ell qq$ and $\nu\nu qq$ searches, only the combination of the two is shown as they share control regions.

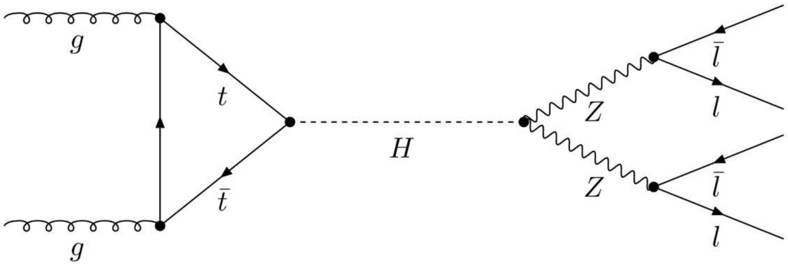

Figure 1.10: Feynman diagram of high mass Higgs boson production and decay.

cross section of high-mass particles has been drastically increased because the LHC has been operated at the center-of-mass energy increased to 13 TeV from 8 TeV since May 2015. Figure 1.11 shows the ratio of LHC parton luminosities at the two center-of-mass energies, where M_x is the mass of new particle [9].

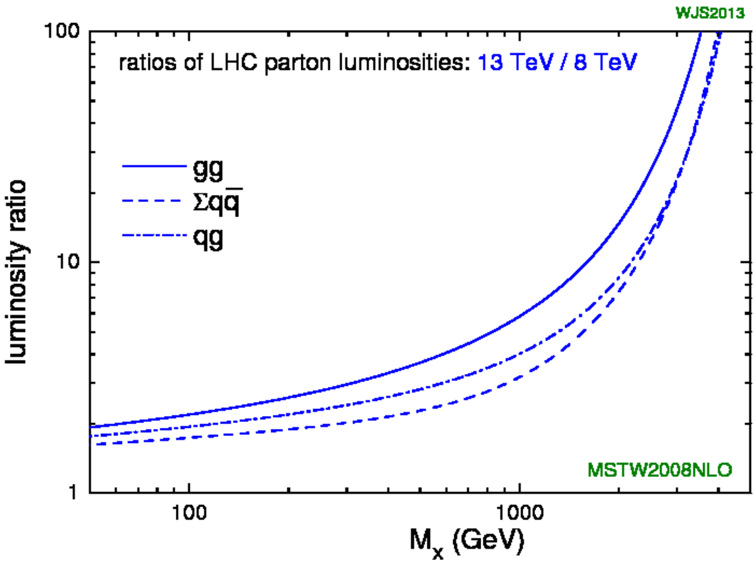

Figure 1.11: The ratios of LHC parton luminosities[9].

Using the same final state, limits are also set on the production of a spin-2 Kaluza-Klien(KK) graviton. The KK graviton is expected in the Randall-Sundrum(RS) framework with a warped extra dimension(RS1) [10].

1.3.2 Search for Higgs decaying to invisible particles

Many direct detection experiments of dark matter are in operation in the world. Dark matter has not been directly observed although many indirect experimental evidences have been confirmed. The idea of direct detection experiment is based on the observation of the dark matter elastic scattering with nuclei in the detector. The expected energy of nuclear recoils induced by the dark matter interactions is in the range from several keV to several hundreds keV depending on the dark matter mass and the atomic number of the detector. A summary on the limit of direct detection experiment is shown in Figure 1.12 [11].

The Higgs portal model[12] can explain why dark matter is not discovered directly so far. In the Higgs portal dark matter scenario, dark matter is coupled to the Standard Model particles via the Higgs boson. In this model, the observed Higgs boson with a mass of about

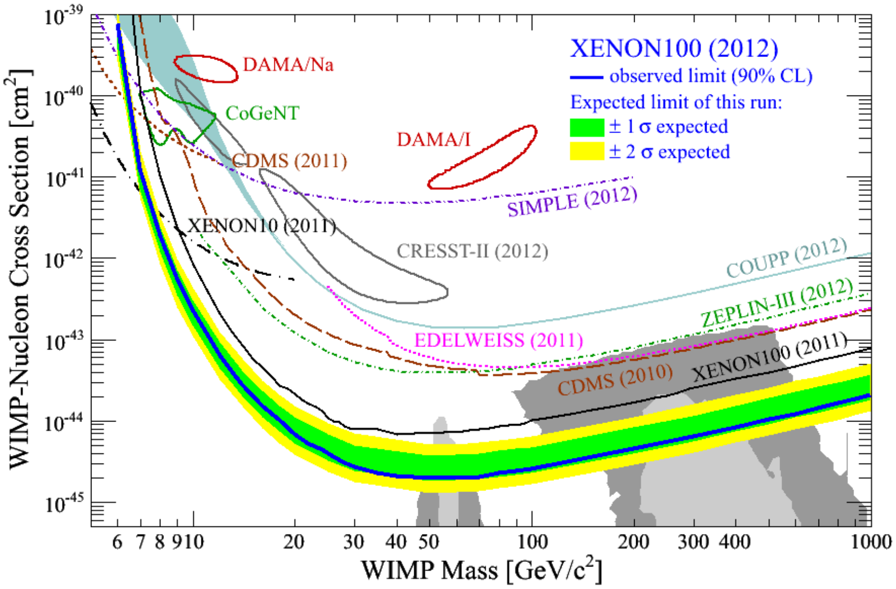

Figure 1.12: Result on spin-independent dark matter-nucleon scattering from XENON100 : The expected sensitivity of this run is shown by the green/yellow band ($1\sigma/2\sigma$) and the resulting exclusion limit (90% CL) in blue. For comparison, other experimental limits (90% limit) and detection claims are also shown. Here dark matter is called WIMP referring to weakly interacting massive particle[11].

125 GeV might decay to dark matter since dark matter get a mass from the Higgs boson as same as the Standard Model particles. If dark matter gets a mass from the Higgs boson, the following terms have to be added to the Standard Model Lagrangian, Eq. (1.14) depending on the spin of dark matter:

$$\begin{aligned} \mathcal{L}_{\rm S} &= -\frac{1}{2}m_S^2 S^2 - \frac{1}{4}\lambda_S S^4 - \frac{1}{4}\lambda_{hSS} H^\dagger H S^2 && (1.31) \\ \mathcal{L}_{\rm V} &= \frac{1}{2}m_V^2 V_\mu V^\mu + \frac{1}{4}\lambda_V (V_\mu V^\mu)^2 + \frac{1}{4}\lambda_{hVV} H^\dagger H V_\mu V^\mu && (1.32) \\ \mathcal{L}_{\rm f} &= -\frac{1}{2}m_f \bar{\chi}\chi - \frac{1}{4}\frac{\lambda_{hff}}{\Lambda} H^\dagger H \bar{\chi}\chi. && (1.33) \end{aligned}$$

After electroweak symmetry breaking, the complex scalar field H is shifted in the same way as Eq. (1.22) and the Lagrangian will be given by

$$\begin{aligned} \mathcal{L}_{\rm S} &= -\frac{1}{2}M_S^2 S^2 - \frac{1}{4}\lambda_S S^4 - \frac{1}{2}\lambda_{hSS} v\eta S^2 - \frac{1}{4}\lambda_{hSS}\eta^2 S^2, && (1.34) \\ \mathcal{L}_{\rm V} &= \frac{1}{2}M_V^2 V_\mu V^\mu + \frac{1}{4}\lambda_V (V_\mu V^\mu)^2 + \frac{1}{2}\lambda_{hVV} v\eta V_\mu V^\mu + \frac{1}{4}\lambda_{hVV}\eta^2 V_\mu V^\mu, && (1.35) \\ \mathcal{L}_{\rm f} &= -\frac{1}{2}M_f \bar{\chi}\chi - \frac{1}{2}\frac{\lambda_{hff}}{\Lambda} v\eta\bar{\chi}\chi - \frac{1}{4}\frac{\lambda_{hff}}{\Lambda}\eta^2\bar{\chi}\chi. && (1.36) \end{aligned}$$

Here, $M_X (X = S,\ V,\ f)$ are physical masses of the dark matter particle and defined as

$$M_S^2 = m_S^2 + \frac{1}{2}\lambda_{hSS} v^2, \tag{1.37}$$

$$M_V^2 = m_V^2 + \frac{1}{2}\lambda_{hVV} v^2, \tag{1.38}$$

$$M_f = m_f + \frac{1}{2}\frac{\lambda_{hff}}{\Lambda} v^2. \tag{1.39}$$

The terms ηXX suggest that the diagram shown in Figure 1.13(a) exists, and the diagram of direct search experiment is written in Figure 1.13(b) in the Higgs-portal model. The cross section between dark matter and nucleon searched for in the direct experiments is reduced due to the smaller coupling constant between the Higgs boson and the nucleon.

In the Higgs-portal model, the invisibly decaying Higgs boson is the best way to search for dark matter. Figure 1.14 shows the limit of invisibly decaying Higgs boson in Run-1 in the case where the direct search experiment results are interpreted as in the Higgs-portal model[13]. Within the constraints of Higgs-portal model, the results indicate strongest limits applicable for the low mass dark matter candidate.

Thus we have focused on the search for the Higgs decaying to dark matter pairs at the LHC which is the only accelerator to be able to produce the Higgs boson. The diagram of Higgs production and the cross-section at the LHC are shown in Figure 1.15 and Table 1.2, respectively. The dominant Higgs boson production is gluon fusion, and the second dominant

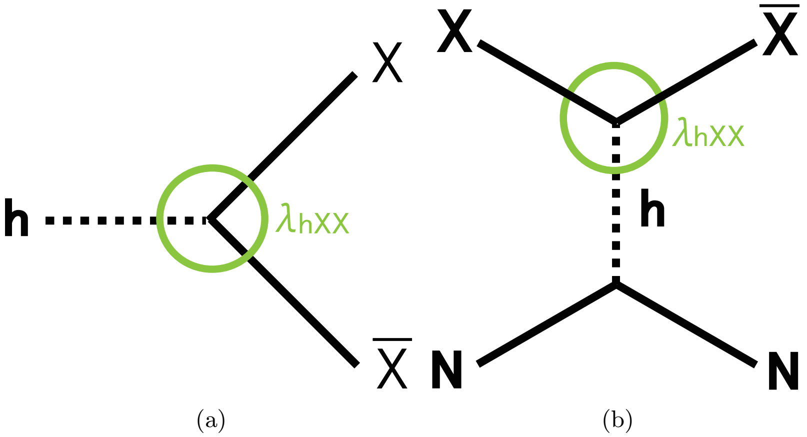

Figure 1.13: Feynman diagrams in the Higgs portal model in (a) the Higgs decay (LHC experiments) and (b) in the direct detection experiments.

process is a vector boson fusion. Since dark matter is also treated as the missing transverse momentum as neutrino, presence of an easily-tagged Standard Model particle in addition against which the invisible particles recoil, is crucial. Thus $Z(\rightarrow \ell\ell)H(\rightarrow inv.)$ production is chosen to search for the invisibly decaying Higgs boson in this thesis since ZH production is the best way to tag the Higgs boson production when the Higgs boson decays to the invisible particles. Figure 1.16 shows the Feynman diagram for Higgs boson decaying to dark matter pairs.

Table 1.2: The production cross-section of the Higgs boson at the LHC with $\sqrt{s} = 8$ TeV and $\sqrt{s} = 13$ TeV.

center-of-mass energy	gluon fusion	VBF	WZ	ZH	$t\bar{t}H$
8 TeV	19.27 pb	1.578 pb	0.7046 pb	0.4153 pb	0.1293 pb
13 TeV	43.62 pb	3.727 pb	1.362 pb	0.8594 pb	0.5027 pb

1.3.3 Search for dark matter in association with a leptonically decaying Z boson

Recently, dark matter is mainly searched using the dark matter elastic scattering with nuclei. An alternative approach to the detection of dark matter is to produce them in a laboratory. At the LHC, the dark matter production is predicted to occur mainly in pairs of dark matter. Thus we also have searched dark matter pair production in association with a leptonically decaying Z boson.

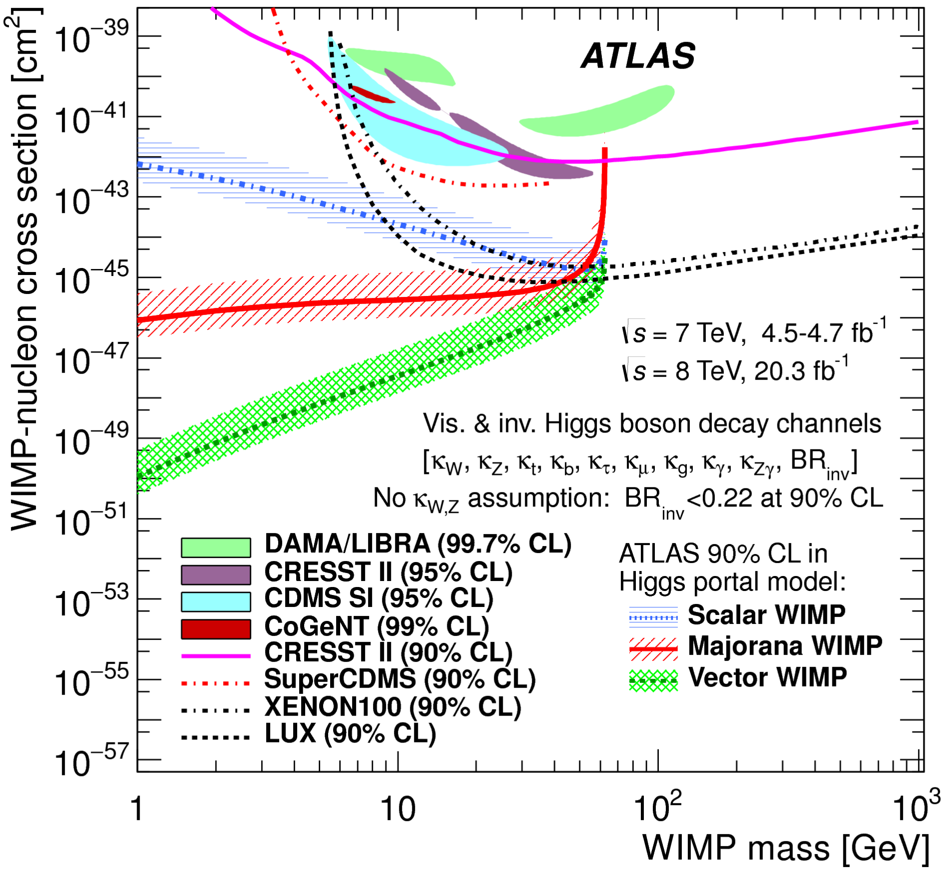

Figure 1.14: The upper limit at the 90% CL on the dark matter-nucleon scattering cross section in a Higgs portal model as a function of the mass of dark matter, shown separately for a scalar, Majorana fermion, or vector-boson[13]. The hashed bands indicate the uncertainty resulting from varying the form factor $f_{\rm N}$ by its uncertainty.

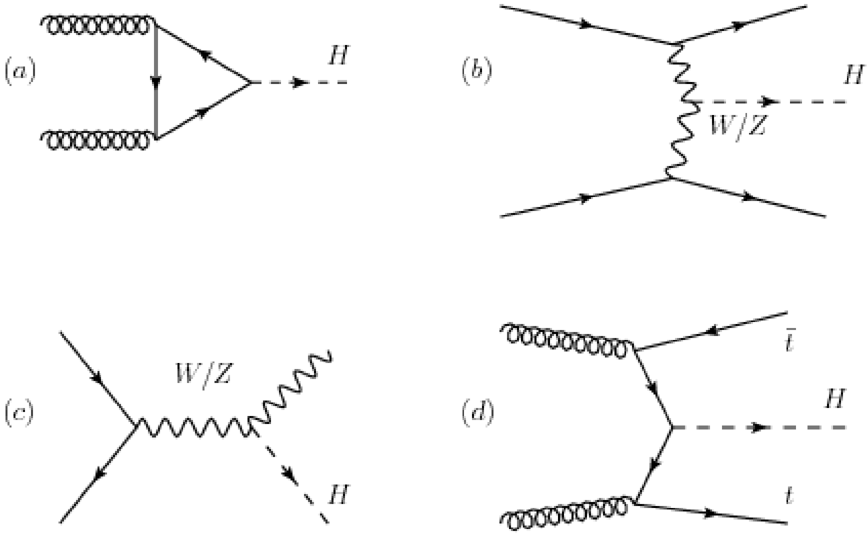

Figure 1.15: Higgs boson production channels at the LHC : (a)gluon fusion, (b)Vector boson fusion, (c) Higgs-Strahlung and (d) $t\bar{t}$ associated production.

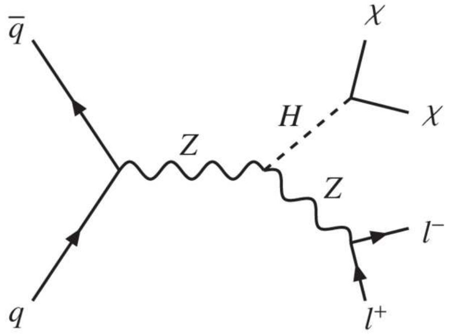

Figure 1.16: Feynman diagram for Higgs boson decaying to dark matter pairs.

The simplest models which include dark matter are the so-called Simplified Models[14]. In these models, other new particles are introduced to mediate the interactions between dark matter and the standard model particles. The simplest model has one pair of dark matters and one mediator particle, and it includes only 5 additional parameters to the standard model : dark matter mass m_{χ}, mediator mass M, mediator width Γ, coupling between the mediator and dark matter g_{χ} and coupling between the mediator and the standard model particles g_q.

The models can be further simplified when the momentum transfer (Q) is smaller than the mediator mass. This is the condition for the Effective Field Theory (EFT) models. There is no mediator particle in EFT and it has only two parameters : dark matter mass m_{χ} and mass scale M. However the EFT is valid only when $Q \ll M$ and is not a UV-safe theory. The greater number of higher Q events at 13 TeV means that the EFT models will be invalid a greater percentage of the time. This is why the simplified models have become increasingly important to study. Further details about the EFT and simplified models can be found in Ref. [15].

The presence of dark matter, can be inferred from their recoil against the standard model particle in the search for Higgs invisibly decaying. Thus we have searched $pp \to X\bar{X} + Z$, where the Z boson is emitted from the initial state radiation (mono-Z production). Figure 1.17 shows the Feynman diagram for the mono-Z production.

Figure 1.18 shows the comparison of the inferred limits to the constraints from spin-dependent direct detection experiments in the Run-2 mono-jet analysis [16]. This comparison is model-dependent in the context of the simplified model with axial-vector coupling. In this case, stringent limits on the scattering cross section of the order of 10^{-42} cm^2 up to dark matter masses of about 300 GeV are inferred.

The mono-Z production has the same topology as the invisibly decaying Higgs boson, and its phase space is also similar. Thus we applied exactly the same event selections and background estimations to both search for invisibly decaying Higgs boson and search for mono-Z production. In the following sections, the invisibly decaying Higgs boson and mono-Z analyses are collectively called as the dark matter search since the same event selection and background estimation are used for both the analyses.

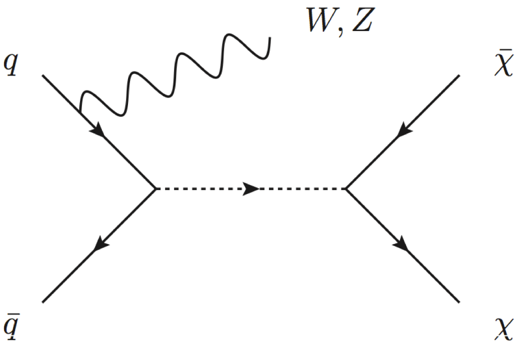

Figure 1.17: Feynman diagram for mono-Z production.

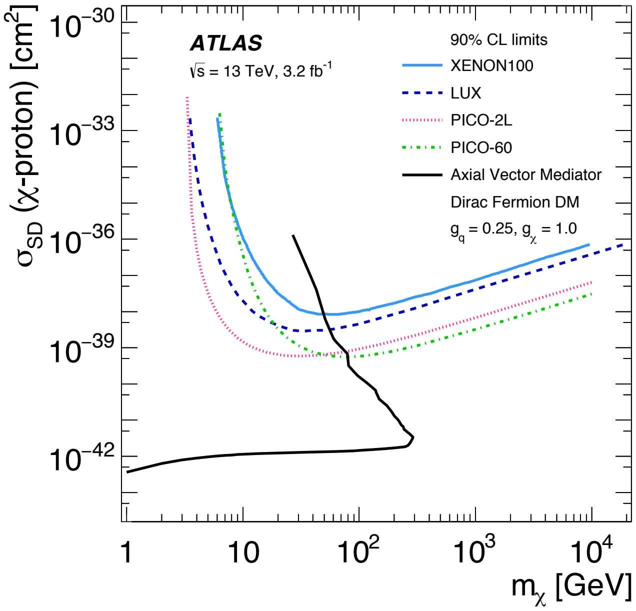

Figure 1.18: A Comparison of the inferred limits to the constraints from direct detection experiments on the spin-dependent dark matter-proton scattering cross section in the context of the simplified model with axial-vector coupling. The limits are shown at 90% CL. The comparison is model-dependent and solely valid in the context of this model, assuming minimal mediator width and the coupling values $g_q = 1/4$ and $g_\chi = 1$.

Chapter 2

Experimental Apparatus

The high energy hadron collison is provided by the Large Hadron Collider (LHC), with the data taken using the ATLAS detector. This section gives a brief introduction to the LHC and the ATLAS detector.

2.1 The Large Hadron Collider

The Large Hadron Collider [17] built at the European Organaization for Nuclear Research (CERN) is a synchrotron located at the border of France and Switzerland. The LHC was constructed between 1998 and 2009, currently being the largest accelerator in the world. The LHC accelerates protons and heavy ions around the circular 28 km tunnel located 100 m underground. The LHC was designed to provide collision of protons at a maximum center of mass energy of $\sqrt{s} = 14$ TeV and an instantaneous luminosity of $\mathcal{L} = 10^{34}$ cm^{-2}s^{-1}.

Collisions occur at four points around the LHC ring, CMS, ATLAS, LHCb and ALICE, as shown in Figure 2.1. CMS (The compact Muon Solenoid) and ATLAS (A Toroidal LHC Apparatus) are built to aim the discovery of the Higgs boson. LHCb (The Large Hadron Collider Beauty experiment) is dedicated to the bottom quark physics where the parameters of CP violation in the interactions associated with b-quarks are studied. ALICE (A Large Ion Collider Experiment) is designed to study the phenomena of strong interaction in heavy ion collisions.

The LHC is a super-conducting particle accelerator circulating two proton beams in opposite directions. In 2010-2011 and 2012, the center of mass energy was 7 TeV and 8 TeV,respectively. In this paper, The data taken with the center of mass energy of 13 TeV in 2015-2016 are used. The LHC plans to upgrade to $\sqrt{s} = 14$ TeV in near future.

The energy of the beam is reached through a series of accelerating stages. The first stage is that the proton is ionized and accelerated in the LINAC2 (LINear ACCelerator 2) to an energy of 50 MeV. After the first step, The protons are injected into the PS Booster (Proton Synchrotron Booster) which further increases the energy of the protons to 1.4 GeV.

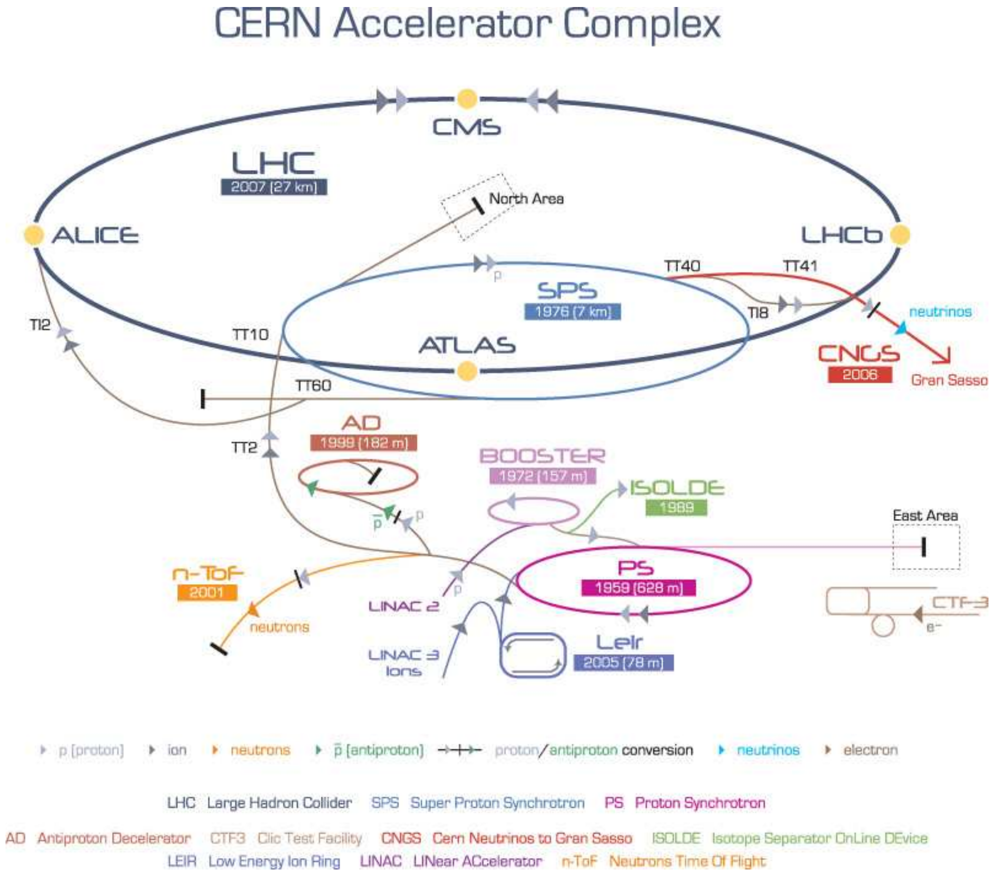

Figure 2.1: A schematic of the Large Hadron Collider.

The protons are then injected into the SPS (Super Proton Synchrotron) which increase their energy to 450 GeV. As the final step, the protons are injected into the LHC which completes the ramping of the energy to the final target energy. In the LHC ring, the acceleration is achieved through application of an oscillating electric field in resonant frequency (RF) cavities. RF cavities are designed to accelerate the bunches to an energy of 7 TeV.

2.2 The ATLAS detector

The ATLAS detector intends to perform general verification of particle physics and new physics search at the LHC energy. It is designed to be sensitive for various processes in both *pp* collisions and heavy ion collisions. Figure 2.2 shows the overview of the ATLAS detector. The ATLAS detector has a cylindrical shape and is about 25 m in height and 44 m in width, with a weight of roughly 7000 tons. Collisions occur at the center of the ATLAS detector, and many kinds of subdetectors surrounding the collision point grab the particles produced by the collisions. These subdetectors consist of the inner tracking detector, the calorimeter system, and the muon spectrometer. This section briefly describes the properties of all the subdetectors.

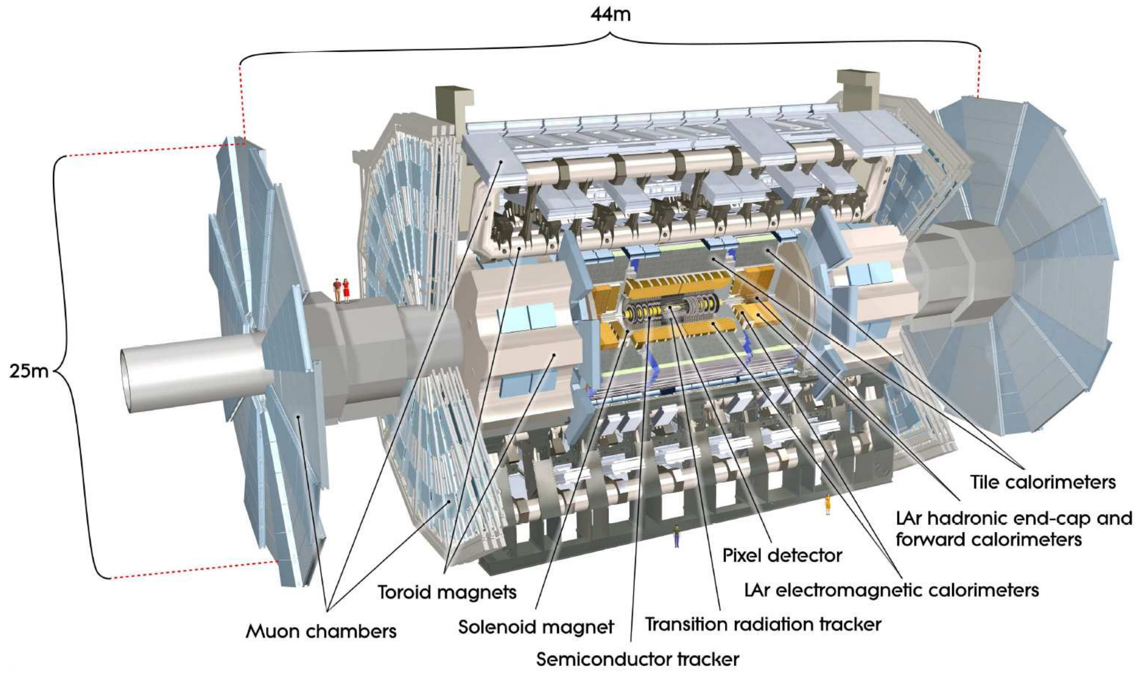

Figure 2.2: The ATLAS detector[18].

2.2.1 Coordinate system

All of the subdetectors are concentric around the collision point. The coordinate system is commonly used for detector hardware description specifying the positions of the modules in terms of x, y and z. It is also used for physics analyses. The z-axis is defined along the beam pipe, positive (negative) side is called as A side (C side). The plane that is perpendicular to the z-axis is called the transverse plane, the x-axis from the collision pointing to the center of the LHC ring and the y-axis being upward from the collision point. Radial distance r and azimuthal angle ϕ are used on the transverse plane in cylindrical coordinates. Furthermore, pseudorapidity η is defined in terms of the polar angle θ as $\eta = -\ln(\tan(\frac{\theta}{2}))$. The transverse momentum p_{T} is defined as $p_{\mathrm{T}} = p\sin\theta = p/\cosh\eta$ in cylindrical coordinates. In addition, a variable called ΔR defined as $\sqrt{(\Delta\eta)^2 + (\Delta\phi)^2}$ is often used in physics analyses, where $\Delta\eta$ and $\Delta\phi$ are the difference between the two directions in η and ϕ.

2.2.2 The inner detector

The inner detector is located nearest to the collision point, having a role is to reconstruct trajectories of charged particles. The positions of charged particles are measured with high precision as particles traverse through the inner detector. The superconducting solenoid which provides a uniform 2T magnetic field surrounding all of the inner detectors. Charged particles are bent by this field, where the curvature of the trajectories are used for momentum calculation. The inner detector is composed of three kinds of subdetectors, pixel detector, semiconductor tracker (SCT) and the transition radiation tracker (TRT) as shown in Figure 2.3.

The pixel detector [19, 20] is the innermost detector nearest to the collision point, consisting of three barrel layers and three endcap layers each, providing a uniform coverage in ϕ for $|\eta| < 2.5$. In addition, the insertable B-layer (IBL) has been installed after Run-1 to the position closest to the beam pipe[21]. The layer has many silicon sensors which is divided into small pixels (50×400 μm). When a charged particle passes through a pixel, electron hole pairs are generated and drift in an applied electric field to the readout electrodes. The system contains a total of 80 million readout channels and provides a position resolution of 10 μm in the r-ϕ plane, and 115 μm in the z-direction.

The SCT [22, 23] is the second innermost detector surrounding the pixel detectors. The mechanism of SCT to detect charged particles is almost the same as the pixel detector. The silicon modules are introduced in many strips of typically 12 cm length in the case of SCT. To obtain a position of charged particle in z-direction, a second detector is required to provide on orthogonal measurement. The entire SCT has about 60 million readout channels.

The TRT is the outermost subdetector[24]. The TRT contains about 300000 straw tubes that occupy 70 layers in the barrel and 140 layers in each end cap. The straw tube is filled with a gas to be ionized by incident charged particles. When a charged particle incidents to the TRT, electrons drift in an applied electric field to the wire strung along the straw

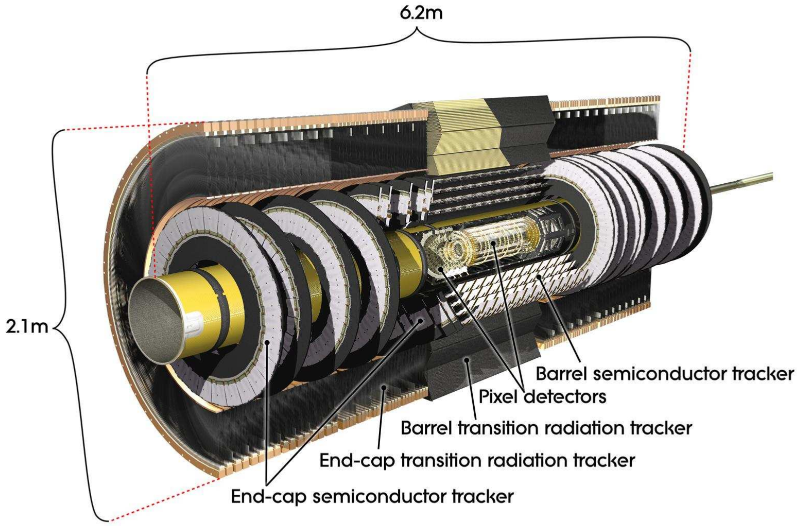

(a)

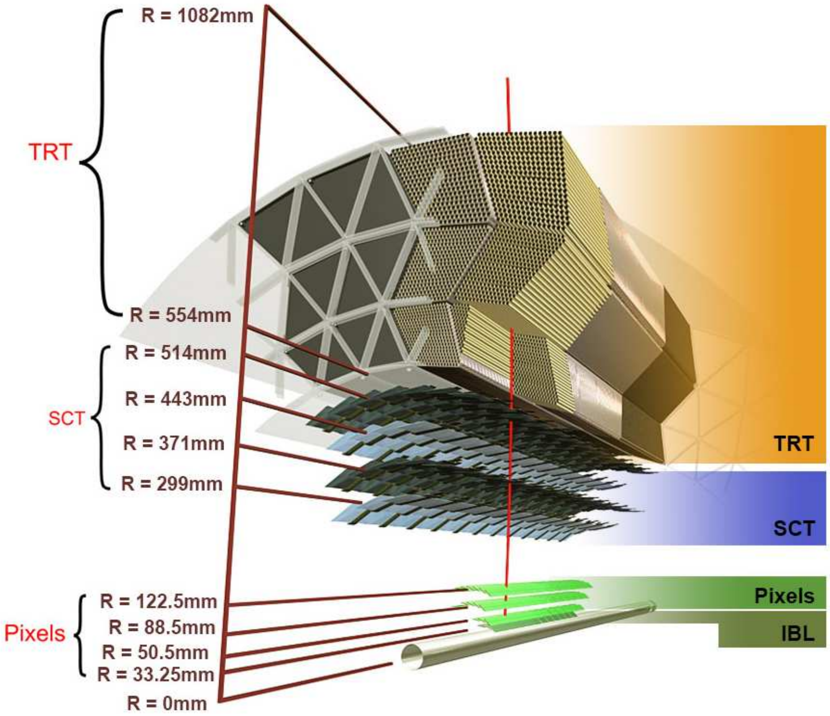

(b)

Figure 2.3: Schematics of the inner detector.

tube at the where electrons are avalanche multiplied. In addition to measure the position of charged particle, the TRT is designed to help with particle identification using the number of transition radiation photons generated by relativistic electrons.

2.2.3 The calorimeter systems

The calorimeters surround the inner detectors. After momenta of charged particle are measured with their tracks, calorimeters provide energy measurements of particles which feel electromagnetic or hadronic interactions. Neutrinos do not interact in the detector, and muon is measured as a Minimally Ionizing Particles. Particles from the hard-scatter collision interact with the calorimeter material creating cascades of particle called showers. There are two types of cascades depending on the source of particles, namely electromagnetic and hadronic showers. Since two types of showers have different properties, different techniques are required in accordance with types of showers. The electromagnetic calorimeter is designed to measure the energy of electromagnetic showers, and the hadronic calorimeter is designed to measure the energy of hadrons. The ATLAS calorimeter system consists of the two kind of calorimeters with a total coverage of $|\eta| < 4.9$, as shown in figure2.4(a).

The liquid-argon electromagnetic calorimeter is located outside of the inner detector, and designed to detect electromagnetic shower which is created by electrons and photons. The calorimeter uses an accordion-like structure of lead as the passive material as shown in 2.4(b). When a charged particle go through the electromagnetic calorimeter, electrons and photons interact with lead and multiple tracks are detected by the liquid-argon. In the case of hadrons, the probability of interaction in the lead is small giving small signal but hadronic shower is created in the iron or copper plates in hadronic calorimeter. The system is divided into a barrel region which covers the range $|\eta| < 1.475$, and two endcap regions each covering 1.375 $< |\eta| < 3.2$.

The hadronic calorimeter consists of the tile calorimeter at the barrel, and the liquid-argon hadronic calorimeter at the endcap. The tile calorimeter is composed of steel and scintillating tiles. It covers the range of $|\eta| < 1.7$. When hadrons go through the tile calorimeter, hadrons interact with the atomic nuclei of steel through the strong interaction, and then produced particles are detected by the scintillator to radiate photons. The intensity of photons is converted to an electric signal. The liquid-argon calorimeter functions similarly the electromagnetic calorimeter, and covers the range of $1.5 < |\eta| < 4.9$. The difference is to use copper and tungsten as passive material instead of lead.

2.2.4 The muon spectrometers

Outermost subdetector is the muon spectrometer which consists of toroidal magnets, resistive plate chambers (RPC)[25], thin gap chambers (TGC)[26], cathode strip chambers (CSC)[27], and monitored drift tubes (MDT)[28]. The muon spectrometers measure the muon momentum from the curvature in the toroidal magnetic field . The track information from the

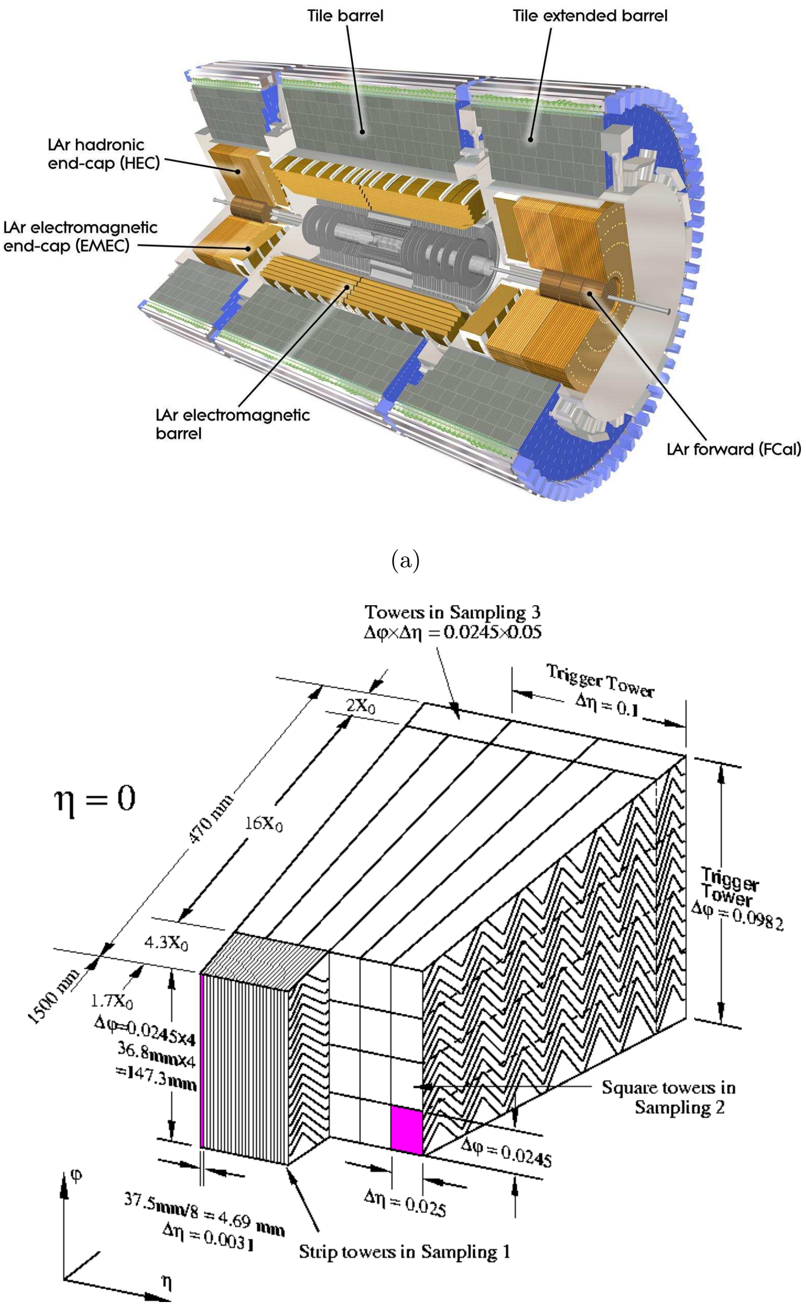

(a)

(b)

Figure 2.4: Schematics of the calorimeter.

inner detector can also be combined to further improve the momentum measurement and the identification. Figure 2.5 shows the illustration of the muon spectrometers.

The RPCs are used in the barrel region, covering the region $|\eta| < 1.05$. They collect ionized charges on two parallel resistive plates separated at a small gap. The signal multiplication is operated in an avalanche mode, thus the RPC is able to achieve fast signal readout. The RPCs are used for the triggers utilizing their fast response.

The TGCs are located in the endcap regions, covering $1.05 < |\eta| < 2.7$. The TGC consists of two conducting cathodes of parallel wires at a small gap. This mechanism can achieve a fast readout, thus TGC is also used for triggering. The TGCs have a good spatial resolution provided by the wires, therefore they have began to be used also for muon reconstruction.

The CSCs are used for precise tracking, operated similarly as the TGCs, with a reduced spacing between wires. The CSCs are installed in the regions $2.0 < |\eta| < 2.7$. CSC has a higher rate resistance than MDT, thus it is used in high η regions replacing MDT.

The MDTs are constructed using brass tubes operated in proportional mode and are instrumented covering the outermost region of the ATLAS detector. The MDTs perform precise measurement of the track coordinates, and are located in both barrel and endcap regions, covering $|\eta| < 2.7$.

2.3 Trigger and data acquisition system

The collision rate of the LHC was 20 MHz in Run-1 and at the beginning of Run-2. It was raised to the design value of 40 MHz in 2015, shortening the bunch space to 25 ns from 50 ns. The average data size of data from the ATLAS detector is about 1.5 MB per collision, amounting to a data rate of 60 TB/s. It is not realistic to record all data on permanent storage. Therefore the ATLAS experiment has a trigger system to select most interesting events so that the event rate being written to tape data storage is reduced to about 1 kHz. This section describes trigger and data acquisition system in the ATLAS experiment.

The ATLAS trigger system was a three-tiered system in Run-1 and is shown in figure 2.6. Level 1 (L1) was a hardware based trigger, selecting interesting events using track and energy information constructed in dedicated fast trigger systems. The L1 trigger had a maximum accept rate of 70 kHz within a latency of 2.5 μs, and defines Region-of-Interest (RoI)[29] as the geographical location of particle candidate. Then the objects were reconstructed at the Level 2 (L2) combining more detailed information only available in the RoI. Thus the output rate at L2 was 6.5 kHz, the average processing time 50 ms. Finally, the trigger objects are reconstructed using full event information at the Event Filter (EF), where precise offline-like algorithm is applied. The EF has an output rate of 1 kHz and an average processing time of 4 s.

The L2 and EF selections were executed on two separate computer farms in Run-1. In Run-2, they have been merged into a single High-Level Trigger (HLT) farm. The logic of the HLT underlying the trigger decision is similar to the case of Run-1.

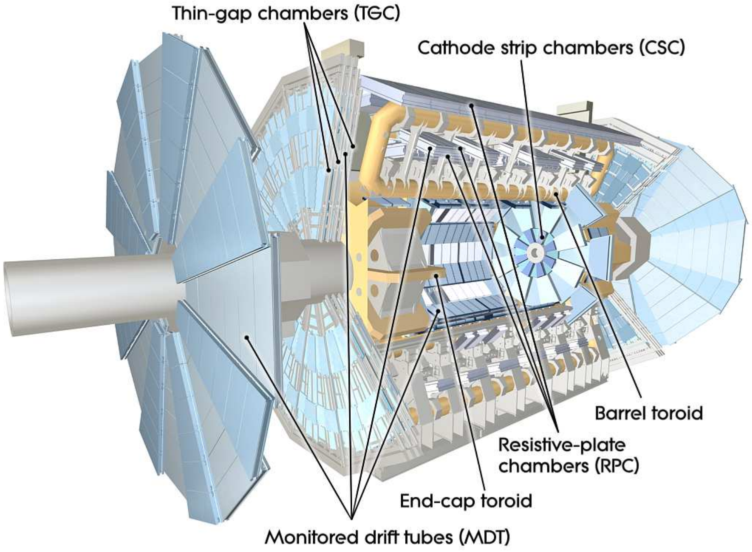

(a)

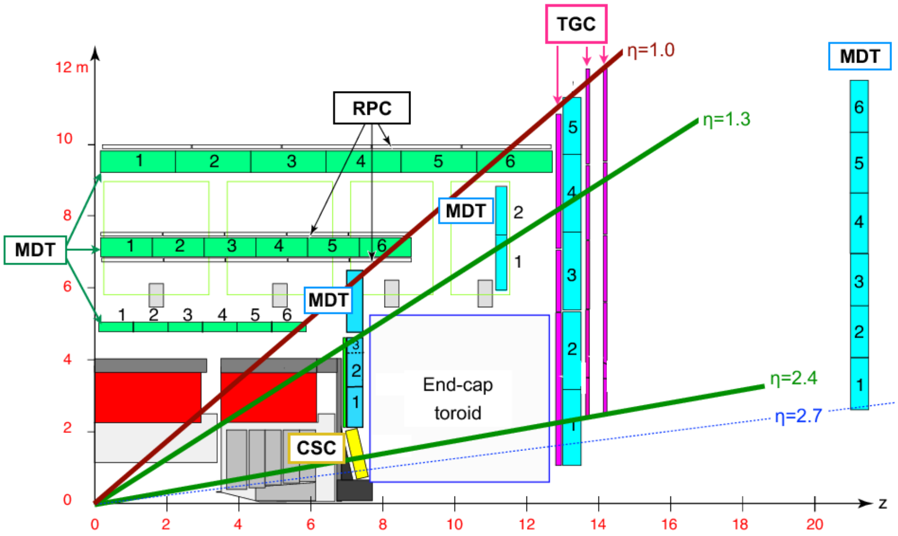

(b)

Figure 2.5: Schematics of the muon spectrometers.

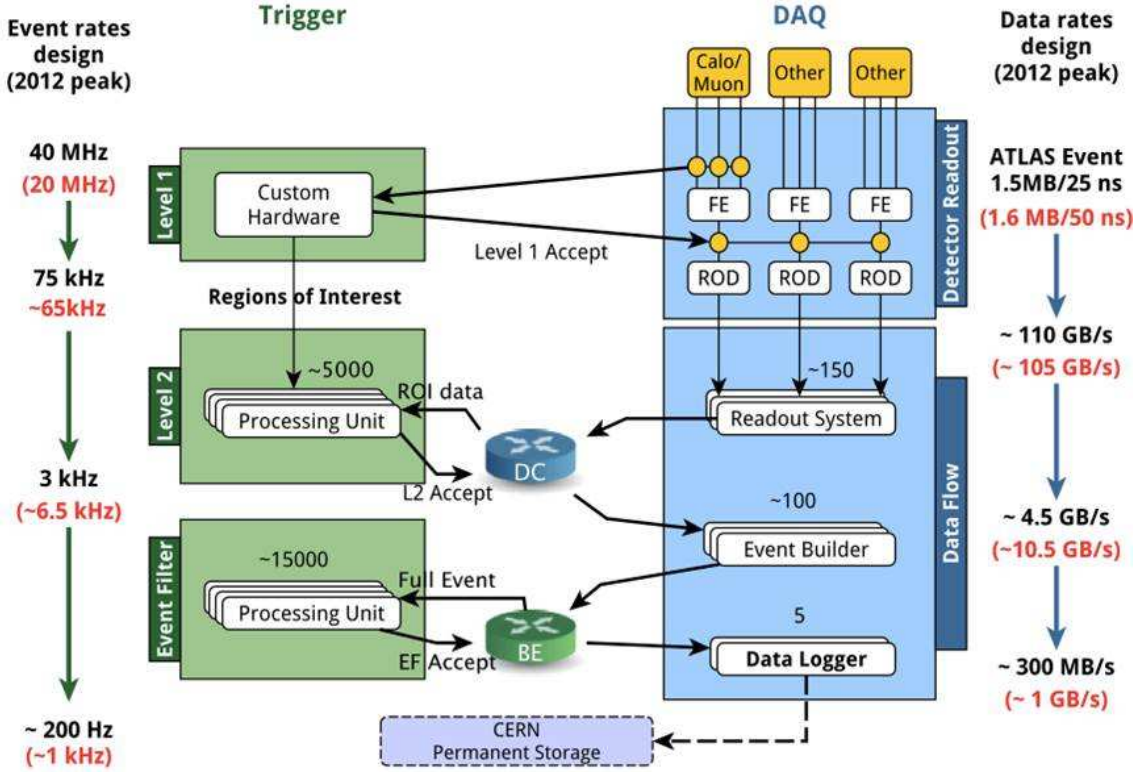

Figure 2.6: Outline of the trigger and the data acquisition systems in Run-1. The three levels of trigger decisions is shown on the left side. and the flow of data in the data acquisition is on the right side. The design values and the 2012 peak values for the event and data rates are shown in black and red, respectively. The level2 and EF are merged into one system (HLT) in Run-2.

Chapter 3

Object Reconstruction

All the analyses require two charged leptons in the final state, as well as a missing transverse momentum. This chapter describes the definitions of the objects used in the analyses.

3.1 Muons

3.1.1 Reconstruction and identification

Muon is reconstructed independently in the inner detectors and muon spectrometers. After the reconstruction, the information from different subdetectors is combined to form the muon tracks that are used in physics analyses. Four reconstruction methods, Combined (CB), Segment-tagged (ST), Calorimeter-tagged (CT) and Extrapolated (ME) muons, are defined depending on which subdetectors are used in reconstruction.

- CB muons : track is reconstructed in the inner detector (ID) and muon spectrometer independently, and a combined track is made with a global refit that uses the hits from both subdetectors.
- ST muons : if a track in the ID is associated with at least one local track segment in the MDT or CSC chambers, it is defined as a ST muon. ST muons are usually used for low p_{T} muons and muons outside the spectrometer acceptance.
- CT muons : a track in the ID is defined as a CT muon if it can be matched to an energy deposit in the calorimeter compatible with a MIP.
- ME muons : a track is only reconstructed in the muon spectrometer and ME muon is applied loose requirement on compatibility with originating from the interaction point. In this case, three hits layers of muon spectrometers are required in the forward region, although the muon is usually required to traverse at least two layers of muon spectrometers.

Reconstructed muons include many backgrounds that are mainly from pion and kaon decays. Thus identification selection is also required. For muon identification, Loose, Medium and Tight are defined.

- Loose muons : CT and ST muons in the $|\eta| < 0.1$ region are classified as Loose. All CB and ME muons satisfying the Medium requirements are included in the Loose selection. In the region $|\eta| < 2.5$, roughly 97.5% of the Loose muons are combined muons, approximately 1.5% are CT and the remaining 1% are reconstructed as ST muons.

- Medium muons : Only CB and ME tracks are used. The tracks are required to have $>$ 3 hits in at least two MDT layers, except for the region $|\eta| < 0.1$, where tracks with at least one MDT layer but no more than one MDT hole layer are allowed. At least three MDT/CSC hit layers are required in the $2.5 < |\eta| < 2.7$ region to extend the acceptance outside the inner detector geometrical coverage. In addition, the q/p (significance), which is defined as the absolute value of the difference between the ratio of the charge and momentum of the muons measured in the inner detector and muon spectrometer divided by the sum in quadrature of the corresponding uncertainties, is required to be less than seven to suppress the contamination due to hadrons misidentified as muons.

- Tight muons : CB muons with hits in at least two stations of the muon spectrometers and muons passing the Medium selection criteria are considered. Furthermore, a two-dimensional cut in the ρ' and q/p (significance) variables is applied as a function of the muon p_{T}, where ρ' is defined as the absolute value of the difference between the transverse momentum measured in the inner detectors and muon spectrometers divided by the p_{T} of the combined track.

Figure 3.1 shows the reconstruction efficiency for muons with $p_{\mathrm{T}} > 10$ GeV passing the Medium selection criteria. Muon reconstruction efficiency is measured by tag-and-probe method using dimuon events. When the muon is used for physics analyses, correction is required to correct the difference of reconstruction efficiency between the simulation and the data. The correction factor is computed using data and MC efficiencies as shown in Figure 3.1.

The simulation can reproduce the muon momentum as measured by the ATLAS detector. However, small difference between data and the simulation appears. Thus the muon momentum is calibrated with $Z \to \mu\mu$ events for high p_{T} muons and $J/\psi \to \mu\mu$ events for low p_{T} muons to verify agreement between data and simulation. The detail can be seen in ref. [30]. Figure 3.2 shows the invariant mass distributions for $Z \to \mu\mu$ and $J/\psi \to \mu\mu$ candidates, and shows a comparison between uncorrected and corrected simulation distributions. Corrected simulation is in good agreement with data even though raw simulation has a maximum difference of 10-20% with the data.

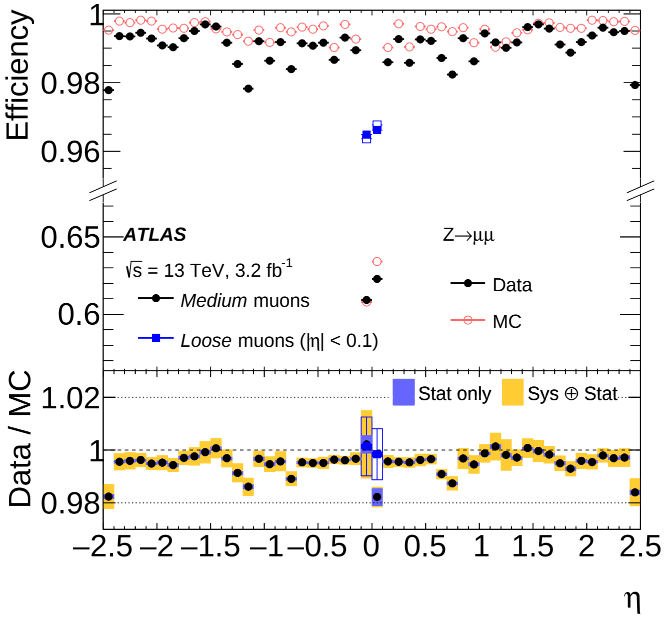

Figure 3.1: Muon reconstruction efficiency as a function of η measured in $Z \rightarrow \mu\mu$ events for muons with $p_{\mathrm{T}} > 10$ GeV shown for the Medium muon selection. The error bars on the efficiencies indicate the statistical uncertainty. The plot at the bottom shows the ratio of the measured to predicted efficiencies, with statistical and systematic uncertainties[30].

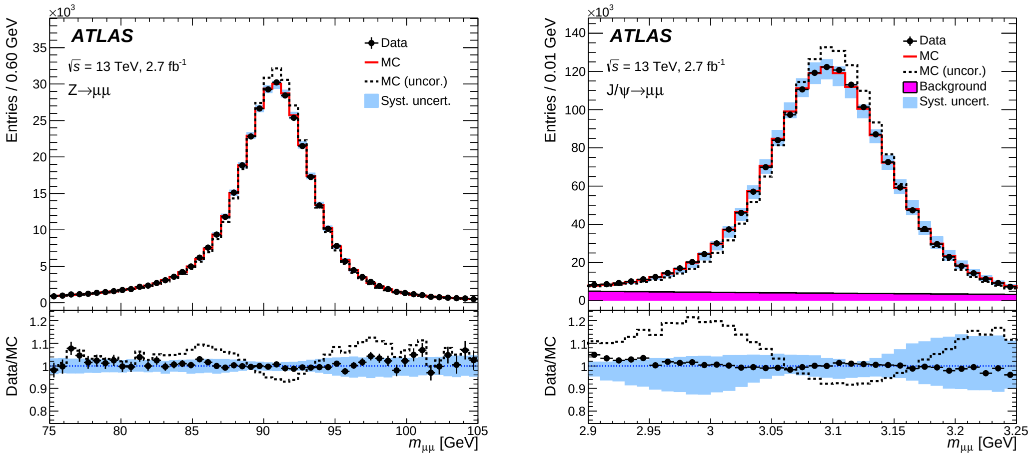

(a)

(b)

Figure 3.2: Invariant mass distribution of (a) the Z boson and (b) the J/ψ with events which have two combined muons. Dashed curves are for uncorrected simulation[30].

3.1.2 Object selection

In $Z + E_{\mathrm{T}}^{\mathrm{miss}}$ analyses, further selections are applied to suppress the background events. The muon object selections are summarized in table 3.1.

A transverse momentum p_{T} greater than 20 GeV and $|\eta| < 2.5$ are required as a kinematics cut, since muons associated with ZH or high mass resonance productions have high momentum. η selection is applied to select quality muons reconstructed with the inner detector as well.

Many cosmic muons constantly traverse the ATLAS detector. To suppress these background and non-prompt muons, a selection on the impact parameters with respect to the primary vertex is applied to the muon track in the inner detector, $|d_0/\sigma_{d_0}| < 3$ and $|z_0 \cdot \sin\theta| < 0.5$ mm. Here, d_0 is the transverse impact parameter, σ_{d_0} is its errors, z_0 is the longitudinal impact parameter and θ is the polar angle.

Finally, the muon is required to be isolated in order to avoid muons associated with jets. To apply the isolation cut, two variables are considered. One is the track-based isolation variable, $p_{\mathrm{T}}^{\mathrm{varcone30}}$, defined as the scalar sum of the transverse momentum of the tracks with $p_{\mathrm{T}} > 1$ GeV in a cone size $\Delta R = 0.3$. The other one is the calorimeter-based isolation variable, $E_{\mathrm{T}}^{\mathrm{topocone20}}$, defined as the sum of the transverse energy of topological clusters in a cone of size $\Delta R = 0.2$ around the muon. The selection is to achieve 99% efficiency for all the signal samples in η and p_{T} using $p_{\mathrm{T}}^{\mathrm{varcone30}}/p_{\mathrm{T}}^{\mu}$ and $E_{\mathrm{T}}^{\mathrm{topocone20}}/p_{\mathrm{T}}^{\mu}$.

Table 3.1: Summary of the muon object selections

Identification	Combined muon with Medium quality
Kinematic	$p_{\mathrm{T}} > 20$ GeV and $\|\eta\| < 2.5$
Impact parameter	$\|d_0/\sigma_{d_0}\| < 3$ and $\|z_0 \cdot \sin\theta\| < 0.5$ mm
Isolation	99% efficiency in η and p_{T} using $p_{\mathrm{T}}^{\mathrm{varcone30}}/p_{\mathrm{T}}^{\mu}$ and $E_{\mathrm{T}}^{\mathrm{topocone20}}/p_{\mathrm{T}}^{\mu}$.

3.2 Electrons

3.2.1 Reconstruction and identification

Electrons are reconstructed by matching the inner detector track to an energy cluster in the electromagnetic calorimeter.

The seed cluster of the electron is searched with a sliding window with a size of 3 × 5 in units of 0.025 × 0.025 in $\eta \times \phi$ space corresponding to the granularity of the electromagnetic calorimeter middle layer. The total cluster transverse energy is required to be above 2.5 GeV.

The track reconstruction is performed with the pattern recognition and the track fit. The pattern recognition uses the pion hypothesis for energy loss due to interactions with the detector material. If a track seed with a transverse momentum larger than 1 GeV can not be successfully extended to a full track of at least seven hits using the pion hypothesis and it falls within one of the electromagnetic cluster region of interest, a second attempt is performed with the new pattern recognition using an electron hypothesis that allows for larger energy loss. Track candidates are then fit either with the pion hypothesis or electron hypothesis, using the ATLAS Global χ^2 Track Fitter [34].

The reconstructed track with the above method is loosely matched to electromagnetic clusters using the distance in η and ϕ between the positions.

To separate the signal-like objects or background-like objects, algorithms for electron identification are applied. The electron identification algorithms use the variables related to the electron cluster, shower shapes in calorimeter, information of the TRT, track-cluster matching quality, track property, and so on. The electron identification algorithm is based on the likelihood method which is a multivariate analysis technique. The multivariate analysis evaluates several properties of the electron candidates when making selection decision. Three levels of identification operating points Loose, Medium and Tight are prepared using the output of likelihood method. Figure 3.3 shows the efficiency for all the electron identification working points.

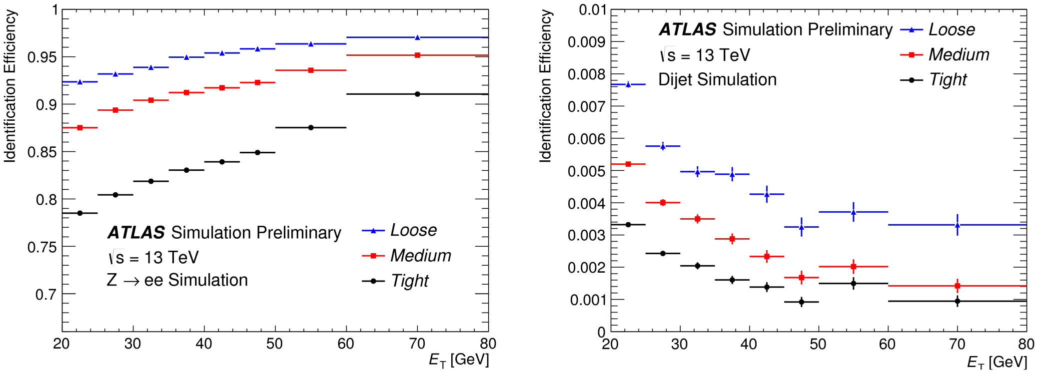

(a) (b)

Figure 3.3: The efficiency to identify electrons from $Z \to ee$ decays (a) and the efficiency to identify hadrons as electrons estimated using simulated di-jet samples (b).

Figure 3.4 shows the reconstruction efficiency. Electron reconstruction efficiency is measured by tag-and-probe method using di-electron events. The electron momentum is also calibrated with $Z \to ee$ events as the same with muon reconstruction.

3.2.2 Object selection

The object selections are applied in addition to the reconstruction method to suppress the background. To ensure higher physics potential in $Z + E_{\mathrm{T}}^{\mathrm{miss}}$ analyses, kinematics selection is

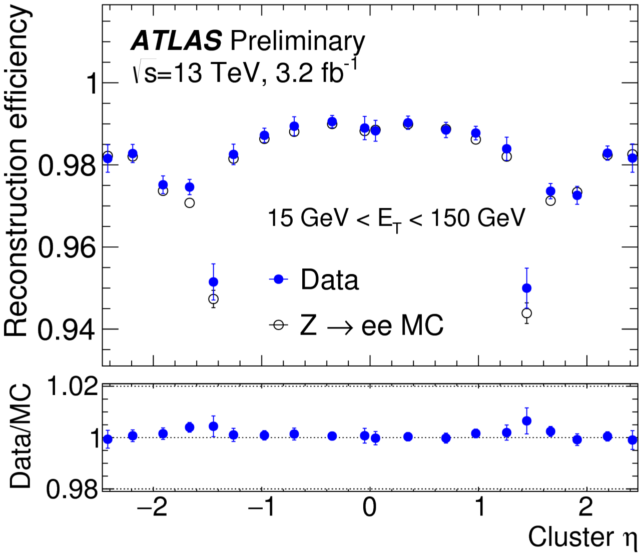

Figure 3.4: Reconstruction efficiency as a function of η for 15 GeV $< E_{\mathrm{T}} <$ 150 GeV. Both statistical and systematic uncertainties are considered[31].

applied as $E_{\mathrm{T}} > 20$ GeV and $|\eta| < 2.47$. The required η region corresponds to the electromagnetic calorimeter region. The quality of electron can be maintained with this η selection. To suppress the contribution from non-prompt electrons, a cut on the impact parameters with respect to the primary vertex is applied to the electron track in the inner detector, specifically $|d_0/\sigma_{d_0}| < 5$ and $|z_0 \cdot \sin\theta| < 0.5$ mm are required. Electrons are also required to be isolated with respect to other tracks and calorimeter cluster. The object selections for electrons are summarized in table 3.2.

Table 3.2: Summary of the electron object selections

Identification	Likelihood Medium
Kinematic	$p_{\mathrm{T}} > 20$ GeV and $\lvert\eta\rvert < 2.47$
Impact parameter	$\lvert d_0/\sigma_{d_0}\rvert < 5$ and $\lvert z_0 \cdot \sin\theta\rvert < 0.5$ mm
Isolation	99% efficiency in η and p_{T} using $p_{\mathrm{T}}^{\mathrm{varcone30}}/p_{\mathrm{T}}^{\mu}$ and $E_{\mathrm{T}}^{\mathrm{topocone20}}/p_{\mathrm{T}}^{\mu}$.

3.3 Jets

The particles which can feel the strong interaction is measured as the aggregation of hadrons called jet. This section describes the jet identification, and the object selections.

3.3.1 Reconstruction and identification

Jets are reconstructed with the anti-k_{T} algorithm [35] with energy depositions in the calorimeters. The anti-k_{T} algorithm considers all particles as jet candidates. In the anti-k_{T} algorithm, the following two parameters are introduced.

$$d_{ij} = min(k_{Ti}^{2p}, k_{Tj}^{2p})\frac{\Delta R_{ij}^2}{R^2} \tag{3.1}$$

$$d_{iB} = k_{Ti}^{2p} \tag{3.2}$$

where, k_{Ti} is the transverse momentum of i, $R_{ij}^2 = (\eta_i - \eta_j)^2 + (\phi_i - \phi_j)^2$, R is the radius parameter of the jet, and d_{iB} is the distance between the particle and the beam. p is the constant value. The jet reconstruction is split into several algorithms based on this value, p can be defined as -1, 0 and 1. If d_{iB} is smaller than d_{ij} is not clustered into j. On the other hand, if d_{iB} is larger than d_{ij}, i is clustered into j. The axis of j would undergo recalculation after clustering. This procedure would repeat until all the particles are clustered into jets. In $Z+E_{\mathrm{T}}^{\mathrm{miss}}$ analyses, the radius parameter of the jet R is defined as 0.4. To ensure the quality of jets, events that have jets built from noisy calorimeter cells are removed. In addition, large-R jets are trimmed to minimize the impact on the large-R jets that are from energy depositions from pile-up interactions not associated with the original shower.

Reconstructed jets are also applied the quality selection to remove fake jets. Two quality selections are proposed, called BadLoose and BadTight jet selections. A jet is identified as a BadLoose jet if it satisfies at least one of following criteria

- $f_{HEC} > 0.5$ and $|f_Q^{HEC}| > 0.5$ and $\langle Q \rangle > 0.8$
- $|E_{neg}| > 60$ GeV
- $f_{EM} > 0.95$ and $f_Q^{LAr} > 0.8$ and $\langle Q \rangle > 0.8$ and $|\eta| < 2.8$
- $f_{max} > 0.99$ and $|\eta| < 2$
- $f_{EM} < 0.05$ and $f_{ch} < 0.05$ and $|\eta| < 2$
- $f_{EM} < 0.05$ and $|\eta| \geq 2$

where, f_{HEC} ,the energy fraction in the hadronic calorimeter is defined as the ratio of the energy deposited in the hadronic calorimeter to the total energy. Similarly, f_{EM}, the energy fraction in the electromagnetic calorimeter. f_{max} is the maximum energy fraction in any single calorimeter. $\langle Q \rangle$, the average jet quality is defined as the energy-squared weighted average of the pulse quality of the calorimeter cells in the jet. f_Q^{LAr} and f_Q^{HEC} are fraction of the energy in the LAr calorimeter and hadronic calorimeter, respectively. Finally, f_{ch} is charged fraction defined as the ratio of the scalar sum of the p_{T} of tracks coming from the primary vertex associated to the jet divided by the jet p_{T}.

The first two selections are required to identify jets mainly due to sporadic noise bursts in the hadronic calorimeter. The third selection has the purpose to identify jets to large coherent noise or isolated pathological cells in the electromagnetic calorimeter, The last three requirements are more general and are used to identify hardware issues, beam-induced background and cosmic muon showers. The BadTight selection is designed to provide a much higher fake jet rejection with an inefficiency for good jets. It adds a single criterion which is based on the ratio between the f_{ch} and f_{max} Figure 3.5 shows the jet quality selection efficiencies as a function of η for p_{T} >100 GeV. Jet are first calibrated to the hadronic scale with the effect of

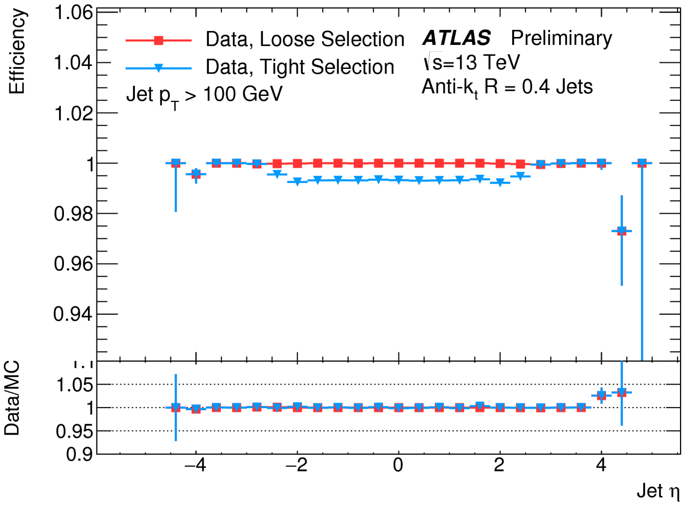

Figure 3.5: Jet quality selection efficiency for anti-k_{T} jets with R = 0.4 measured with a tag-and-probe method as a function of η for p_{T} >100 GeV, for the Loose and Tight selection criteria[32].

removing pile-up, then in-situ techniques are used to obtain calibration constants that correct MC to obtain a better agreement with data.

3.3.2 b-jets identification

The B-hadron produced in LHC can travel a few millimeters in the transverse plane from the primary vertex before decaying since it has a long proper lifetime distance of $c\tau = 470 - 500$ μm. Therefore the tracks from the B-hadron decay originate from a displaced secondary vertex. The d_0 of the tracks associated with the b jets tend to take large values in comparison with those associated with light jets. Figure 3.6 shows a sketch of a jet from a long-lived particle decay. Furthermore, B-hadrons have large mass. Therefore the decay products can have large transverse momentum with respect to the jet axis. To separate the b-jets, a Boosted Decision Tree (BDT) algorithm which is one of multi-variate analysis methods is applied. The variables to separate the flavor of jets are basically related to the above b-jet properties. The detail of the variables are described in ref. [36].

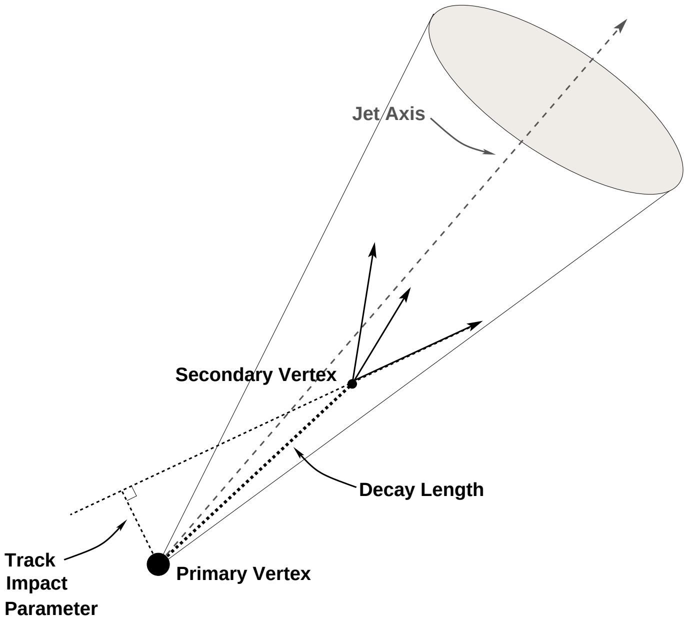

Figure 3.6: A secondary vertex with a significant decay length indicates the presence of a long-lived particle in the jet. The secondary vertex is reconstructed from tracks with a large impact parameter significance with respect to the primary vertex[33].

Figure 3.7 shows the b-tagging BDT output for the b-jets, c-jets and light-flavor-jets. The simulation is the $t\bar{t}$ events and adjusted to describe better the data. The b-jet can be efficiently selected with small probabilities for the other jets contributions in high output region.

3.3.3 Object selections

$Z + E_{\mathrm{T}}^{\mathrm{miss}}$ analyses do not include the jet object at the final objects. However, properties of jet have a pottential to separate the signal with the background, and are used for the computation of missing transverse momentum. Thus the jet object selection is important in $Z + E_{\mathrm{T}}^{\mathrm{miss}}$ analyses.

Kinematic selections are jet $p_{\mathrm{T}} > 20$ GeV, and reconstructed in the region $|\eta| < 4.5$ which consistent to the acceptance of the calorimeter. To reduce the pile-up jets, jet-vertex-fraction (JVF) selection is applied. The JVF is defined as the scalar sum of the transverse momentum

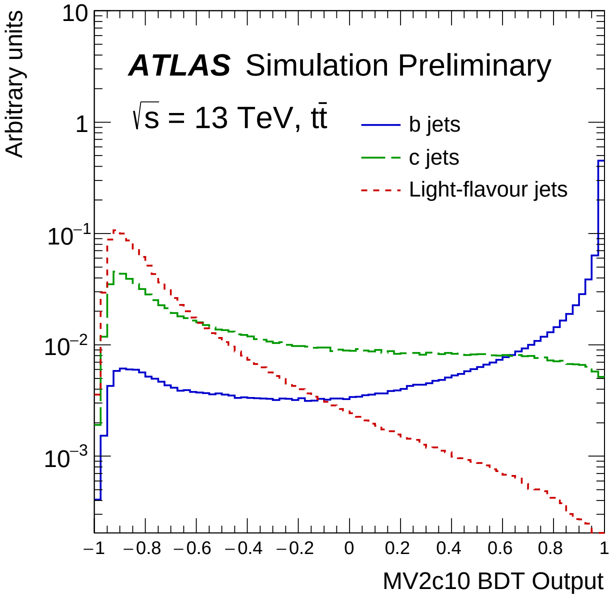

Figure 3.7: B-tagging BDT output for b-jets (blue), c-jets (green) and light-flavor-jets (red) using $t\bar{t}$ simulation.

of the tracks associated to the jets and originating from the hard-scattering vertex, divided by the scalar sum of the transverse momentum of all the tracks. The JVF is combined with other variables in a multivariate discriminant called Jet Vertex Tagger (JVT)[37] which is then used in the corresponding tool at the analysis level to select jets from the hard-scatter vertex. The JVT selection is 0.59 for jets with $p_{\mathrm{T}} < 60$ GeV and $|\eta| < 2.4$, which correspond to an efficiency of 92% with an observed fake rate of 2%. Finally, jets are retained in the analyses only if they pass the loose selection criteria which is described in the previous section before.

The jets object selections are summarized in the table 3.3

Table 3.3: Summary of the jet object selections

Kinematic	$p_{\mathrm{T}} > 20$ GeV and $\lvert\eta\rvert < 4.5$
Pileup removal	JVT > 0.59 for $p_{\mathrm{T}} < 60$ GeV, $\lvert\eta\rvert < 2.4$ jets
Identification	Loose jets accepted

3.4 Overlap removals

The reconstruction algorithms described before are at first conducted independently. Thus the same tracks or clusters may be reconstructed as more than one objects. For example, b-jet may be reconstructed as a muon in addition to b-jet since a b-jet is often associated with decay muons. In this case, the objects should be reconstructed as b-jet because muon is a part of the b-jet. To remove such case, overlap removal selection is also applied.

Table 3.4 shows the summary of the overlap removal strategy used in the analyses. Here pile-up jets check means JVT > 0.59 if the jet $p_{\mathrm{T}} < 60$ GeV and $|\eta| < 2.4$.

	Reference objects	Criteria
Remove jets	electrons	$\Delta R_{e-\mathrm{jet}} < 0.2$
	muons	$\Delta R_{\mu-\mathrm{jet}} < 0.2$ if $N_{\mathrm{Trk}}(jet) < 3$ OR ($p_T^{jet}/p_T^{\mu} < 2$ and $p_T^{\mu}/\Sigma_{\mathrm{TrkPt}} > 0.7$)
Remove electrons	jets	$0.2 < \Delta R_{e-\mathrm{jet}} < 0.4$ **AND** pile-up jets check
	muons	share the same ID track
remove muons	jets	$\Delta R_{\mu-jet} < 0.4$ **AND** pile-up jets check

Table 3.4: Summary of the overlap removal selection adopted in the analyses.

3.5 Missing transverse momentum

In the LHC, momentum conservation in the transverse plane to the beam axis implies that the transverse momentum of the collision products should sum to zero. Thus, a particle escape from detector, is characterized by the missing transverse momentum $E_{\mathrm{T}}^{\mathrm{miss}}$ computed as momentum imbalance in the transverse plane. This section describes the reconstruction of the missing transverse momentum.

3.5.1 Reconstruction

The missing transverse momentum is reconstructed by selecting calibrated hard objects, and calculated as the following equation :

$$\boldsymbol{E}_{\mathbf{T}}^{\mathbf{miss}} = -\boldsymbol{E}_{\mathbf{T}}^{\boldsymbol{e}} - \boldsymbol{E}_{\mathbf{T}}^{\boldsymbol{\gamma}} - \boldsymbol{E}_{\mathbf{T}}^{\boldsymbol{\tau}} - \boldsymbol{E}_{\mathbf{T}}^{\mathbf{jets}} - \boldsymbol{E}_{\mathbf{T}}^{\boldsymbol{\mu}} - \boldsymbol{E}_{\mathbf{T}}^{\mathbf{soft}}, \tag{3.3}$$

where all terms are given by the negative vectorial sum of the object momentum. All missing transverse momentum are computed with the objects passing the object selections except for the soft term. The soft term is reconstructed from the detector signal objects not associated with any object. The soft term is basically built from the inner detector track information. The tracks and vertex to build the soft term are required to pass the following selections :

- track $p_{\mathrm{T}} > 0.4$ GeV and $|\eta| < 2.5$
- $|d_0| < 1.5$ cm and $|z_0| < 1.5$ cm
- Tracks within ΔR(track, electron/photon cluster) < 0.05 are removed.
- Tracks within ΔR(track, τ-lepton) < 0.2 are removed.
- ID tracks associated to combined or segment-tagged muons are replaced with the combined the inner detector and the muon spectrometer fit.
- Tracks associated with jets using the ghost-association technique [38, 39] are removed.
- tracks with momentum uncertainties larger than 40% are removed.

Figure 3.8 shows the missing transverse momentum distribution[40]. The difference between data and the simulation in the low $E_{\mathrm{T}}^{\mathrm{miss}}$ region is caused by the multi-jet background which is not included in the simulation.

The $E_{\mathrm{T}}^{\mathrm{miss}}$ resolution is evaluated in $Z \to \mu\mu$ events. Figure 3.9 shows the $E_{\mathrm{T}}^{\mathrm{miss}}$ resolution as a function of ΣE_{T} and number of primary vertices, respectively.

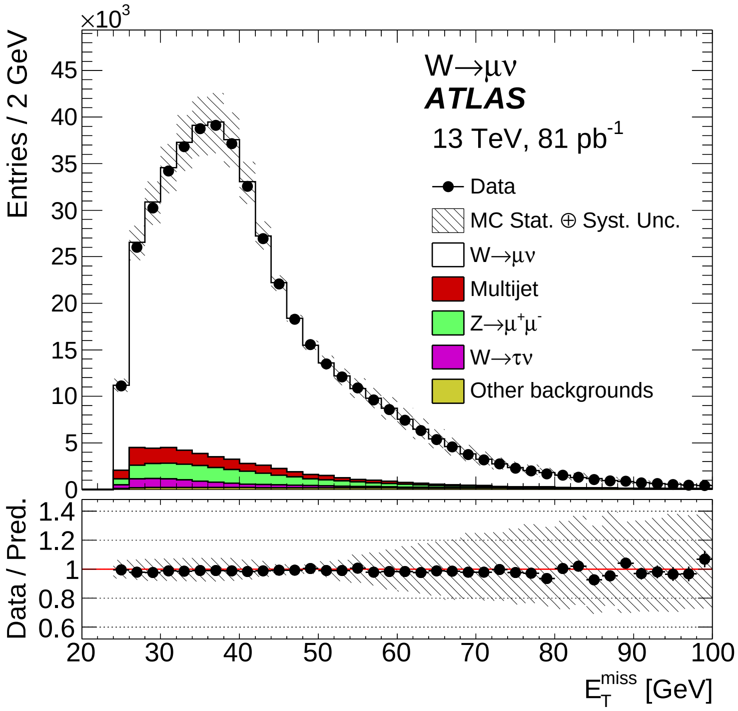

Figure 3.8: Distributions of the missing transverse momentum in $W \to \mu\nu$[40].

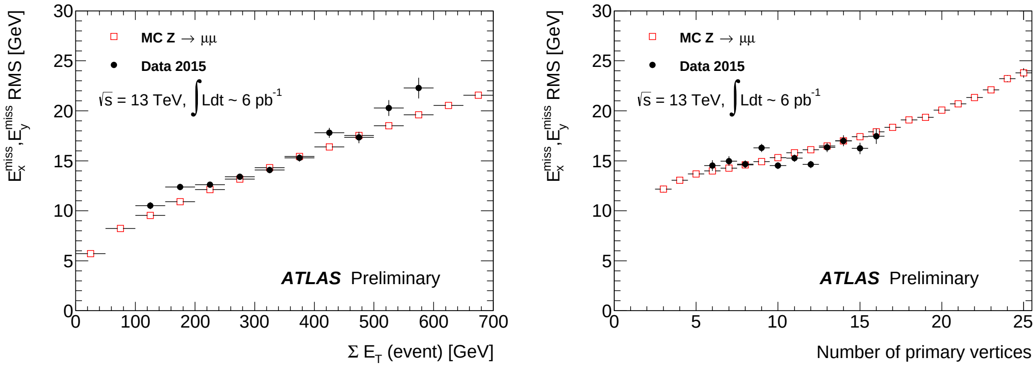

(a)

(b)

Figure 3.9: Distributions of missing transverse momentum resolution as a function of ΣE_T and of the number of primary vertices in $Z \to \mu\mu$ events[41].

Chapter 4

Signal and Background Processes

This section describes the definition of signal and backgrounds in $Z + E_{\mathrm{T}}^{\mathrm{miss}}$ analyses, and the data samples recorded with the ATLAS detector and the simulation samples. Monte Carlo samples have been used to simulate all the background and signal processes, and have been generated for a center-of-mass energy of 13 TeV and passed through the full GEANT4 simulation [42] of the ATLAS detector.

4.1 ATLAS data sample

The data samples used consist of the full integrated luminosity collected by ATLAS in 2015, and the part of the data in 2016 during 25 ns proton-proton collisions in the LHC. The sample corresponds to 13.3 fb^{-1} of luminosity. Data are required to satisfy specific quality conditions which collect all the luminosity blocks with all the sub-detectors working with a high efficiency.

4.2 Signal processes

4.2.1 ZZ resonance search

The resonance search has a potential to inclusively search for many physics beyond the Standard Model. In this analysis, heavy Higgs boson and spin-2 Kaluza-Klein (KK) graviton are assumed as the signal.

An additional heavy Higgs boson is searched in the mass range $300 < m_H < 1000$ GeV, because $\ell\ell\nu\nu$ channel has the highest sensitivity in the Z boson pair production channel in the region above 500 GeV due to the larger branching with respect to $\ell\ell\ell\ell$, and cleaner event topology than $\ell\ell qq$ and $\nu\nu qq$. The heavy Higgs boson signal is assumed as Narrow Width Approximation (4.7 MeV), which is a resonance with a width narrower than the experimental detector resolution. The heavy Higgs boson in the gluon-fusion in $Z + E_{\mathrm{T}}^{\mathrm{miss}}$ final state is generated by POWHEG-BOX v2 [43] up to next-to-leading order. Parton shower and hadronisation is modeled by PYTHIA 8.186[44]. bottom and charm hadron decays are simulated by EVTGEN v1.2.0 [45]. The parton distribution function is modeled by the CT10[46]. Samples are generated for several mass point in the m_H interval of 300-1000 GeV.

The graviton production is modeled with MADGRAPH5 AMC@NLO b2.2.2 [47]. Generator-parameter values and PDF set are the A14 [48] and NNPDF2.3LO [49] are used, respectively. In the RS framework, a dimensionless coupling constant $\kappa/\bar{M}_{Pl}$ is introduced as a voluntary parameter, where κ is the curvature of the warped extra-dimensions and $\bar{M}_{Pl}$ is the reduced Plank mass. In the simulation, the parameter $\kappa/\bar{M}_{Pl}$ is assumed as 1.

4.2.2 Invisible particle searches

The Higgs invisibly decaying and mono-Z search are assumed as the signal, and performed using the same events due to their similar phase space.

The signal in the Higgs invisibly decaying is simulated assuming the Standard Model Higgs decaying to $\nu\nu\nu\nu$ with a branching fraction of 100%. The production of the Standard Model Higgs boson in association with a Z boson and its decay are modeled with POWHEG-BOX v2. The signal is simulated at NLO in perturbation theory using the MiNLO [50]. However the NNLO QCD and NLO electroweak corrections are applied to the cross section. The cross section is assumed as $89.31^{+3.8}_{-3.0}$fb (QCD) ± 3fb (PDF) taken from Ref [51, 52, 53].

The mono-Z production is simulated with MADGRAPH5 [54]. The Dirac fermion WIMP particle χ interacts with the Standard Model particles via an unknown massive mediator η. We focus on the Vector-mediator model, where the dark matter candidate is produced via the exchange of a neutral spin-1 mediator in the s-channel. The coupling parameters have been set to $g_\chi = 1.0$ and $g_q = 0.25$, for the coupling between the mediator and the dark matter, and the coupling between the mediator and the Standard Model particles, respectively. The mass of the mediator m_{med} is considered in the region between 10 and 10000 GeV, and the dark matter mass m_χ is varied in the region between 1 and 1000 GeV. The cross section is computed with the leading order. The PDF set is NNPDF3.0 [49].

4.3 Background processes

In the $Z + E_{\mathrm{T}}^{\mathrm{miss}}$ analyses, the following topologies can be the backgrounds :

- 2 real leptons + $E_{\mathrm{T}}^{\mathrm{miss}}$
- 1 real lepton + 1 fake lepton + $E_{\mathrm{T}}^{\mathrm{miss}}$

This section describes all possible backgrounds in the $Z + E_{\mathrm{T}}^{\mathrm{miss}}$, and the properties of background simulations.

4.3.1 Z boson pair production

The Z boson pair productions from quark-antiquark annihilation have the same objects with both ZZ resonance and invisible particle searches, since Z decays to the same final states. The decay modes $ZZ \to \ell\ell\ell\ell$, $ZZ \to \nu\nu\nu\nu$ and $ZZ \to \ell\ell\nu\nu$ are considered using the POWHEG event generator [55] with AZNLO CTEQ6L1 tune. Phythia8 is used for the parton showering. The NNLO QCD and NLO electroweak corrections are considered by Ref. [56][57] as a function of m_{ZZ}. Figure 4.1 and Figure 4.2 show the NLO electroweak correction function and the NNLO QCD correction function, respectively. The vertical axis is the event weight for m_{ZZ}.

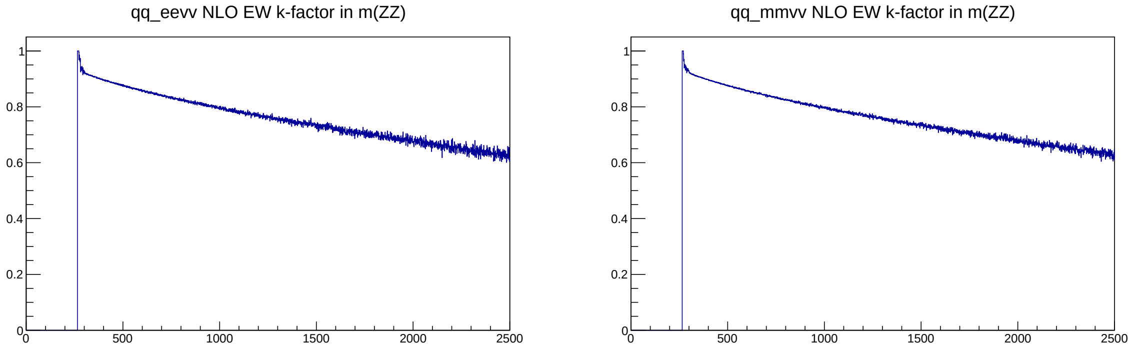

(a)

(b)

Figure 4.1: Function for NLO electroweak corrections to Z boson pair production in the (a) $ee\nu\nu$ and $\mu\mu\nu\nu$ channels as a function of m_{ZZ}.

A minimum mass of 4 GeV is required for the off-shell Z boson.

Furthermore, Z boson pair production in the gluon-fusion is also considered. The background can interfere the off-shell Standard Model Higgs boson in gluon-fusion production. The interference contributions are generated at leading order in perturbative QCD using GG2VV3.1.6 [58, 59] with higher order correction. The CT10 is used for the PDF set to correct higher order QCD effects, 1.7 is applied as a K-factor taken from Ref. [66].

4.3.2 WZ production and W boson pair production

The WZ production with the charged lepton from the W decay escaping from the detection or W decaying hadronically in the case of $W \to \tau\nu$, is the second largest background in $Z + E_{\mathrm{T}}^{\mathrm{miss}}$. Thus the main decay mode is $WZ \to \ell\nu\ell\ell$. The $\ell\nu\nu\nu$ decay mode barely contributes in the signal region. In this case, additional jet imitates a charged lepton. The WZ production is modeled with POWHEG interfaced with Pythia8. The NNLO QCD correction effects to the cross section at the level of 10 % [61]. The WZ production cross section has been measured around 15% higher than the POWHEG prediction [62, 63]. Thus the normalization in the

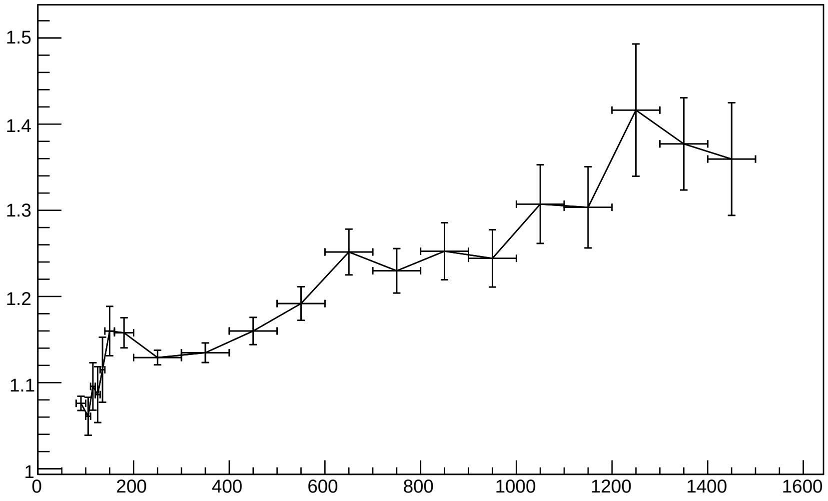

Figure 4.2: Function for NNLO QCD corrections to Z boson pair production.

background control region is defined as described in section 6.2.

The W boson pair production in the final state with both W bosons decaying to leptons $WW \rightarrow \ell\nu\ell\nu$ is also considered. A minimum mass of 4 GeV is required for each charged lepton coupling. The generators are the same as for the WZ sample.

4.3.3 V+jets production

Z+jets background

The events with a di-electron or di-muon pair from Z boson decays and one or more accompanying jets in the final state can be the background due to poorly reconstructed $E_{\mathrm{T}}^{\mathrm{miss}}$. This background can be largely reduced by kinematic selections. However, the Z + jets background has significant systematics uncertainties. Since the modeling of mismeasurement in the Monte Carlo depends strongly on the correct modeling of the detector, pile-up interactions, jet energy response and track reconstruction, Z+jets background is estimated with the data as described in section 6.4.

For the Z+jets process, MADGRAPH [47] event generator is attempted to use with cross checks done using POWHEG generator with AZNLO CTEQ6L1 tune and interfaced with Pythia8 for the parton showering. The simulation generated by POWHEG shows a reasonably good description of inclusive kinematic distributions for leptons and an agreement in the number of jets distribution up to one jet bin. MADGRAPH models the emission of additional partons, and describes the jet multiplicity as well as the jet kinematics better than POWHEG.

However the agreement in Z boson p_{T} distribution is slightly different.

Since the high Z_{P_T} tail can contribute significantly to the signal region, one of the kinematic distributions evaluated from only the generators is statistically not enough. Thus both MADGRAPH and POWHEG samples are used for the background studies. In addition, Z boson p_{T} difference is corrected by bin-by-bin re-weighting as shown in Figure 4.3. The weights are derived for events with exactly two opposite sign electrons and muons with $p_{\mathrm{T}} >$ (30, 20 GeV) for (leading, sub-leading), and $|\eta| < 2.47$ (electrons) and $|\eta| < 2.5$ (muons) respectively. The cut on the di-lepton invariant mass is also applied to select a Z-boson, specifically $75 < m_{\ell\ell} < 106$ GeV. Figure 4.4 shows the resulting effect of Z_{P_T} re-weighting.

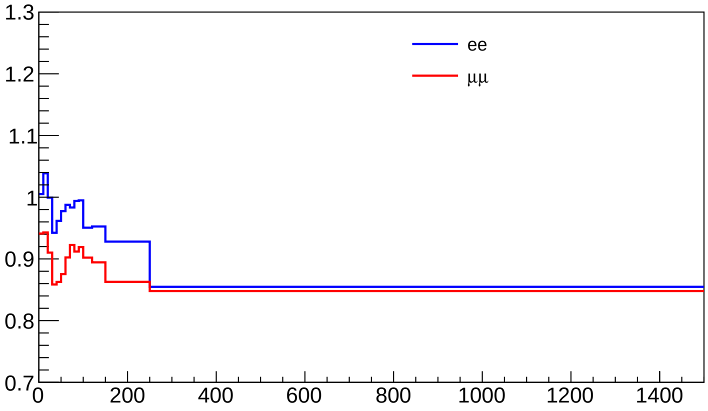

Figure 4.3: Ratio of number of events for Data/(MADGRAPH+POWHEG), in $Z \to ee$ and $Z \to \mu\mu$ decay channels. The x axis is Z_{P_T}.

W+jets production

$W \to e\nu$, $W \to \mu\nu$ and $W \to \tau\nu$ processes can contribute to the signal region if one of the jets is reconstructed as a lepton. W+jets background is simulated using POWHEG-BOX v2. The W+jets cross section is normalized to the NNLO prediction.

4.3.4 Top quark pair and single top production

Background samples of top-pair, single top and Wt productions are simulated using POWHEG interfaced with Pythia6. Perugia2012 tune was used. Events for the top pair production are filtered at the event generator level requiring at least one lepton originating from a W boson and having $p_{\mathrm{T}} > 1$ GeV. Single top production is considered for both s-channel and t-channel. For Wt single top associated production, di-lepton events have been used.

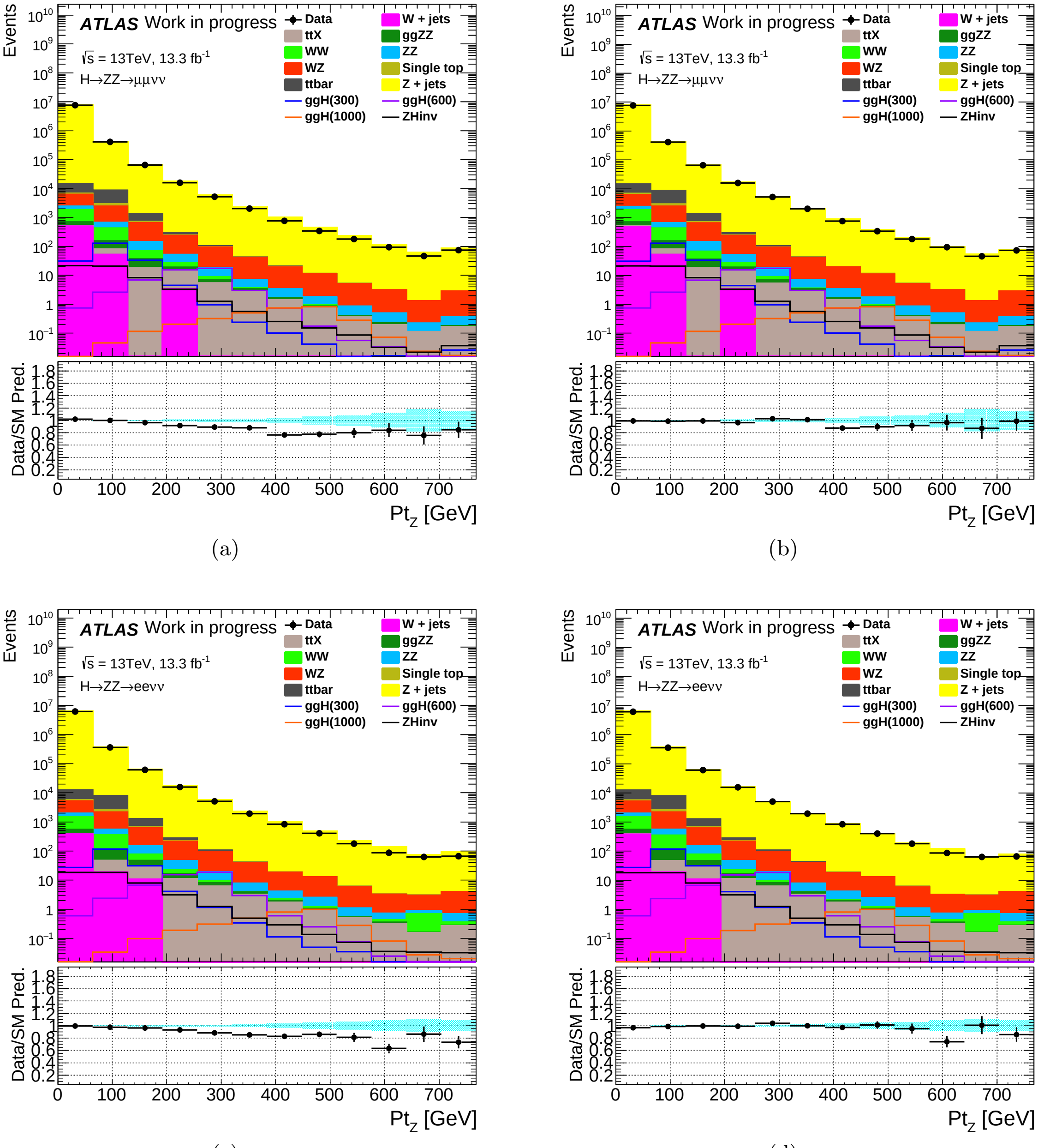

(a)

(b)

(c)

(d)

Figure 4.4: Z_{P_T} distributions before (left) and after (right) the weighting to data. The top plots are for Z decays to muons, bottom plots are for Z decays to electrons.

4.3.5 Other insignificant background

As other insignificant background processes, tri-boson, $t\bar{t}V$ and $t\bar{t}VV$ background are considered.

Tri-boson background

The production of three vector bosons is suppressed by requiring no more than two leptons in the final state. The expected contribution from these samples is then very small, compared to that of the di-boson events. Tri-boson production VVV, with $V = W, Z$, is simulated by SHERPA event generator at NLO.

$t\bar{t}V$ and $t\bar{t}VV$ backgrounds

Background samples for top pair production in association with one or two vector bosons are simulated with MADGRAPH generator interfaced with Pythia8.

Chapter 5

Event Selection

The events used for analyses are selected using variables which have distinctive difference between the signal and background. The event selections were optimized for the ZZ resonance and the dark matter searches independently, since the phase space is different in these analyses. This section describes the event selection for the $Z + E_{\mathrm{T}}^{\mathrm{miss}}$ analyses.

5.1 Event preselection

To exclude events in problematic luminosity blocks, all data events are required to pass certain quality checks. These selections are applied to both $Z+E_{\mathrm{T}}^{\mathrm{miss}}$ analyses. The event preselection is applied to reject non-collision background events and pileup jets, which can give rise to fake $E_{\mathrm{T}}^{\mathrm{miss}}$ and consequently degrade the $E_{\mathrm{T}}^{\mathrm{miss}}$ performance. The primary vertex with at least two associated tracks with $p_{\mathrm{T}} > 400$ MeV is required, where the primary vertex is defined as the vertex with the greatest Σp_{T}^2 associated in the event. In addition, events that have a noise burst in the LAr calorimeter and HV trips in the calorimeter are removed, and events affected by the recovery procedure for single event upsets in the SCT are also removed. Finally the events that are taken with the toroid off are excluded.

5.2 Trigger

The ATLAS takes the data with many kinds of trigger logic. In $Z + E_{\mathrm{T}}^{\mathrm{miss}}$ analyses, two leptons from Z boson decay expected to have high p_{T}. Thus single lepton triggers are chosen for both $Z+E_{\mathrm{T}}^{\mathrm{miss}}$ analyses. The p_{T} threshold of the single lepton trigger needs to be adjusted with the luminosity since the overall trigger rate the ATLAS can manage is limited. Since the LHC luminosity was substantially improved in the data taking period of 13 TeV, the single trigger threshold was changed with the LHC luminosity. The list of trigger requirement is shown in table 5.1.

Table 5.1: Trigger requirement in $Z + E_{\mathrm{T}}^{\mathrm{miss}}$ analyses in 2015 and 2016 data periods. The single lepton triggers were all un-prescaled.

	Trigger selection
Single Muon	mu20_iloose_L1MU15 OR mu50 (2015)
	mu24_ivarmedium OR mu50 (2016)
	mu26_ivarmedium OR mu50 (2016, after $10^{34} cm^{-2} s^{-1}$)
Single Electron	e24_lhmedium_L1EM18VH OR e60_lhmedium OR e120_lhloose (2015)
	e24_lhtight_nod0_ivarloose OR e60_lhmedium_nod0 (2016)
	OR e140_lhloose_nod0 (2016)
	e26_lhtight_nod0_ivarloose (2016, after $10^{34} cm^{-2} s^{-1}$)

For the muon (electron) triggers, the numeral after "mu"("el") means the p_{T} threshold of the muon (electron) in GeV. iloose and ivarmedium mean the isolation requirement as follows :

- iloose : p_{T}cone20/$p_{\mathrm{T}} < 0.12$, where p_{T}cone20 is the p_{T} sum of ID tracks in cone dR = 0.2 excluding muon track itself.
- ivarloose : p_{T}varcone30/$p_{\mathrm{T}} < 0.16$, where p_{T}varcone30 is the p_{T} sum of the tracks in a cone of dR = 10 excluding muon track itself with maximum cone size = 0.3.
- imedium : p_{T}cone30/$p_{\mathrm{T}} < 0.06$, where, p_{T}cone30 is the p_{T} sum of ID tracks in cone dR = 0.3, excluding muon track itself.
- ivarmedium : p_{T}varcone30/$p_{\mathrm{T}} < 0.07$, where, p_{T}varcone30 is the p_{T} sum of the tracks in a cone of dR = 10, excluding muon track itself with maximum cone size = 0.3.

lhloose, lhmedium and lhtight mean the electron qualities according to the result of likelihood identification.

The ATLAS experiment also prepares the di-lepton trigger that requires two leptons, it has a lower p_{T} threshold than the single lepton trigger. However the efficiency to take the signals is much the same as the single lepton triggers for the present analyses. The evaluated trigger efficiencies to take the signals are shown in Figure 5.1 and Figure 5.2.

Figure 5.3 shows the efficiency turn-on curves of the muon triggers. Since non-active layers exist in the barrel region, the efficiency in the barrel region is lower than in the endcap region.

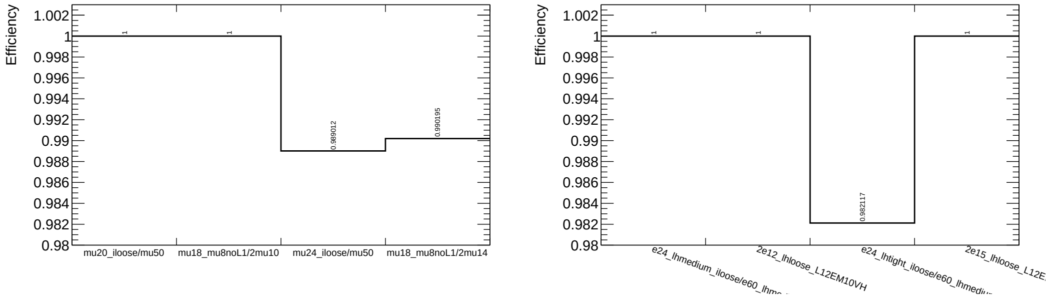

(a)

(b)

Figure 5.1: Efficiency to select the higgs invisibly decaying signal after applying all the kinematic selections in (a) the electron channel and (b) the muon channels.

Figure 5.4 shows the efficiency curves of electron triggers.

In these figures, the trigger scale factor is applied to the MC samples to correct the trigger efficiency difference between the data and the MC. Trigger scale factors are computed using the following equation with events that at least one lepton fired the trigger :

$$SF = \frac{\prod_{n}^{Nleptons}(1-\epsilon_{Data})}{\prod_{n}^{Nleptons}(1-\epsilon_{MC})} \tag{5.1}$$

where ϵ is the trigger efficiency provided as a function of lepton η.

5.3 The variables used for event selections

This section summaries the event selections. The event selection is optimized to reach optimal search sensitivity in all the $Z + E_{\mathrm{T}}^{\mathrm{miss}}$ analyses. The cut based analysis is adopted to the analyses, defining the selection cut off for the variables which have a sensitivity to separate the signal with the background. The variables used for the selection are almost the same for both $Z + E_{\mathrm{T}}^{\mathrm{miss}}$ analyses.

In all of the $Z + E_{\mathrm{T}}^{\mathrm{miss}}$ analyses, events are required to contain exactly two same flavor and oppositely charged muons or electrons that pass the object selections described in section 3.1 and 3.2. Furthermore, to suppress the $ZZ \to \ell\ell\ell\ell$ and $WZ \to \ell\nu\ell\ell$ events, events with a third lepton are vetoed. The p_{T} thresholds and selection criteria for the third lepton are set to be 7 GeV and loose selection criteria for both muons and electrons.

The trigger turn on curve is pretty sharp as shown in Figure 5.3 and Figure 5.4. A lower threshold at 20 GeV on the lepton p_{T} is not on the plateau region. Thus the p_{T} cut on leading lepton to 30 GeV is applied, while the sub-leading lepton is kept to 20 GeV.

To exclude the events that do not include a Z boson (ex. $t\bar{t}$, $WW \to \ell\nu\ell\nu$, etc.), the

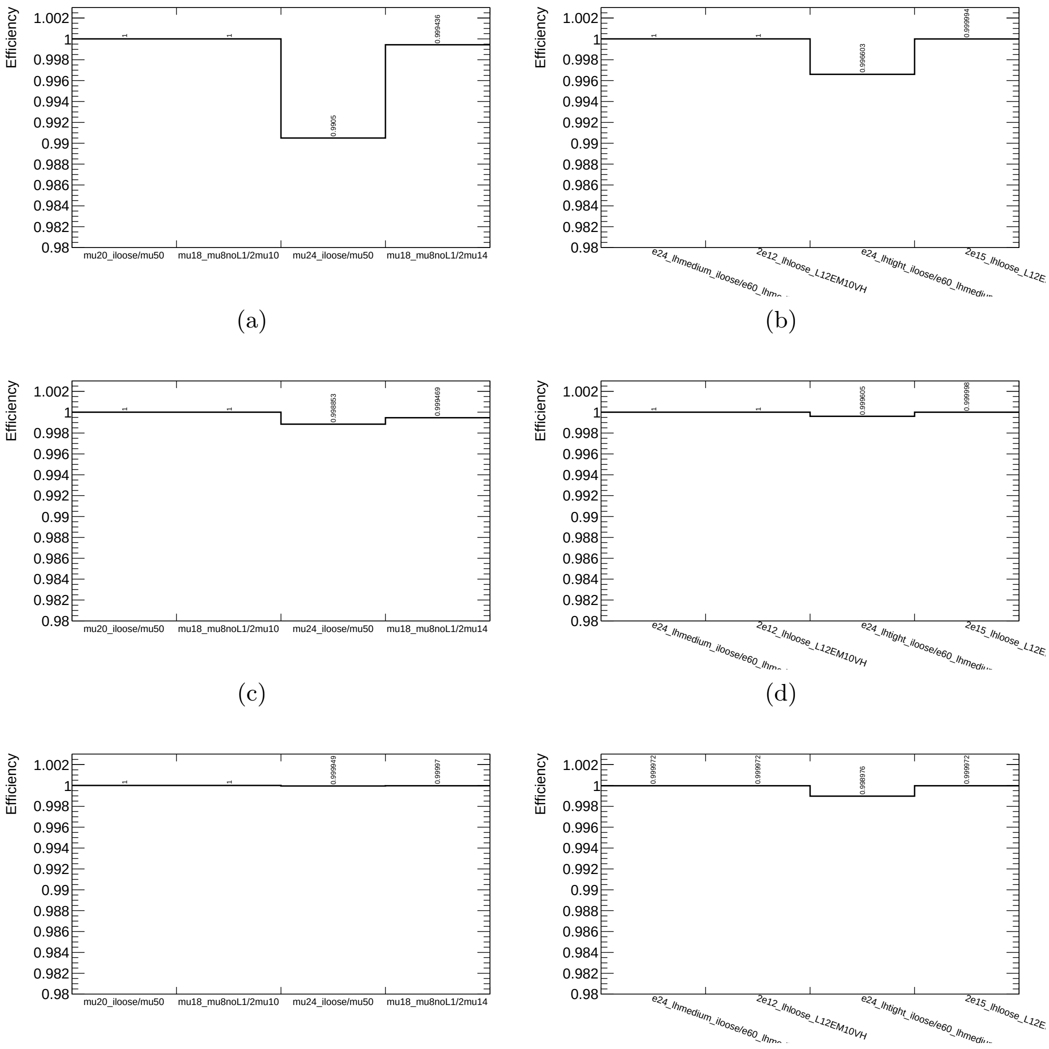

(a)

(b)

(c)

(d)

(e)

(f)

Figure 5.2: Efficiency to select heavy Higgs for m_H = 300 GeV (top two), m_H = 600 GeV (middle two) and m_H = 1000 GeV (bottom two) after applying all kinematic selections in (a),(c),(e) the electron channel and (b),(d),(f) the muon channel. Both signal and di-lepton triggers are checked.

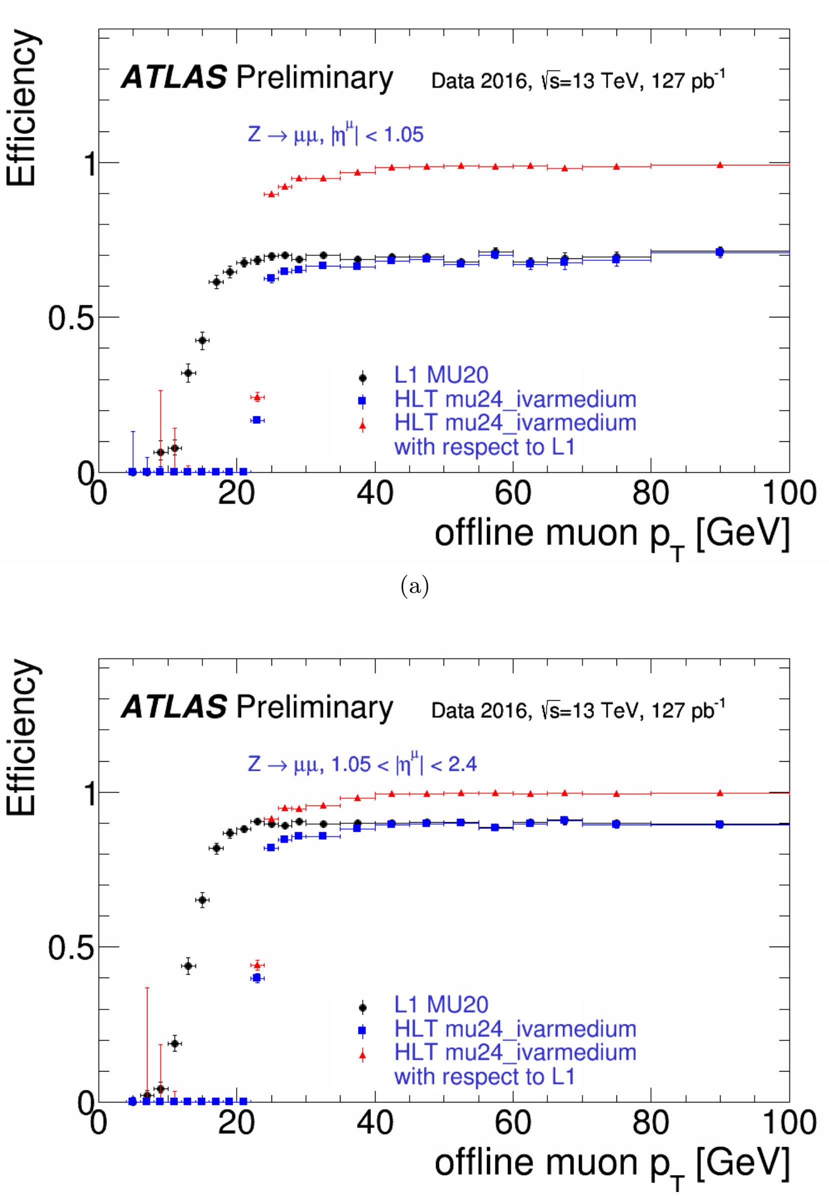

(a)

(b)

Figure 5.3: L1 muon trigger efficiency, HLT muon trigger efficiency and relative efficiency of muon trigger as a function of p_{T} of offline muon candidates in (a) the barrel detector region and (b) the endcap region[64].

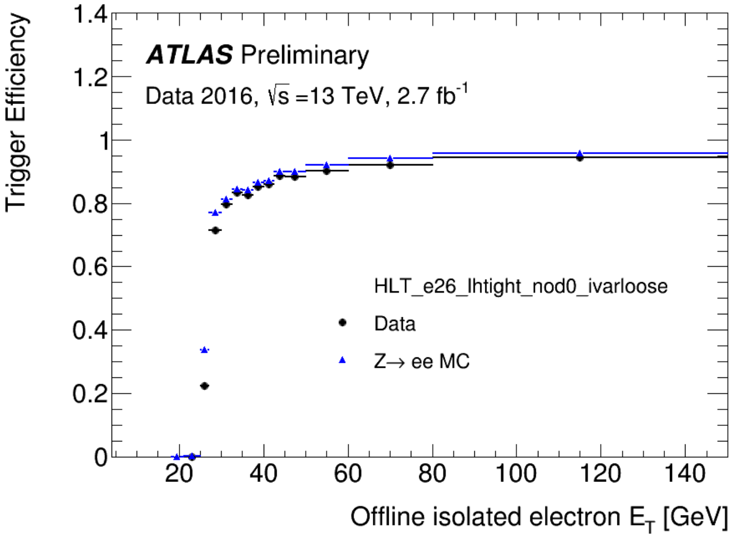

(a)

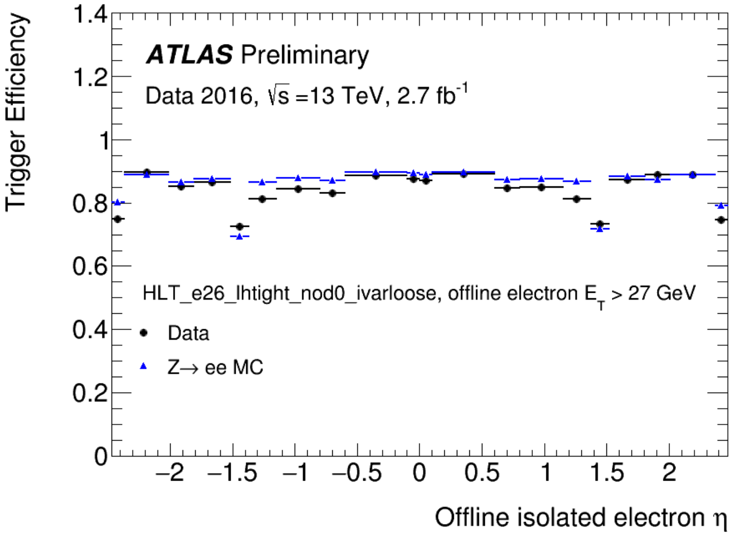

(b)

Figure 5.4: Electron trigger efficiency as a function of (a) electron p_{T} and (b) electron η[65].

invariant mass of the selected two leptons is required to be within the range of 76 GeV $\leq M_{\ell\ell} \leq$ 106 GeV. Figure 5.5 shows the invariant mass of leptons that pass the object selections. Here Only events with two oppositely signed same flavor leptons and no additional leptons are accepted.

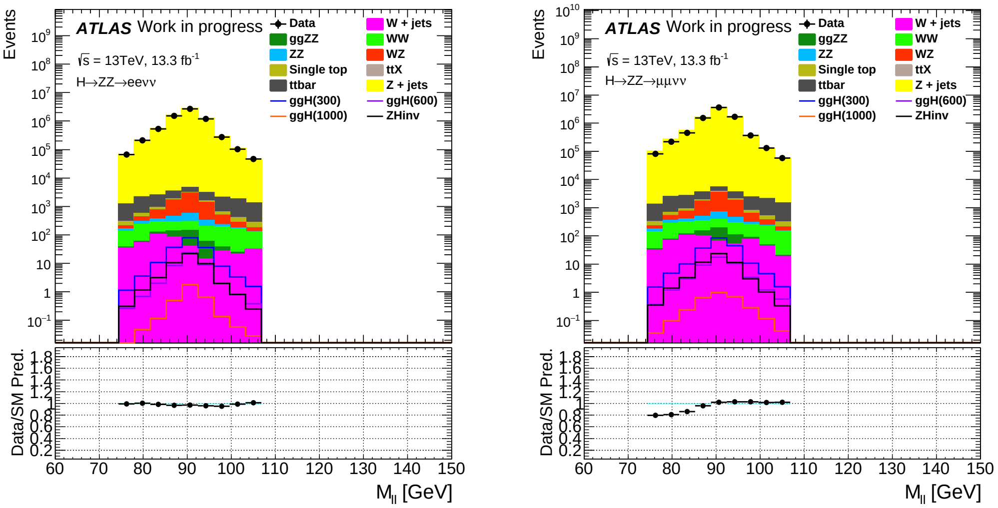

(a)

(b)

Figure 5.5: The invariant mass of leptons that pass the object selections in the (a) electron channel and (b) muon channel.

Others common selections are applied, which exploits the topology and kinematics of the signal events. A lower threshold is set on the $E_{\mathrm{T}}^{\mathrm{miss}}$ variable, which helps in selecting signal events while rejecting the inclusive Z production, since the signal productions predict the high p_{T} neutrinos caused by high $\hat{s}$. The $E_{\mathrm{T}}^{\mathrm{miss}}$ thresholds are different accordingly because $\hat{s}$ is difference between the ZZ resonance and the dark matter searches. Figure 5.6 shows the $E_{\mathrm{T}}^{\mathrm{miss}}$ distributions with events that pass the Z boson mass requirement and third-lepton veto.

The Z boson is boosted as the same way as $E_{\mathrm{T}}^{\mathrm{miss}}$ case. This effect implies the two leptons are close in the space. Thus an upper threshold on the distance $\Delta R_{\ell\ell}$ is applied. Figure 5.7 shows the $\Delta R_{\ell\ell}$ distributions with events which pass the Z mass requirement and third-lepton veto.

In the absence of initial or final state radiation, the expected signature of signal events is that of a Z boson, recoiling against the Higgs boson. Thus the $E_{\mathrm{T}}^{\mathrm{miss}}$ is expected to be balanced against the Z boson p_{T}. If some objects have large different p_{T} from the truth object (caused by the calibration, smearing, etc), the balance can not be kept. To reduce the imbalance events, the fractional p_{T} difference variables which is defined as the following

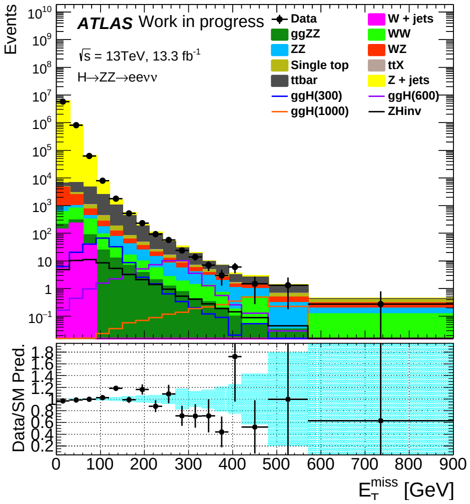

(a) (b)

Figure 5.6: The missing transverse energy distribution in the (a) electron channel and the (b) muon channel.

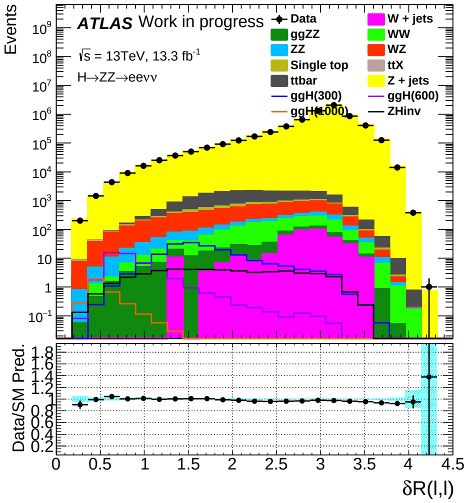

(a) (b)

Figure 5.7: The distance between leptons ($\Delta R_{\ell\ell}$) in the (a) electron channel and the (b) muon channel.

equation is used for the event selection:

$$\begin{aligned} \text{frac. } p_{\mathrm{T}} \text{ diff.} &= |p_{\mathrm{T}}^{\text{miss,jet}} - p_{\mathrm{T}}^{ll}|/p_{\mathrm{T}}^{ll}. && (5.2) \\ p_{\mathrm{T}}^{miss,jet} &= |\vec{E}_{\mathrm{T}}^{\text{miss}} + \sum_{jets} \vec{p}_{\mathrm{T}}^{jet}| && (5.3) \end{aligned}$$

The fractional p_{T} difference distributions are shown in Figure 5.8. In these plots, the Z mass requirement and third lepton veto are applied.

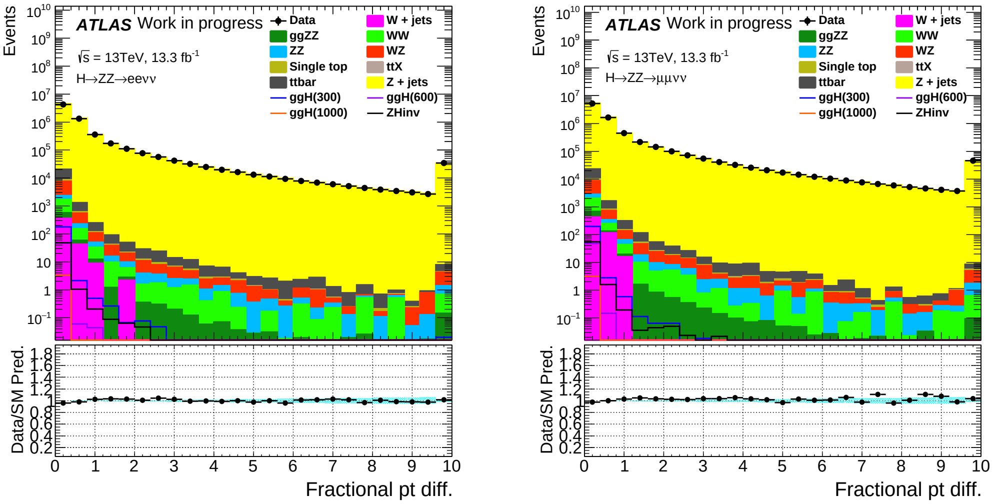

(a)

(b)

Figure 5.8: The fractional p_{T} difference distributions in the (a) electron channel and (b) muon channel.

Furthermore, $\Delta\phi(Z, E_{\mathrm{T}}^{\text{miss}})$ also has a sensitivity to separate the signal with the background since $E_{\mathrm{T}}^{\text{miss}}$ is expected to be back-to-back with respect to the Z boson in the signal. Figure 5.9 shows the $\Delta\phi(Z, E_{\mathrm{T}}^{\text{miss}})$ distributions in events with two leptons with an invariant mass consistent with Z boson.

The Z + jets background is efficiently reduced by the $E_{\mathrm{T}}^{\text{miss}}$, $\Delta R_{\ell\ell}$ selections, however it may not be removed when some objects have large difference in distribution described simulation due to smearing or calibration. These events have very similar kinematics to the signals. To reduce these background events, two additional selections, $\Delta\phi(jet, E_{\mathrm{T}}^{\text{miss}})$ and p_{T}^{Z}/m_T are applied.

High $E_{\mathrm{T}}^{\text{miss}}$ Drell-Yan events that pass the kinematic selections usually have high p_{T} jets, boosted Z boson, and large $E_{\mathrm{T}}^{\text{miss}}$ originated from mis-measurement of high p_{T} jets. Therefore, absolute value of $\Delta\phi(jet, E_{\mathrm{T}}^{\text{miss}})$ is defined as the minimum azimuthal angle separation between $E_{\mathrm{T}}^{\text{miss}}$ and jets with $p_{\mathrm{T}} > 100$ GeV for the ZZ resonance or with $p_{\mathrm{T}} > 25$ GeV for the dark

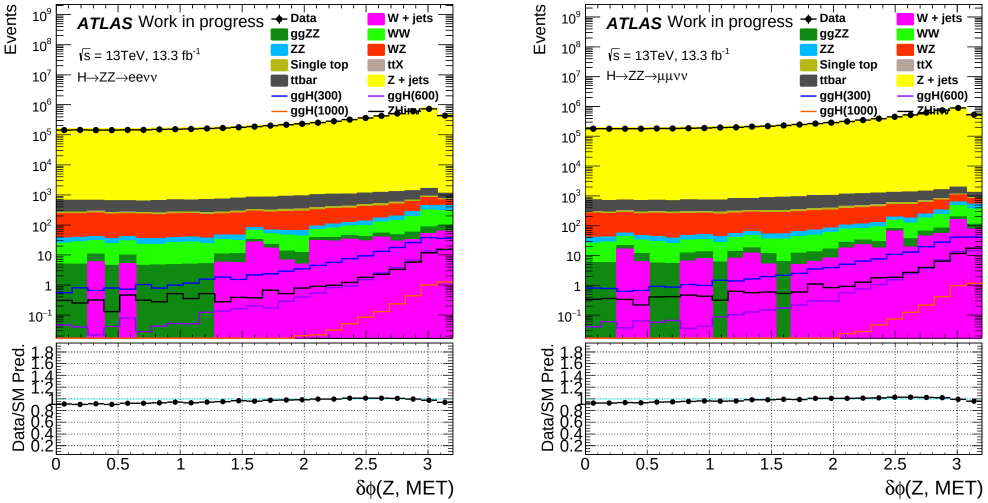

(a)

(b)

Figure 5.9: $\Delta\phi(Z, E_{\mathrm{T}}^{\mathrm{miss}})$ distributions in the (a) electron channel and (b) muon channel.

matter searches. Figure 5.10 shows the minimum $\Delta\phi(jets, E_{\mathrm{T}}^{\mathrm{miss}})$ distributions.

The p_{T}^{Z}/m_T also helps to reject events with fake $E_{\mathrm{T}}^{\mathrm{miss}}$ as well as events where the $E_{\mathrm{T}}^{\mathrm{miss}}$ is mismeasured due to the momentum resolution of high-p_{T} muons. The m_T is the transverse mass of the event which is defined as equation 5.4 for the ZZ resonance search and equation 5.5 for the dark matter search. The p_{T}^{Z}/m_T typically has around 0.5 for the signal. To reduce the events with large $E_{\mathrm{T}}^{\mathrm{miss}}$ caused by mis-reconstruction, the upper cut is applied.

$$(m_{\mathrm{T}}^{ZZ})^2 = \left(\sqrt{m_Z^2 + |p_{\mathrm{T}}^{\ell\ell}|^2} + \sqrt{m_Z^2 + |E_{\mathrm{T}}^{\mathrm{miss}}|^2}\right)^2 - |\boldsymbol{p}_{\mathbf{T}}^{\boldsymbol{\ell\ell}} - \boldsymbol{E}_{\mathbf{T}}^{\mathbf{miss}}|^2 \tag{5.4}$$

$$m_{\mathrm{T}} = \sqrt{2p_{\mathrm{T}}^{ll}E_{\mathrm{T}}^{\mathrm{miss}}(1 - \cos(\Delta\phi(\boldsymbol{p}_{\mathbf{T}}^{\boldsymbol{\ell\ell}}, \boldsymbol{E}_{\mathbf{T}}^{\mathbf{miss}})))} \tag{5.5}$$

Figure 5.11 and Figure 5.12 show p_{T}^{Z}/m_T distributions for the ZZ resonance search and the dark matter search, respectively.

Finally, events with a b-jet with $p_{\mathrm{T}} > 20$ GeV and $|\eta| < 2.5$ are rejected to reduce the top quark background. Figure 5.13 shows the number of b-tagged jets distributions.

5.4 The event selection optimization

To optimize the event selection, all the cut requirements except for one variable are applied, and the signal significance is scanned for that variable (the N-1 method). When the variable

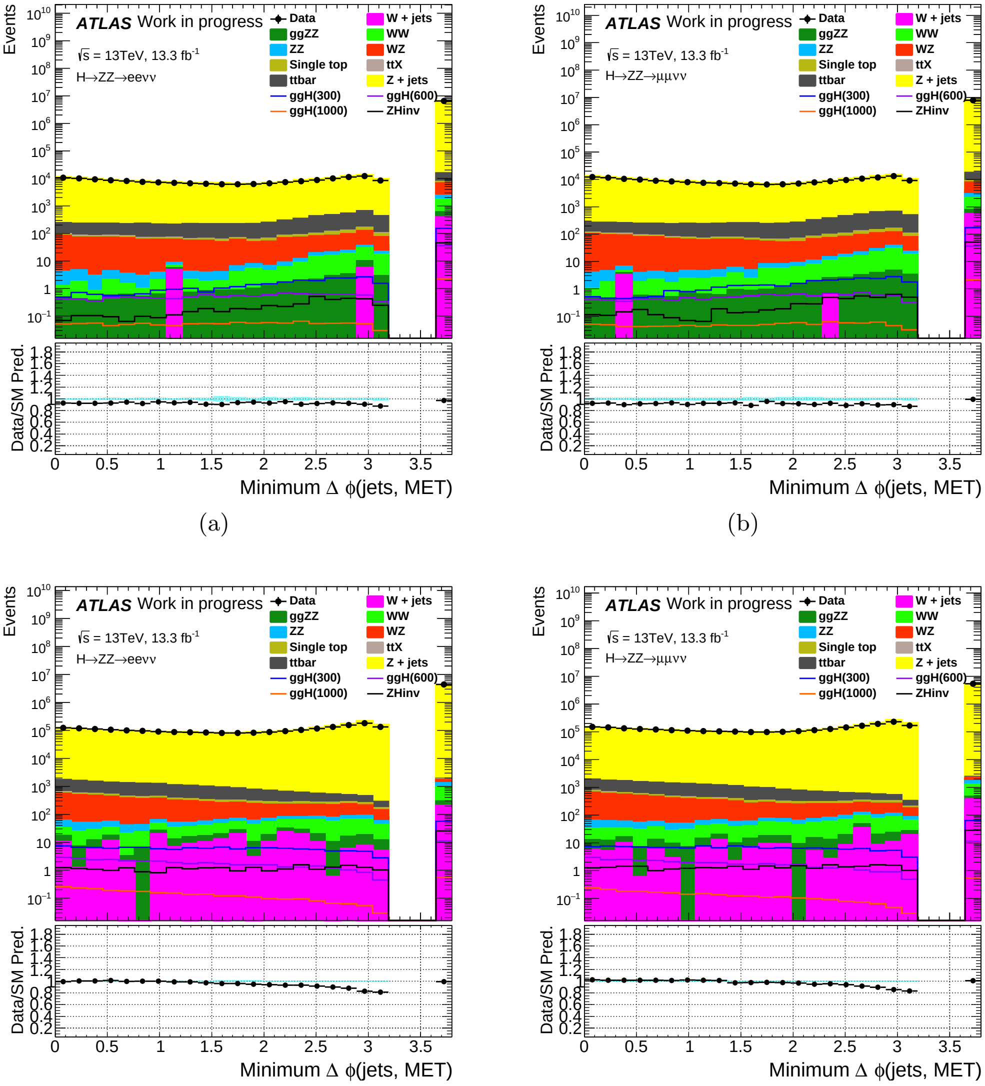

(a) (b)

(c) (d)

Figure 5.10: Minimum $\Delta\phi(jets, E_{\mathrm{T}}^{\mathrm{miss}})$ distributions with events that have jets with $p_{\mathrm{T}} > 100$ GeV (top two plots) or with $p_{\mathrm{T}} > 25$ GeV in the electron channel (left two plots) and muon channel(right two plots). The events which do not have jets are added to the overflow bin.

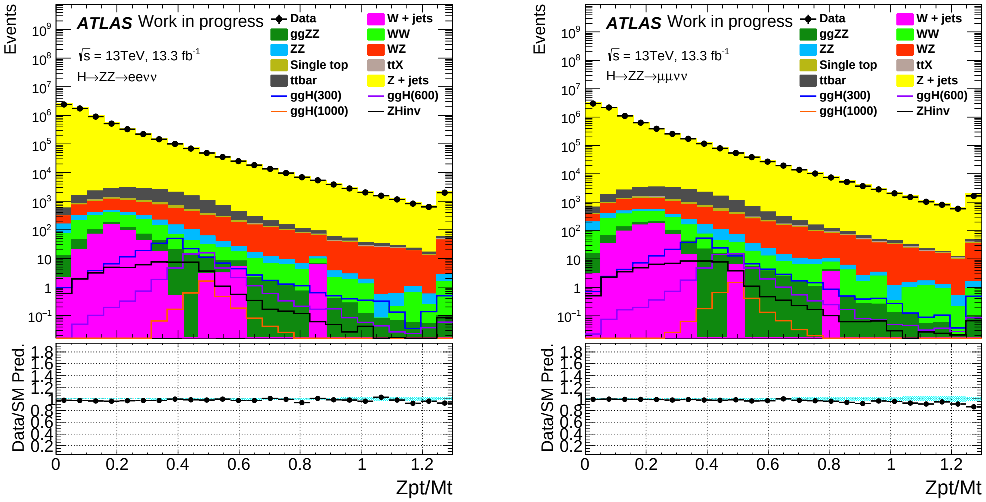

(a)

(b)

Figure 5.11: $p_{\mathrm{T}}^{Z}/m_{T}^{ZZ}$ distributions in (a)the electron channel and (b)the muon channel.

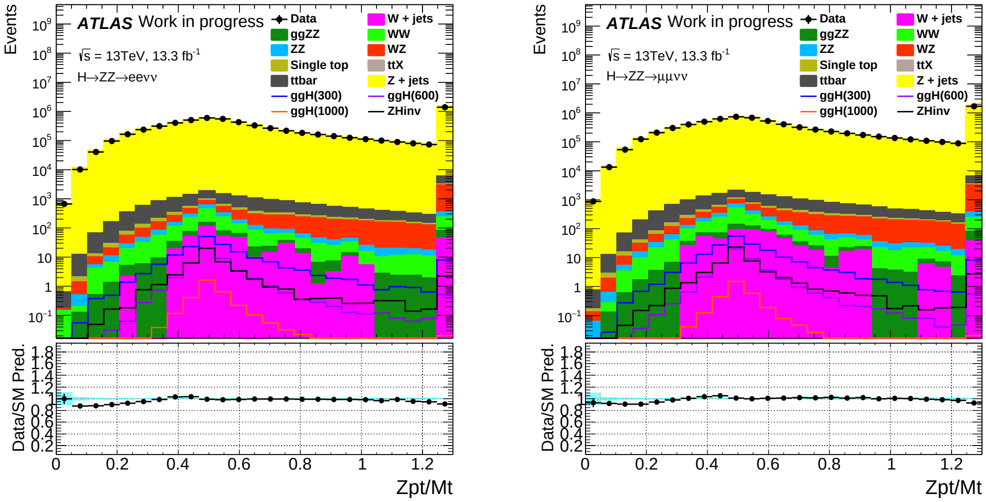

(a)

(b)

Figure 5.12: p_{T}^{Z}/m_{T} distributions in (a)the electron channel and (b)the muon channel.

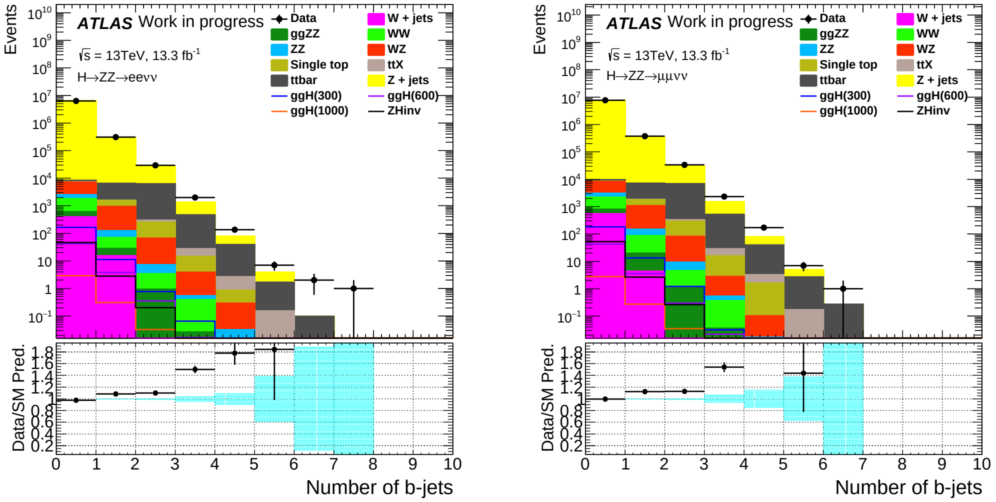

(a) (b)

Figure 5.13: Number of b-tagged jets distributions in (a)the electron channel and (b)the muon channel.

is scanned, the signal significance would be defined as the following equation :

$$Z = \sqrt{2\left(S+B\right)\ln\left(1+\frac{S}{B}\right)-S} \tag{5.6}$$

However equation 5.6 does not consider the background uncertainties. Thus the equation should be modified as equation 5.9.

$$p = A\int_0^\infty dbG(b;N_b,\delta N_b)\sum_{i=N_{data}}^{\infty}\frac{e^{-b}b^j}{i} \tag{5.7}$$

$$A = \left(\int_0^\infty dbG\left(b;N_b,\delta N_b\right)\sum_{i=0}^{\infty}\frac{e^{-b}b^i}{i}\right)^{-1} \tag{5.8}$$

$$Z = \sqrt{2}erf^{-1}(1-2p) \tag{5.9}$$

Here, the variables are defined as follows. p : the probability that background fluctuates to the measured value or above, A : a normalization factor, N_b : the number of background events, δN_b : size of the systematic uncertainty of the background, $G(b;N_b,\delta N_b)$: a Gaussian, Z : the significance.

Event selections are optimized for $m_H = 300$ GeV sample in the ZZ resonance search and for $H \to inv.$ sample in the dark matter search. When the significance is computed, the background uncertainty is assumed as 13% which is the same value adopted in the Run-1

8 TeV analysis. For example, Figure 5.14 shows the result of significance scan for the $dR_{\ell,\ell}$ distribution. For $m_H = 300$ GeV, the significance is the highest at $dR_{\ell,\ell} = 1.8$. Significance scan is done for all the other variables. Table 5.2 and table 5.3 summarize event selections for the ZZ resonance search and the dark matter search, respectively.

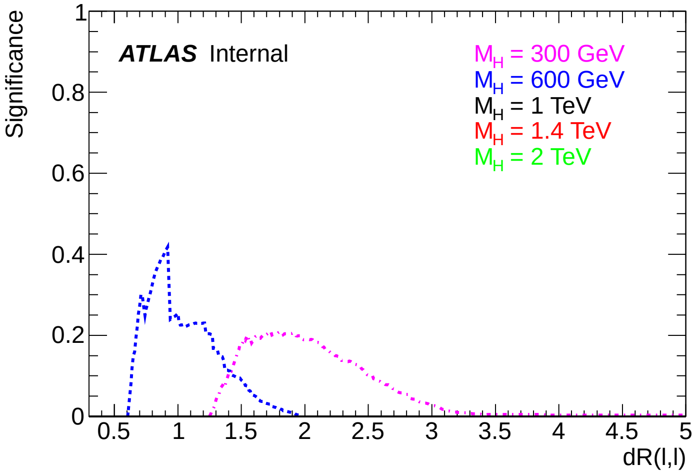

Figure 5.14: Significance scan for the dR(ℓ,ℓ) distribution with background uncertainty 13%.

Table 5.2: List of event selections for the ZZ resonance search.

Event Pre-Selection
All_Good GRL events
Vertex with ≥ 2 tracks with $p_{\mathrm{T}} > 1$ GeV
Single lepton trigger as in section 5.2
Event Selection
Two Same Flavor Opposite-Sign Leptons (e^+e^- OR $\mu^+\mu^-$)
Veto of any additional lepton with Loose PID and $p_T > 7$ GeV
$76 < M_{\ell\ell} < 106$ GeV
$E_{\mathrm{T}}^{\mathrm{miss}} > 120$ GeV
$\Delta R_{\ell\ell} < 1.8$
$\Delta\phi(Z, E_{\mathrm{T}}^{\mathrm{miss}}) > 2.7$
Fractional p_{T} difference < 0.2
$\Delta\phi(jet(p_{\mathrm{T}} > 100$ GeV$)$, $E_{\mathrm{T}}^{\mathrm{miss}}) > 0.4$
$Z_{p_{\mathrm{T}}}/m_T < 0.7$
b-jet Veto

Table 5.3: List of event selections for the Higgs invisibly decaying search.

Event Pre-Selection
All_Good GRL events
Vertex with ≥ 2 tracks with $p_{\mathrm{T}} > 1$ GeV
Single lepton trigger as in section 5.2
Event Selection
Two Same Flavor Opposite-Sign Leptons (e^+e^- OR $\mu^+\mu^-$)
Veto of any additional lepton with Loose PID and $p_T > 7$ GeV
$76 < M_{\ell\ell} <$106 GeV
$E_{\mathrm{T}}^{\mathrm{miss}} > 90$ GeV
$\Delta R_{\ell\ell} < 1.8$
$\Delta\phi(Z, E_{\mathrm{T}}^{\mathrm{miss}}) > 2.7$
Fractional p_{T} difference < 0.2
$\Delta\phi(jet(p_{\mathrm{T}} > 25GeV), E_{\mathrm{T}}^{\mathrm{miss}}) > 0.7$
$Z_{p_{\mathrm{T}}}/m_T < 0.9$
b-jet Veto

Chapter 6

Background Estimation

This part describes how to estimate the main backgrounds to the $ll + E_{\mathrm{T}}^{\mathrm{miss}}$ final states.

6.1 ZZ background

The Standard model $ZZ \to \ell\ell\nu\nu$ background has the same final states and the similar kinematics with the signals, therefore it is the main background in $Z + E_{\mathrm{T}}^{\mathrm{miss}}$ analyses. These backgrounds are estimated with Monte Carlo predictions since it is difficult to define a control region to estimate both $qq \to ZZ$ and $gg \to ZZ$ backgrounds. Both the $qq \to ZZ$ and $gg \to ZZ$ processes are considered. The NNLO QCD k-factor as a function of m_{ZZ} is applied to normalize the $qq \to ZZ$ contribution. Regarding the k-factor for $gg \to ZZ$ continuum production calculated for mass-less quark loops [66, 67] and in the heavy top quark limit [68], and for $gg(\to h*)\to ZZ$, i.e. off-shell light Standard Model Higgs signal plus its interference with the continuum background [69, 70], we estimate a k-factor of 1.7 ± 1.0 while the applied uncertainty of 60% results from conservative considerations.

For ZZ background, theoretical uncertainties are only considered as the systematic uncertainty since background is estimated with Monte-Carlo expectation. As a theoretical uncertainty, NNLO QCD correction, EW NLO correction, QCD uncertainty and PDF uncertainty are considered. The detail will be described in Section 7.1.

The data-driven estimation is also investigated for ZZ background. However the statistics is not enough to adopt the method at this point. The detail of data-driven study is described in appendix B.

6.2 WZ background

This background in which the lepton from W boson decay is not reconstructed is the second largest background in $Z + E_{\mathrm{T}}^{\mathrm{miss}}$ analyses. In order to normalize $WZ \to \ell\nu\ell\ell$ prediction to the data, we define a three-lepton control region (3l-CR), where additional lepton is required to the two leptons from Z boson decay in events which have no b-tagged jets. The third lepton is defined in the same way as the two leptons from the Z boson, which is described in Section 3.2 and Section 3.1. Figure 6.1 and Figure 6.2 show $E_{\mathrm{T}}^{\mathrm{miss}}$ distributions and transverse mass distributions of third lepton and $E_{\mathrm{T}}^{\mathrm{miss}}$ system, respectively.

As it can be seen from figures, many Z + jets contributions still exist. For higher purity of WZ in 3l-CR, the transverse mass of third lepton and $E_{\mathrm{T}}^{\mathrm{miss}}$ system is required to be higher than 60 GeV. In addition, events including a b-tagged jet are vetoed. Final selection criteria is shown in table 6.1, and the plots for the events in 3l-CR are also shown in Figure 6.3. Events with a transverse mass greater than 60 GeV are dominated by WZ production. The purity of the region turns out to be ~90%. The final scale factor to normalize WZ contribution is then obtained by averaging the single scale factors in the different decay modes : a scale factor of 1.25 ± 0.04 (stat) $\pm$ 0.05 (syst) is evaluated. The systematic uncertainty is estimated to 0.05 by taking the largest difference found among the average and each of the four SFs. Shape systematics uncertainties on WZ background will be mentioned in Section 7.1.

Table 6.1: List of selections applied at the event selection level for three lepton control region.

Event Pre-Selection
All_Good GRL events
Vertex with ≥ 2 tracks with $p_{\mathrm{T}} > 1$ GeV
Single lepton trigger as in section 5.2
Event Selection
Two Same Flavor Opposite-Sign Leptons (e^+e^- OR $\mu^+\mu^-$) and one additional lepton
Veto of any additional lepton with Loose PID and $p_T > 7$ GeV
$76 < M_{\ell\ell} < 106$ GeV (If two combination pass the cut, a pair closer to Z mass is chosen)
M_T ($E_{\mathrm{T}}^{\mathrm{miss}}$, 3rd lepton) > 60 GeV
b-jet Veto

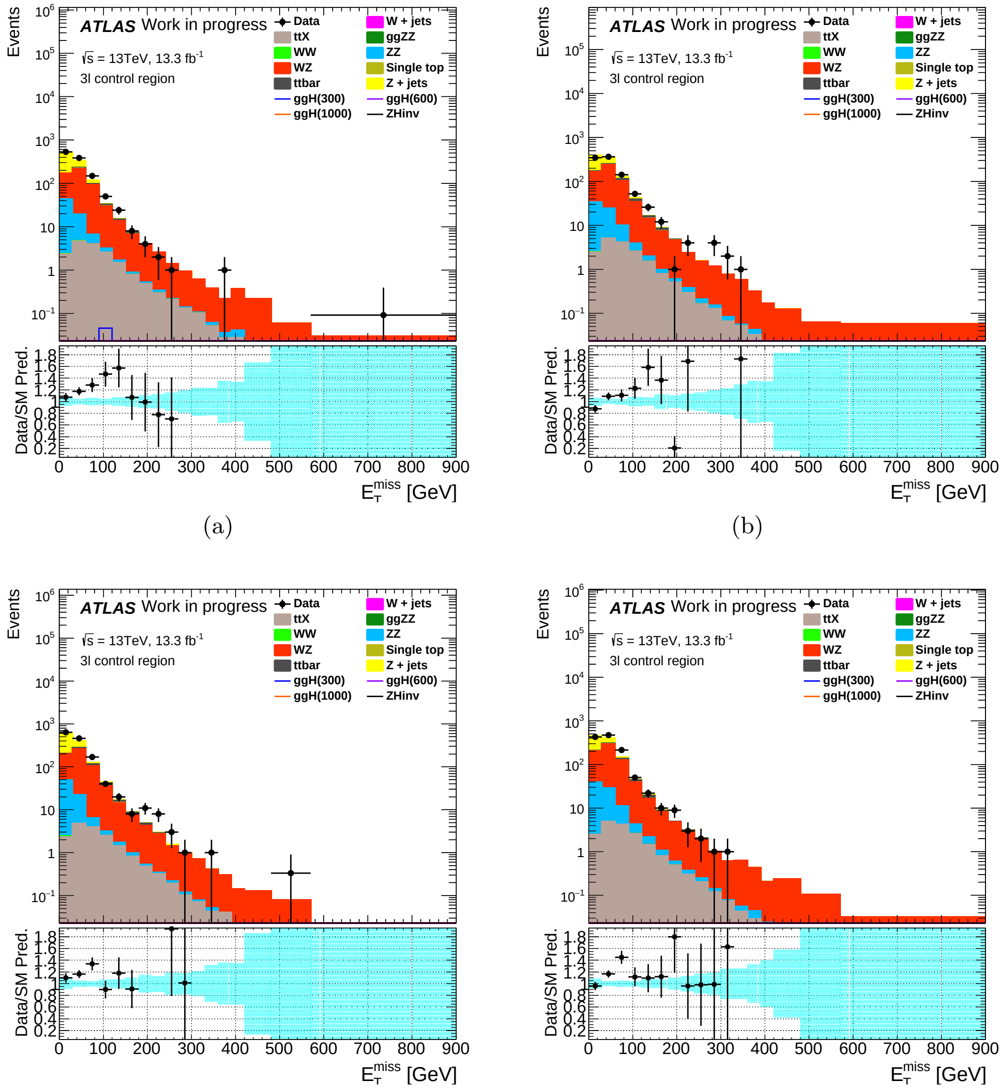

(a) (b)

(c) (d)

Figure 6.1: $E_{\mathrm{T}}^{\mathrm{miss}}$ distributions for data and Monte-Carlo in $ee + e$ channel (top left) , $ee + \mu$ channel (top right), $\mu\mu + e$ channel (bottom left) and $\mu\mu + \mu$ channel (bottom right) in events with one additional lepton with respect to the lepton pair whose invariant mass is consistent with Z boson mass. The bottom plots show the ratio of the data and Monte Carlo.

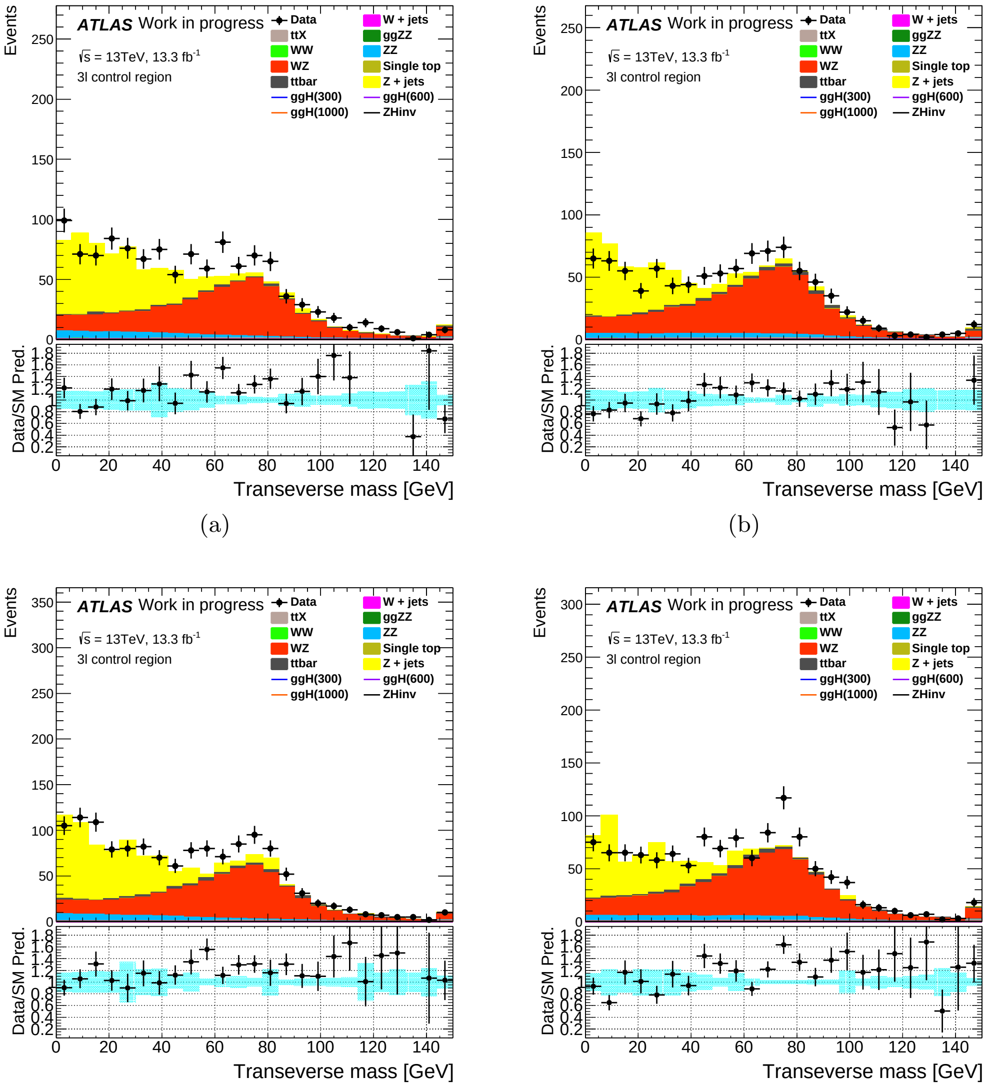

(a) (b) (c) (d)

Figure 6.2: Transverse mass distributions for data and Monte-Carlo in $ee + e$ channel (top left) , $ee + \mu$ channel (top right), $\mu\mu + e$ channel (bottom left) and $\mu\mu + \mu$ channel (bottom right) in events with one additional lepton with respect to the lepton pair whose invariant mass is consistent with Z boson mass. The bottom plots show the ratio of the data and Monte Carlo.

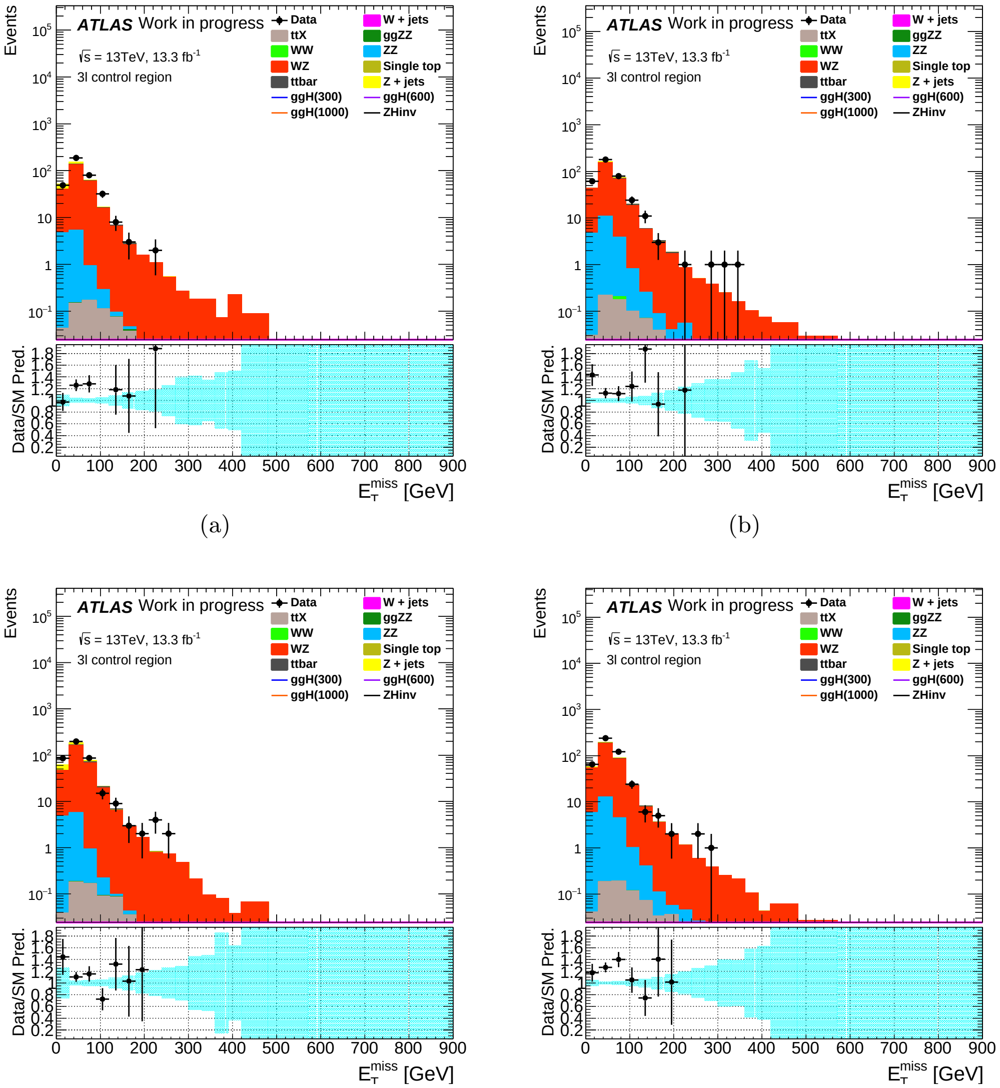

(a)

(b)

(c)

(d)

Figure 6.3: Transverse mass distributions for data and Monte-Carlo in ee + e channel (top left) , ee + μ channel (top right), $\mu\mu$ + e channel (bottom left) and $\mu\mu$ + μ channel (bottom right) in events with one additional lepton with respect to the lepton pair whose invariant mass is consistent with Z boson mass. The bottom plots show the ratio of the data and Monte Carlo.

Table 6.2: The expected number of background and observed number of events in the 3l-CRs in $M_T > 60$ GeV region. Number of observed events is for an integrated luminosity of 13.3 fb^{-1}. The quoted uncertainty is statistical.

channel	$ee+e$	$ee+\mu$	$\mu\mu+e$	$\mu\mu+\mu$	Total
Expected	209.93 ± 5.40	305.05 ± 4.23	348.16 ± 12.30	369.36 ± 18.44	1313.51 ± 14.60
Observed	361	362	406	465	1594
Scale factor	1.28 ± 0.08	1.21 ± 0.07	1.20 ± 0.08	1.29 ± 0.07	1.25 ± 0.04 ± 0.05

Figure 6.4 shows the invariant mass of the WZ resonance system for data and Monte-Carlo. In all the ratio plots, the difference between data and Monte-Carlo is flat. This behavior means that the scale factor do not depend on the m_{WZ}. Since the systematic uncertainties on the m_T shape are computed as function of M_{WZ}, the systematic uncertainty related to the difference between signal and control regions should not be considered.

6.3 Top, WW, Wt, $Z \to \tau\tau$ background

$t\bar{t}$, WW, single top and $Z \to \tau\tau$ have a minor contribution on $\ell\ell + E_{\mathrm{T}}^{\mathrm{miss}}$ analyses. Most of backgrounds in association with a top quark can be reduced with b-tagged jet veto. $WW \to \ell\nu\ell\nu$ is mainly removed by requiring that the two leptons have an invariant mass consistent to be Z boson mass. Remaining WW process can be reduced by $E_{\mathrm{T}}^{\mathrm{miss}}$ requirement. $Z \to \tau\tau$ decaying to two light leptons can be the background, however their invariant mass should be lower than $Z \to ee/\mu\mu$ since neutrinos take away the energy.

The contribution of $t\bar{t}$, WW, single top and $Z \to \tau\tau$ is estimated from the data using a dedicated control region. All the backgrounds decay to $e\mu$ pair in addition to ee and $\mu\mu$. The probability of $e\mu$ process has a probability twice the other two decay modes due to flavor symmetry. Thus, we define $e\mu$ control region to estimate the backgrounds. Table 6.3 shows the definition of $e\mu$ control region.

Figure 6.5 - Figure 6.7 show the distributions of the various variables in the $e\mu$ control region. These are distributions after di-lepton invariant mass selection. The data points are drawn on top of MC samples and the Data/MC ratio is given on the bottom of the plots. As can be seen the data is in good agreement with the MC expectation within the uncertainty.

Since the reconstructions efficiency are different for electrons and muons, the correction factor $\epsilon - factor$ should be applied when the $e\mu$ control region distribution is applied as the background in the signal region. $\epsilon - factor$ is defined as

$$\epsilon^2 = \frac{N_{ee}}{N_{\mu\mu}}, \tag{6.1}$$

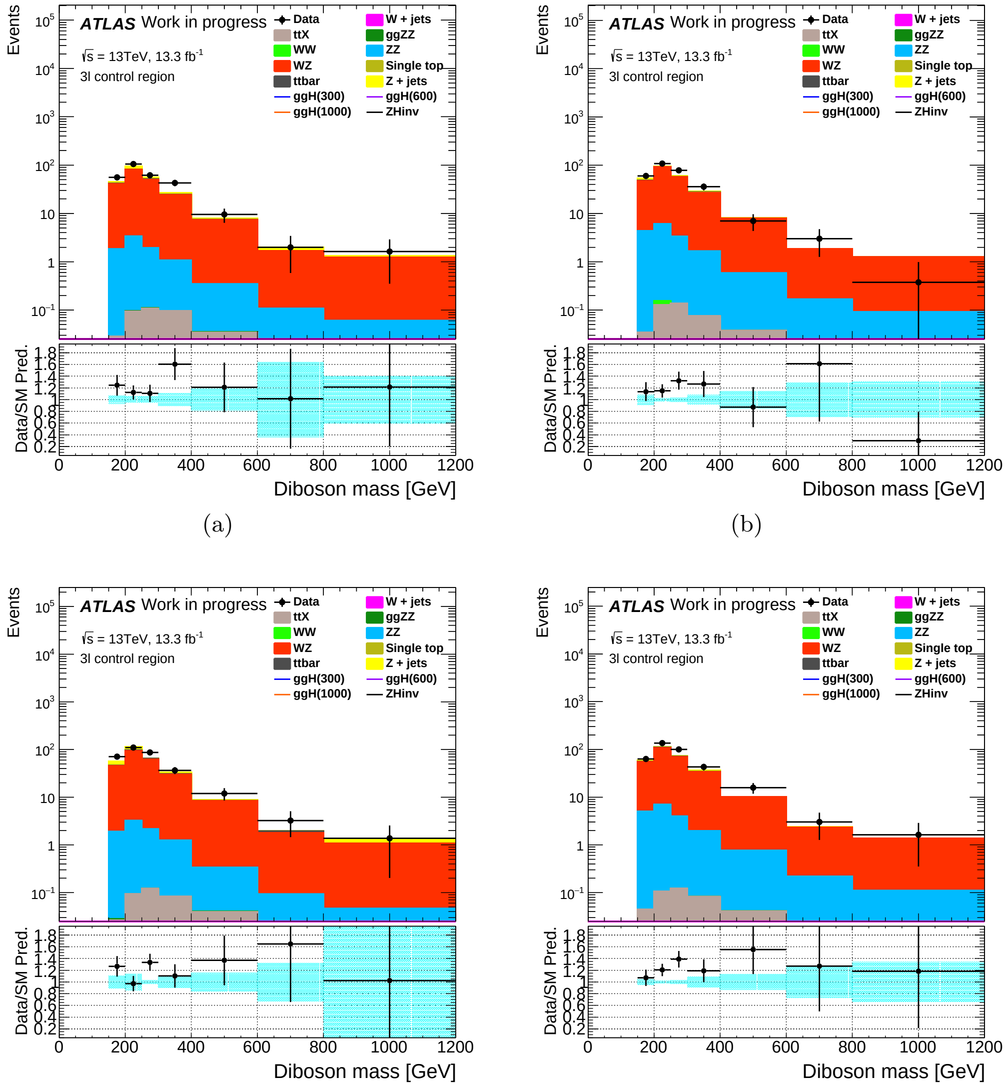

(a)

(b)

(c)

(d)

Figure 6.4: The invariant mass of the WZ resonance distributions for data and Monte-Carlo in $ee + e$ channel (top left) , $ee + \mu$ channel (top right), $\mu\mu + e$ channel (bottom left) and $\mu\mu + \mu$ channel (bottom right) in events with one additional lepton with respect to the lepton pair whose invariant mass is consistent with Z boson mass. The distributions are shown for the range of diboson mass greater than 60 GeV. The bottom plots show the ratio of the data and Monte Carlo.

Table 6.3: List of selections applied at the event selection level for $e\mu$ control region.

<table>
<tr><th colspan="2">Event Pre-Selection</th></tr>
<tr><td colspan="2">All_Good GRL events</td></tr>
<tr><td colspan="2">Vertex with ≥ 2 tracks with $p_{\mathrm{T}} > 1$ GeV</td></tr>
<tr><td colspan="2">Single lepton trigger as in section 5.2</td></tr>
<tr><th colspan="2">Event Selection</th></tr>
<tr><td>High-mass selection criteria</td><td>Low-mass selection criteria</td></tr>
<tr><td colspan="2">Two Opposite Flavor Opposite-Sign Leptons ($e^+\mu^-$ OR $e^-\mu^+$)</td></tr>
<tr><td colspan="2">Veto of any additional lepton with Loose PID and $p_T > 7$ GeV</td></tr>
<tr><td colspan="2">$76 < M_{\ell\ell} < 106$ GeV</td></tr>
<tr><td>$E_{\mathrm{T}}^{\mathrm{miss}} > 120$ GeV</td><td>$E_{\mathrm{T}}^{\mathrm{miss}} > 90$ GeV</td></tr>
<tr><td colspan="2">Δ R (e, μ) < 1.8</td></tr>
<tr><td colspan="2">$\Delta\phi$ (Z, $E_{\mathrm{T}}^{\mathrm{miss}}$) > 2.7</td></tr>
<tr><td colspan="2">Fractional pt difference < 0.2</td></tr>
<tr><td>Min. $\Delta\phi$ (jets (100 GeV), $E_{\mathrm{T}}^{\mathrm{miss}}$) > 0.4</td><td>Min. $\Delta\phi$ (jets (25 GeV), $E_{\mathrm{T}}^{\mathrm{miss}}$) > 0.7</td></tr>
<tr><td>Z_{P_T} / $M_{T_{ZZ}} < 0.7$</td><td>Z_{P_T} / $M_T < 0.9$</td></tr>
<tr><td colspan="2">b-jet Veto</td></tr>
</table>

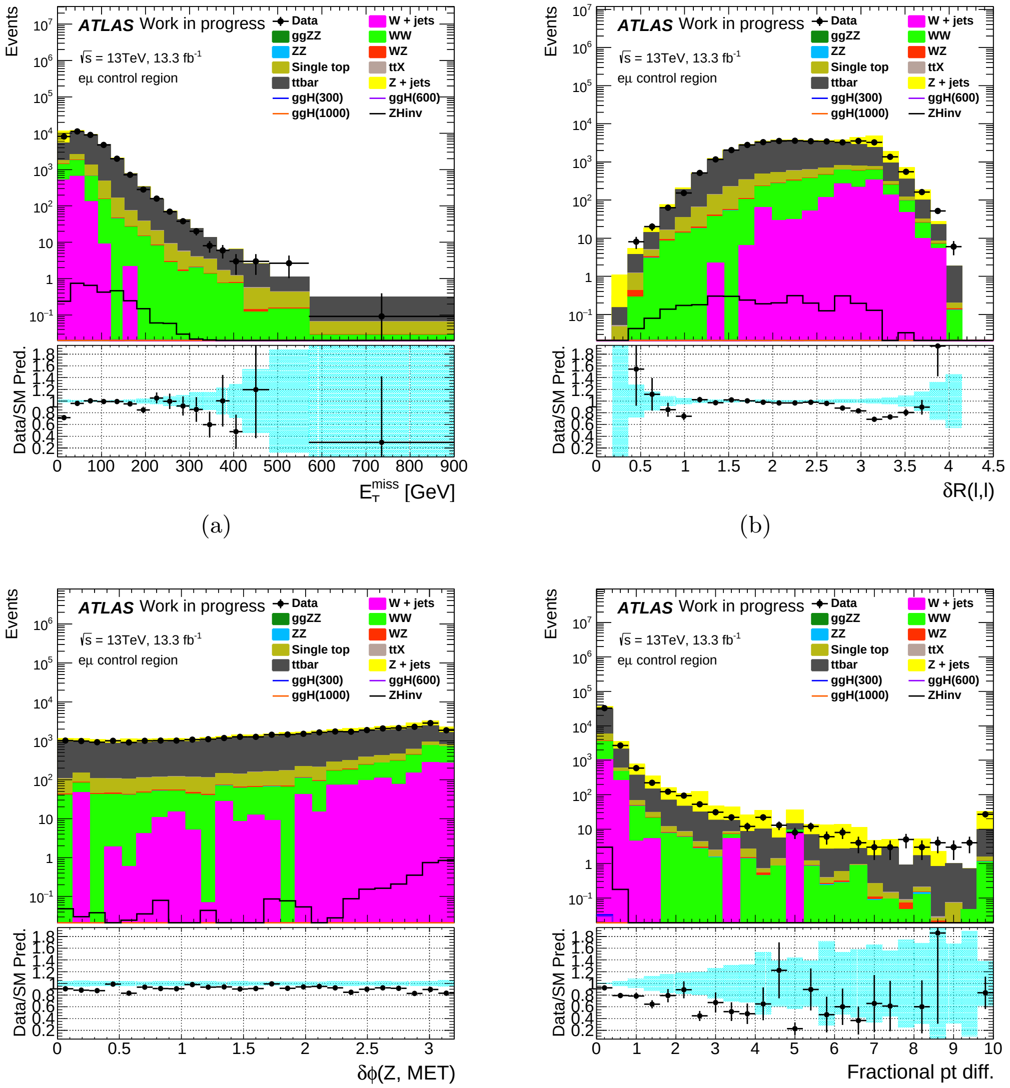

(a) (b) (c) (d)

Figure 6.5: Kinematic distributions that are used for event selections in the $e\mu$ control region, data and MC expectation after Z mass window cut applied : (a) $E_{\mathrm{T}}^{\mathrm{miss}}$, (b) distance between electron and muon, (c) the opening angle between Z and $E_{\mathrm{T}}^{\mathrm{miss}}$, (d) fractional P_T difference.

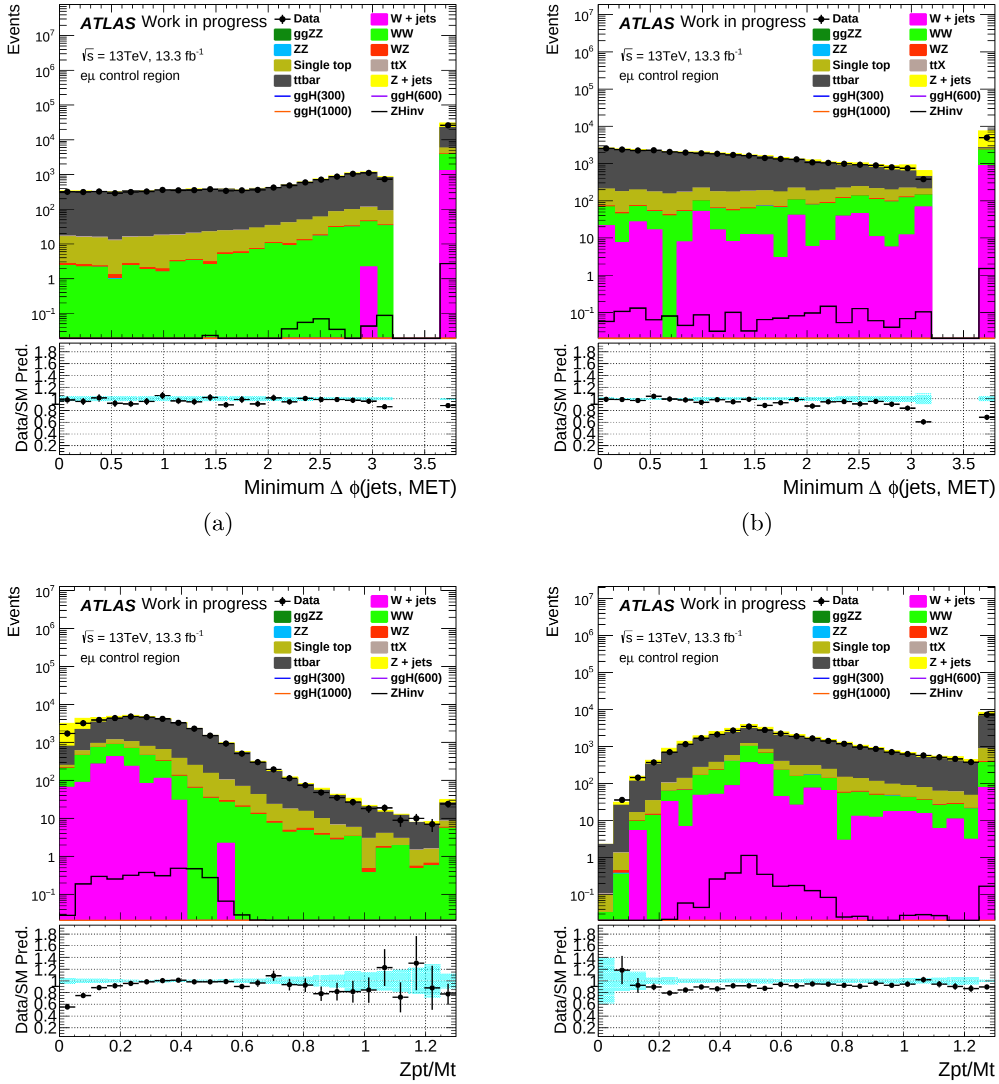

(a) (b)

(c) (d)

Figure 6.6: Kinematic distributions that are used for event selections in the $e\mu$ control region, data and MC expectation after Z mass window cut applied : (a) minimum opening angle between $E_{\mathrm{T}}^{\mathrm{miss}}$ and jet with $p_{\mathrm{T}} > 100$ GeV, (b) minimum opening angle between $E_{\mathrm{T}}^{\mathrm{miss}}$ and jet with $p_{\mathrm{T}} > 25$ GeV, (c) $Z_{P_T}/M_{T_{ZZ}}$, (d) Z_{P_T}/M_T.

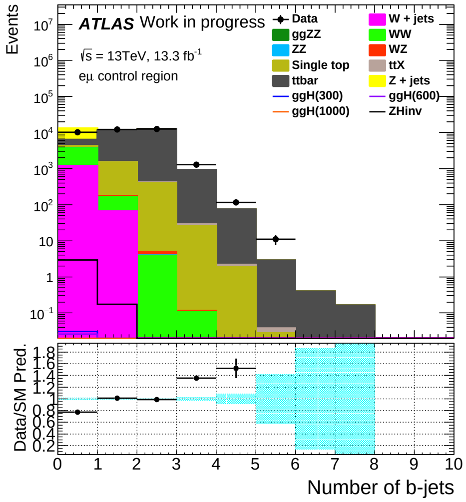

Figure 6.7: Number of b-tagged jets distribution in the $e\mu$ control region, data and MC expectation after Z mass window cut applied.

where N_{ee} and $N_{\mu\mu}$ are, respectively, ee and $\mu\mu$ events with an invariant mass compatible with Z-boson mass. Then the number of non-resonant background in the signal region is given in the following :

$$N^{e\mu}_{\mathrm{SR}ee} = \frac{1}{2} \times \epsilon \times N^{\mathrm{data,sub}}_{e\mu} \tag{6.2}$$

$$N^{e\mu}_{\mathrm{SR}\mu\mu} = \frac{1}{2} \times \frac{1}{\epsilon} \times N^{\mathrm{data,sub}}_{e\mu}. \tag{6.3}$$

$$\tag{6.4}$$

Where $N^{\mathrm{data,sub}}_{e\mu}$ is the number of $e\mu$ events in the control region subtracted with non-tt, WW, Wt and $Z \rightarrow \tau\tau$ backgrounds, estimated as :

$$N^{\mathrm{data,sub}}_{e\mu} = N^{\mathrm{data}}_{e\mu} - \sum^{i}_{\mathrm{non}-e\mu\mathrm{bkg.}} N^{\mathrm{MC}}_{i} \tag{6.5}$$

A final comparison between data and MC estimation is provided in Table 6.4 for both analyses. The systematic uncertainties are estimated from the $\epsilon - factor$ difference between data and MC expectation. The shape is taken from the MC expectation since the data statistics is not enough at this point.

Table 6.4: The estimated background yields of data (MC) in the ZZ resonance and dark matter analyses signal regions for $WW/Wt/ttbar/Z\tau\tau$ backgrounds.

	channel	Background yields from $e\mu$ estimation
Lowmass analysis	ee	16.9±2.8±1.0 (14.8±1.0)
	$\mu\mu$	20.7±3.4±1.2 (16.2±1.1)
Highmass analysis	ee	3.5±1.3±0.21 (5.55±0.66)
	$\mu\mu$	4.2±1.6±0.25 (6.10±0.72)

6.4 Z+jets background

Z+jets background is mainly reduced by $E_{\mathrm{T}}^{\mathrm{miss}}$ cut, $\Delta R(\ell,\ell)$ cut and $\Delta\phi$ (Z, $E_{\mathrm{T}}^{\mathrm{miss}}$) cut. This background has significant uncertainties in the modeling of $E_{\mathrm{T}}^{\mathrm{miss}}$ due to modeling of the detector, pileup interaction and mis-measurement of jets and leptons. Therefore it is crucial to estimate the Z+jets background with data. A so-called ABCD method is used to estimate Z+jets background.

The ABCD method is a data-driven method technique that is used to estimate the background in signal region using the numbers of events in side-band regions. The side-band regions are defined two dimensionally using the event selections of fractional p_{T} difference and $\Delta\phi(Z, E_{\mathrm{T}}^{\mathrm{miss}})$. Figure 6.8 shows the definition of signal and side-band regions. These two variables are chosen due to their non-correlation, as can be seen in Figure 6.9. Furthermore, both variables have no correction with the final discriminant variables ($E_{\mathrm{T}}^{\mathrm{miss}}$ and $M_{T_{ZZ}}$).

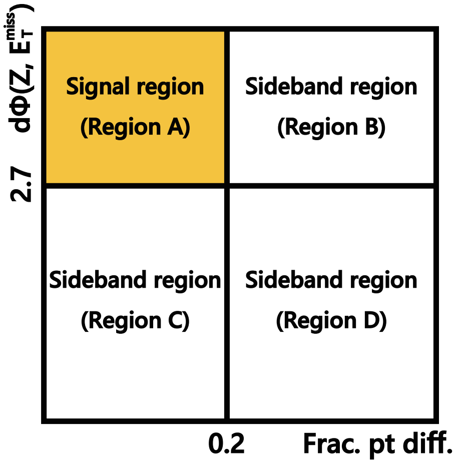

Figure 6.8: The signal and side-band regions in the ABCD method.

Figure 6.12-6.11 show the transverse mass distribution and $E_{\mathrm{T}}^{\mathrm{miss}}$ distribution for all the

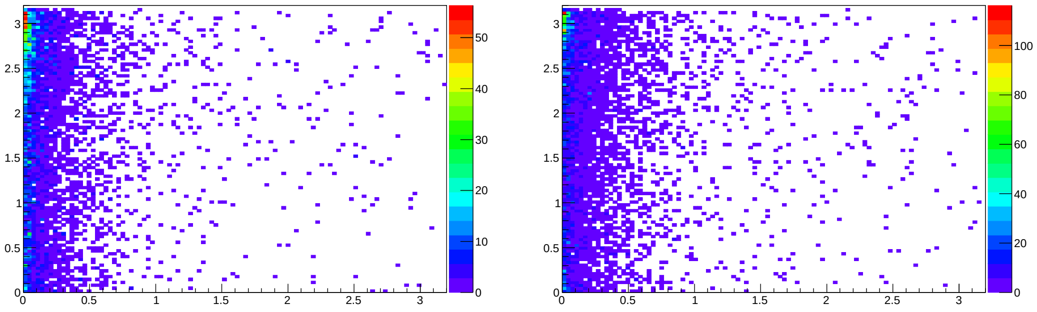

(a) (b)

Figure 6.9: Two dimensional plots for $\Delta\phi(Z, E_{\mathrm{T}}^{\mathrm{miss}})$ and fractional p_{T} difference for the electron (a) and muon (b) channels. The Z mass requirement and $E_{\mathrm{T}}^{\mathrm{miss}} > 90$ GeV requirement are applied. Horizontal : fractional p_{T} difference, Vertical : $\Delta\phi(Z, E_{\mathrm{T}}^{\mathrm{miss}})$.

regions. As can be seen in the figures, the data is in good agreement with MC expectation after Z mass window selection and Z+jets can be enriched in the side-band regions.

The Z+jets background in the signal region is estimated by the following equation :

$$N_{\mathrm{SR}} = N_{\mathrm{C}}^{\mathrm{obs,sub}} \times \frac{N_{\mathrm{B}}^{\mathrm{obs,sub}}}{N_{\mathrm{D}}^{\mathrm{obs,sub}}}, \tag{6.6}$$

where $N_{\mathrm{C}}^{\mathrm{obs,sub}}$, $N_{\mathrm{B}}^{\mathrm{obs,sub}}$ and $N_{\mathrm{D}}^{\mathrm{obs,sub}}$ are the observed events with the non-Z+jets contribution subtracted in region B, C and D, respectively.

Table 6.5 - 6.8 show the breakdown of the scaling factors against the selections for ZZ resonance and dark matter analyses. The ratios are consistent between $N_{\mathrm{A}}/N_{\mathrm{C}}$ and $N_{\mathrm{B}}/N_{\mathrm{D}}$ for both the electron and muon channels. Furthermore MC expectation of $N_{\mathrm{B}}/N_{\mathrm{D}}$ is in good agreement with data.

Table 6.9 shows the final yields of the Z+jets background estimated using the ABCD method. The final yields include statistical and systematic uncertainties. The systematic uncertainties are mainly caused by the $N_{\mathrm{B}}/N_{\mathrm{D}}$ difference against various kinematic cuts.

6.5 Fake-lepton background

W+jets, semileptonic tt and single top (s- and t-channels) backgrounds can contribute to the signal region by a mis-identifying jet as a lepton in events W boson decays leptonically. The contribution is very small since lepton mis-identification from jet, or fake-lepton, is a rare process. The lepton mis-identification is not accurately described in the simulation due to rare fragmentation processes or interactions with the detector. Thus these backgrounds

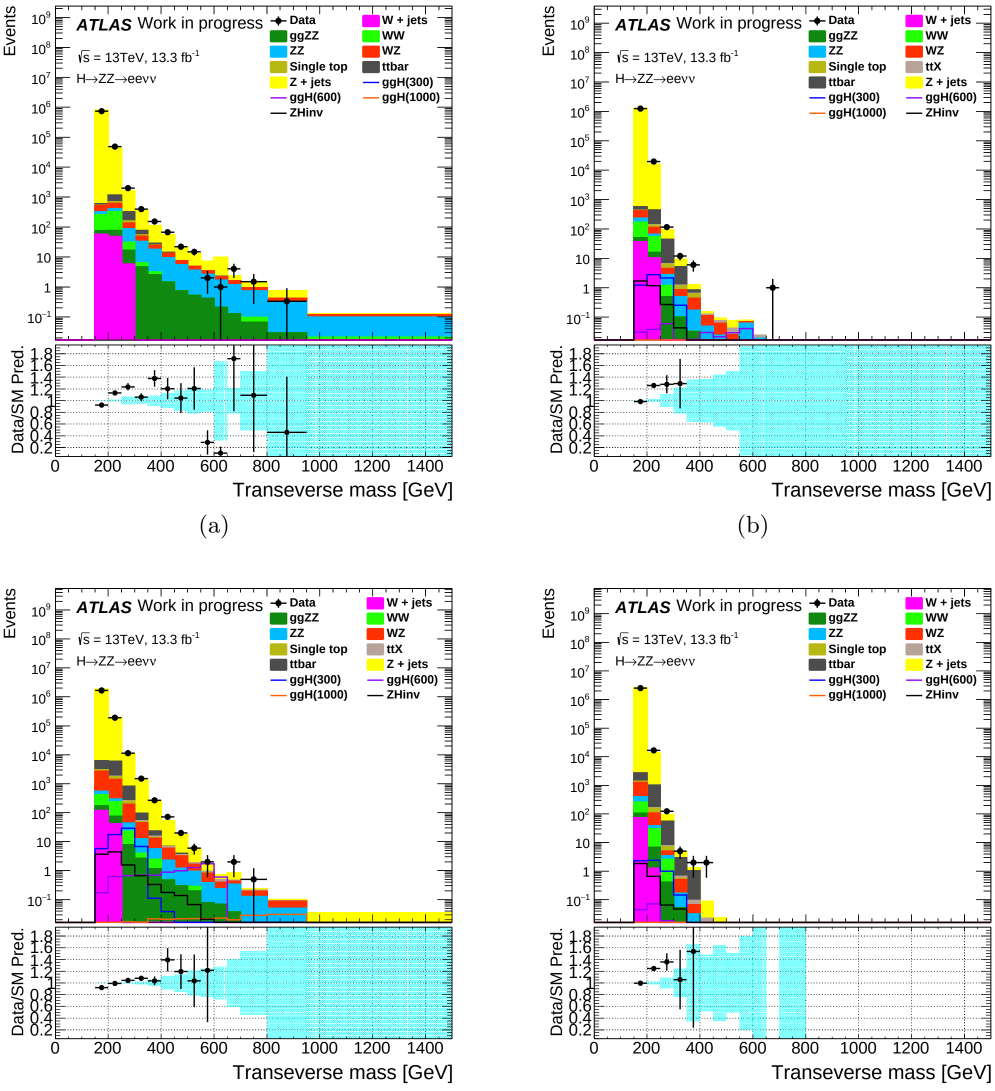

(a) (b)

(c) (d)

Figure 6.10: Transverse mass distributions in signal and side-band regions, (a) Region A, (b) Region B, (c) Region C and (d) Region D, in electron channel. Z mass window cut is applied.

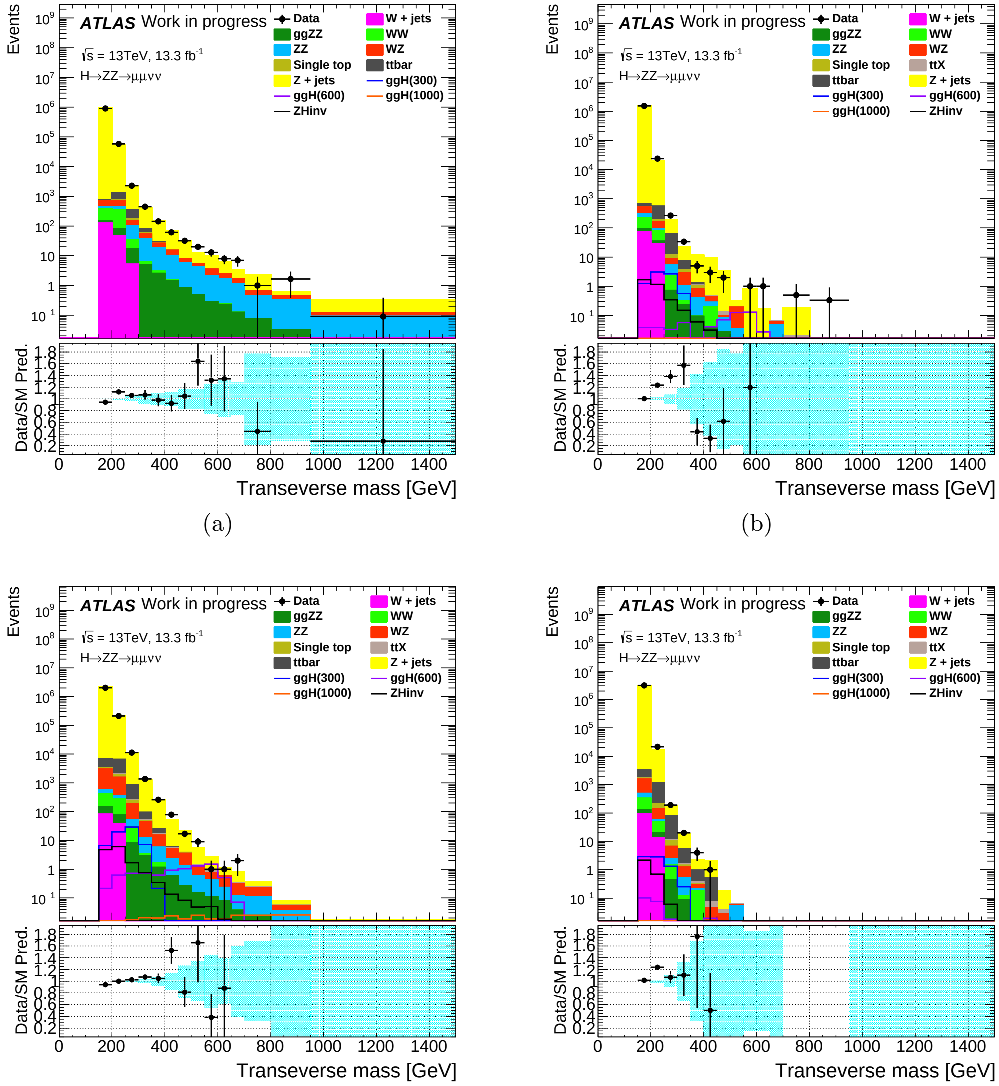

(a) (b) (c) (d)

Figure 6.11: Transverse mass distributions in signal and side-band regions, (a) Region A, (b) Region B, (c) Region C and (d) Region D, in muon channel. Z mass window cut is applied.

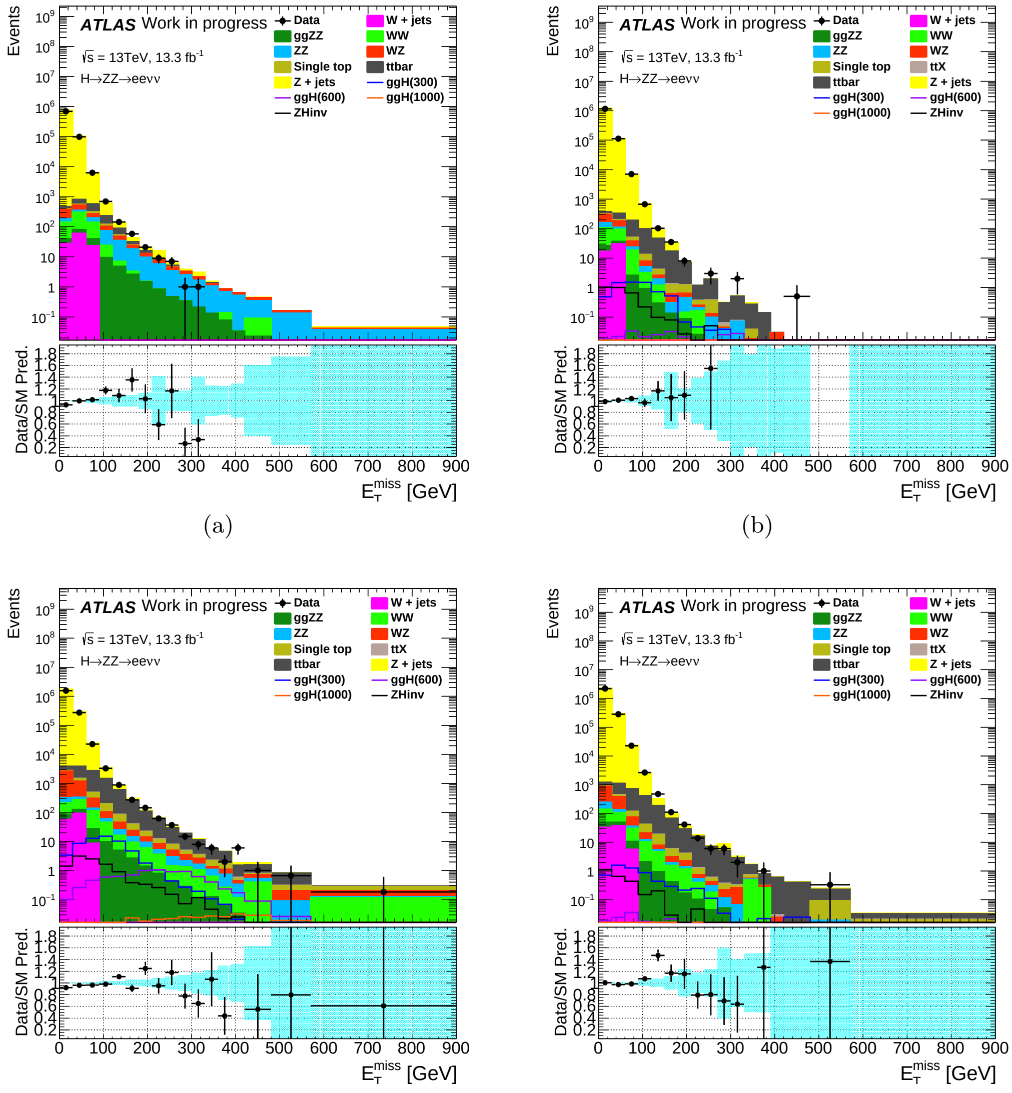

(a) (b)

(c) (d)

Figure 6.12: $E_{\mathrm{T}}^{\mathrm{miss}}$ distributions in signal and side-band regions, (a) Region A, (b) Region B, (c) Region C and (d) Region D, in electron channel. Z mass window cut is applied.

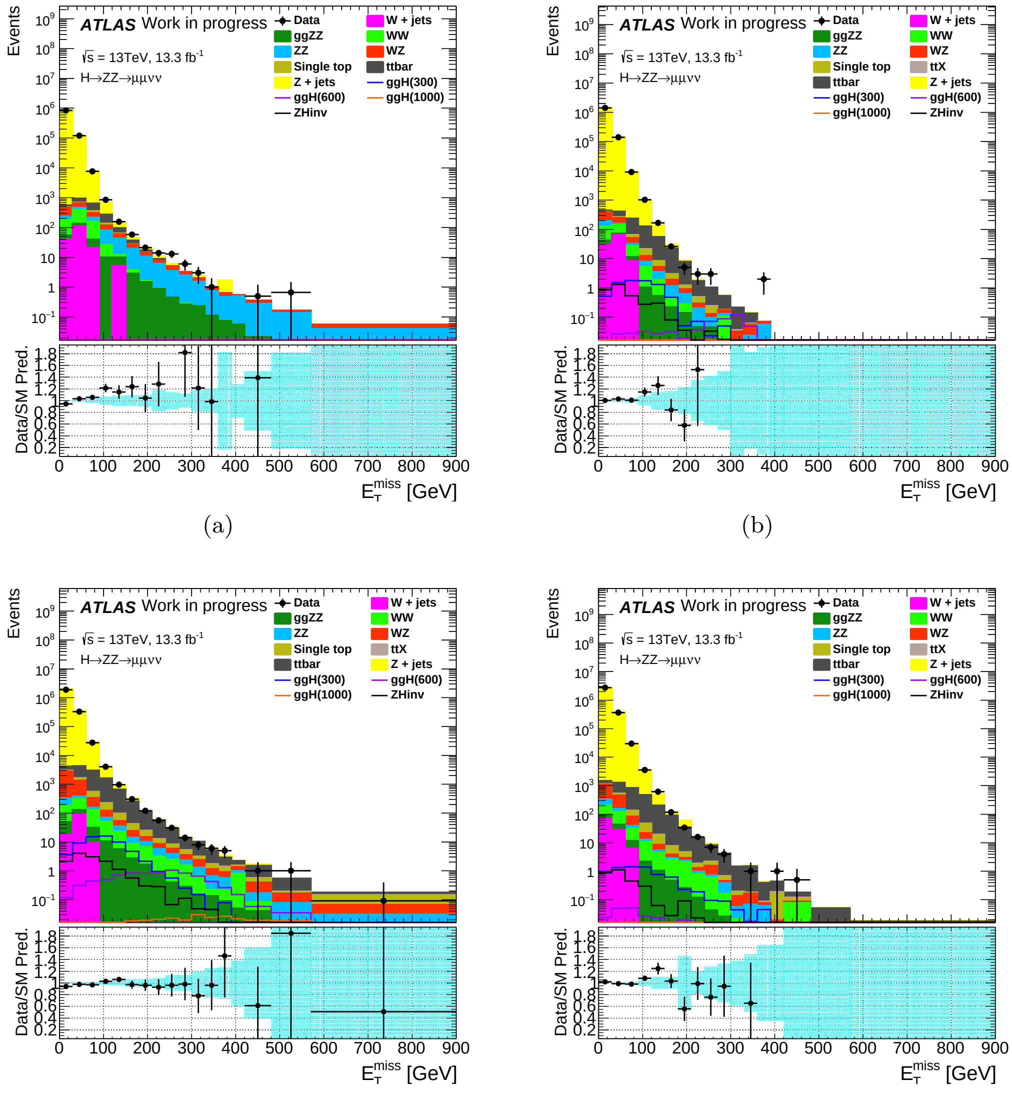

(a)

(b)

(c)

(d)

Figure 6.13: $E_{\mathrm{T}}^{\mathrm{miss}}$ distributions in signal and side-band regions, (a) Region A, (b) Region B, (c) Region C and (d) Region D, in muon channel. Z mass window cut is applied.

Table 6.5: Breakdown of scaling factors in the electron channel for the ZZ resonance analysis. Only the statistical uncertainties are shown.

	N_A/N_C[MC]	N_B/N_D[MC]	N_B/N_D[Data]
Z mass	0.496 ± 0.001	0.519 ± 0.001	0.5081 ± 0.0006
Z_{P_T}/M_T	0.502 ± 0.002	0.519 ± 0.001	0.5081 ± 0.0006
$\Delta\phi$(jet, $E_{\mathrm{T}}^{\mathrm{miss}}$)	0.498 ± 0.001	0.519 ± 0.001	0.5082 ± 0.0006
B-tagged jet veto	0.524 ± 0.001	0.529 ± 0.001	0.5197 ± 0.0006
$E_{\mathrm{T}}^{\mathrm{miss}} > 30$ GeV	0.462 ± 0.003	0.386 ± 0.003	0.399 ± 0.001
$E_{\mathrm{T}}^{\mathrm{miss}} > 60$ GeV	0.39 ± 0.01	0.30 ± 0.007	0.306 ± 0.004
$E_{\mathrm{T}}^{\mathrm{miss}} > 90$ GeV	0.31 ± 0.02	0.30 ± 0.02	0.25 ± 0.01
$E_{\mathrm{T}}^{\mathrm{miss}} > 120$ GeV	0.29 ± 0.06	0.35 ± 0.10	0.18 ± 0.03
dR_{ll}	1.0 ± 0.3	1.2 ± 0.9	no event left

Table 6.6: Breakdown of scaling factors in the muon channel for the ZZ resonance analysis. Only the statistical uncertainties are shown.

	$N_{\mathrm{A}}/N_{\mathrm{C}}$[MC]	$N_{\mathrm{B}}/N_{\mathrm{D}}$[MC]	$N_{\mathrm{B}}/N_{\mathrm{D}}$[Data]
Z mass	0.501 ± 0.001	0.508 ± 0.001	0.4980 ± 0.0005
Z_{P_T}/M_T	0.505 ± 0.001	0.508 ± 0.001	0.4980 ± 0.0005
$\Delta\phi$(jet, $E_{\mathrm{T}}^{\mathrm{miss}}$)	0.502 ± 0.001	0.508 ± 0.001	0.4980 ± 0.0005
B-tagged jet veto	0.527 ± 0.001	0.518 ± 0.001	0.5093 ± 0.0005
$E_{\mathrm{T}}^{\mathrm{miss}} > 30$ GeV	0.456 ± 0.003	0.375 ± 0.003	0.389 ± 0.001
$E_{\mathrm{T}}^{\mathrm{miss}} > 60$ GeV	0.38 ± 0.01	0.29 ± 0.007	0.303 ± 0.004
$E_{\mathrm{T}}^{\mathrm{miss}} > 90$ GeV	0.33 ± 0.02	0.27 ± 0.02	0.29 ± 0.01
$E_{\mathrm{T}}^{\mathrm{miss}} > 120$ GeV	0.26 ± 0.05	0.21 ± 0.05	0.26 ± 0.03
dR_{ll}	0.7 ± 0.3	22 ± 31	no event left

Table 6.7: Breakdown of scaling factors in the electron channel for the dark matter analysis. Only the statistical uncertainties are shown.

	$N_{\mathrm{A}}/N_{\mathrm{C}}$[MC]	$N_{\mathrm{B}}/N_{\mathrm{D}}$[MC]	$N_{\mathrm{B}}/N_{\mathrm{D}}$[Data]
Z mass	0.496 ± 0.001	0.519 ± 0.001	0.5081 ± 0.0006
Z_{P_T}/M_T	1.049 ± 0.003	0.733 ± 0.002	0.7180 ± 0.0009
$\Delta\phi$(jet, $E_{\mathrm{T}}^{\mathrm{miss}}$)	1.018 ± 0.004	0.734 ± 0.002	0.7176 ± 0.0009
B-tagged jet veto	1.06 ± 0.004	0.743 ± 0.002	0.7283 ± 0.0009
$E_{\mathrm{T}}^{\mathrm{miss}} > 30$ GeV	0.626 ± 0.005	0.454 ± 0.003	0.470 ± 0.002
$E_{\mathrm{T}}^{\mathrm{miss}} > 60$ GeV	0.45 ± 0.01	0.337 ± 0.009	0.34 ± 0.005
$E_{\mathrm{T}}^{\mathrm{miss}} > 90$ GeV	0.31 ± 0.03	0.32 ± 0.03	0.28 ± 0.01
dR_{ll}	0.32 ± 0.08	0.2 ± 0.2	0.4 ± 0.4

Table 6.8: Breakdown of scaling factors in the muon channel for the dark matter analysis. Only the statistical uncertainties are shown.

	$N_{\mathrm{A}}/N_{\mathrm{C}}$[MC]	$N_{\mathrm{B}}/N_{\mathrm{D}}$[MC]	$N_{\mathrm{B}}/N_{\mathrm{D}}$[Data]
Z mass	0.501 ± 0.001	0.508 ± 0.001	0.4980 ± 0.0005
Z_{P_T}/M_T	1.043 ± 0.004	0.717 ± 0.002	0.7032 ± 0.0008
$\Delta\phi$(jet, $E_{\mathrm{T}}^{\mathrm{miss}}$)	1.089 ± 0.006	0.718 ± 0.002	0.7026 ± 0.0008
B-tagged jet veto	1.053 ± 0.004	0.727 ± 0.002	0.7133 ± 0.0008
$E_{\mathrm{T}}^{\mathrm{miss}} > 30$ GeV	0.604 ± 0.005	0.439 ± 0.003	0.456 ± 0.001
$E_{\mathrm{T}}^{\mathrm{miss}} > 60$ GeV	0.44 ± 0.01	0.33 ± 0.009	0.337 ± 0.004
$E_{\mathrm{T}}^{\mathrm{miss}} > 90$ GeV	0.34 ± 0.03	0.29 ± 0.02	0.31 ± 0.01
dR_{ll}	0.2 ± 0.1	0.2 ± 0.1	0.02 ± 0.26

Table 6.9: Final yields of the Z + jets background estimated using the ABCD method for both ZZ resonance and dark matter analyses. The uncertainties are statistical and systematic.

	electron channel	muon channel
High-mass	14.8 ± 4.8 ± 9.7	14.6 ± 4.6 ± 7.0
Low-mass	23 ± 5 ± 11	16.9 ± 5.2 ± 6.7

are determined by the data using fake-factor method. The fake-factor method estimates fake lepton background by applying the fake-factor to data events in a control region that is defined as requiring one electron or muon passing all the object selections and a lepton-like jet which fails the requirements on isolation or likelihood identification. The fake-factor is the probability ratio of a lepton and a lepton-like jet as a function of lepton η, as shown in the following equation :

$$F(\eta) = \frac{N_{\text{good}}(\eta)}{N_{\text{bad}}(\eta)} \tag{6.7}$$

Here, N_{good} (N_{bad}) is number of leptons (lepton-like jets). The fake factor is measured with a Tag and Probe method using Z+jets events. Table 6.10 shows the event selections for the Z+jets. The fake-factor is obtained as a function of η of leptons (or lepton-like jets).

Table 6.10: Event selection for Tag and Probe method with Z+jets events

Criteria	Selection
Tag lepton	2 good electrons or muons
Z-reconstruction	oppositely charged leptons and $\lvert M_{\ell\ell} - M_Z \rvert < 15$ GeV
Probe lepton	only one extra lepton

Table 6.11 shows the final yields of the W+jets background estimations using the fake-factor method. The final yields include statistical and systematic uncertainties. The fake-factor is also estimated with another tag and probe method using a W+jets events, Table 6.12. The systematic uncertainty is evaluated from the difference between W+jets definition and Z+jets definition.

Table 6.11: Final yields of the W+jets background estimation using the fake-factor method for both ZZ resonance and dark matter analyses. The uncertainties are statistical and systematic.

	electron channel	muon channel
High-mass	$0.13 \pm 0.03 \pm 0.03$	$0.20 \pm 0.27 \pm 0.15$
Low-mass	$0.18 \pm 0.04 \pm 0.04$	$0.36 \pm 0.46 \pm 0.08$

Table 6.12: Event selection for Tag and Probe method with W+jets events

Criteria	Selection
Tag lepton	1 good electron or muon
Probe lepton	only one extra lepton
$E_{\mathrm{T}}^{\mathrm{miss}}$	> 20 GeV

Chapter 7

Systematic Uncertainties

This part describes the systematic uncertainties considered for the background processes.

7.1 Theoretical uncertainties

Since MC-based estimation is used for WZ and ZZ backgrounds, theoretical uncertainties are considered as systematics.

7.1.1 WZ theoretical uncertainty estimation

The scale factor is defined as 1.25 ± 0.04 (stat) $\pm$ 0.05 (syst) estimated by 3l-CR. Here, the systematic uncertainty of the scale factor is taken to be the largest difference found among the average and each of the four channels. Furthermore, in the WZ background estimation, the shape uncertainties from the variation of QCD scale and the variation of PDF are considered since the normalization is fixed using the data yield in 3l-CR.

As the QCD scale uncertainties, the re-normalization and factorization scales are varied by factor of 1/2 or 2. The largest variation from the nominal scale combination is treated as systematic uncertainty.

To estimate the PDF uncertainties, the samples are re-weighted with different PDF sets. For WZ sample, the default PDF is CT10. The sample is re-weighted according to the weights calculated using PDF sets of MSTW2008nlo and NNPDF. The largest variation is taken into account as systematic uncertainty. The uncertainty on CT10 is derived by quadratically adding up all the 52 CT10 eigenvector variations.

The uncertainty is provided as a function of the invariant mass of W boson and Z boson system. The results of systematic uncertainty is shown in Figure 7.1.

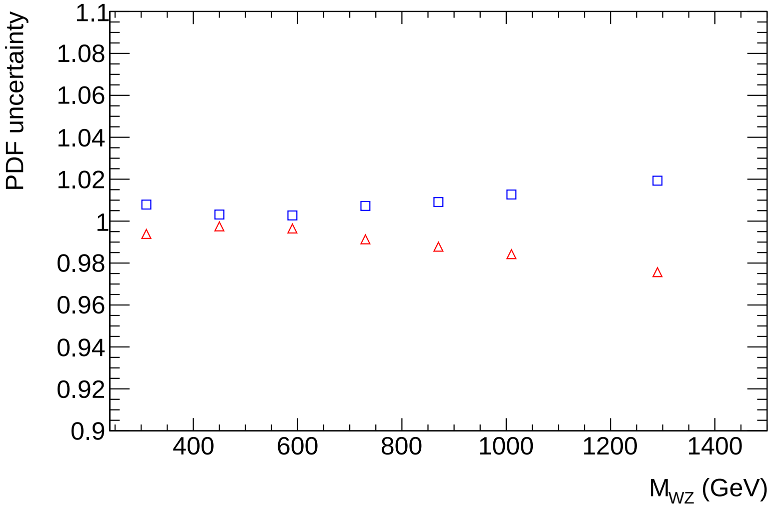

(a)

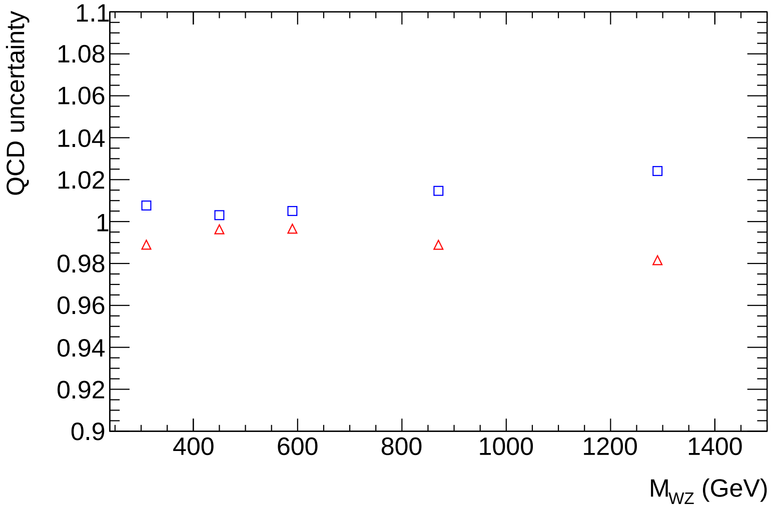

(b)

Figure 7.1: PDF (a) and QCD scale shape uncertainties as a function of the mass of the WZ system.

7.1.2 ZZ theoretical uncertainty estimation

For ZZ background, we rely on the MC prediction. Thus the cross section uncertainty on NNLO QCD correction and EW NLO correction are considered in addition to the QCD scale and PDF uncertainties.

The QCD uncertainties are estimated based on the variation of re-normalization and factorization by a factor of 1/2 or 2.

The PDF uncertainties are estimated based on re-weighting nominal ZZ sample with different PDF sets. The default PDF is CT10. The events re-weighted according to the weights calculated using PDF sets of MSTW2008nlo and NNPDF are considered. The uncertainty on CT10 is derived by quadratically adding up all the 52 CT10 eigenvector variations. Shape variation due to QCD scales for ZZ background is extracted the extreme variations of the QCD scale combinations.

Figure 7.2 shows the QCD and PDF uncertainties on ZZ background as a function of the mass of the ZZ system.

The NNLO cross section for ZZ background is calculated for on-shell Z in final state. The $gg \to ZZ$ background is also included in the calculation as part of NNLO calculation and therefore it needs to be factorized. The k-factor as function of m_{ZZ} is provided to re-normalize the POWHEG NLO $qq \to ZZ$ sample, as shown in Equation 7.1.

$$k(m_{ZZ}) = \frac{\sigma^{NNLO}_{qq\to ZZ}(m_{ZZ}, \mu = m_{ZZ}/2, CT10NNLO) - \sigma^{LO}_{gg\to ZZ}(m_{ZZ}, \mu = m_{ZZ}/2, CT10NNLO)}{\sigma^{NLO}_{gg\to ZZ}(m_{ZZ}, \mu = m_{ZZ}/2, CT10NLO)} \tag{7.1}$$

Roughly 6-8% increase in $qq \to ZZ$ cross section is estimated in ZZ resonance signal region, where about 4% come from the NNLO calculation and the rest comes from the change of central scale with respect to the Powheg nominal values.

NLO EW corrections are also considered in addition to QCD higher order correction. These corrections have a non-negligible effect on the $pp \to ZZ$ cross section. They are the same size as NNLO QCD correction. The k-factor is given in figure 4.1. As the uncertainty, the impacts of possible mixing of QCD and EW effects are considered. This uncertainty is adopted by the same approach with ref. [71] and found to have a small impact.

7.2 Experimental uncertainties

The uncertainties on the differences that can not be fully anticipated and caused by the detector performance are also considered as the systematic uncertainties. This section briefly summarizes the experimental uncertainties.

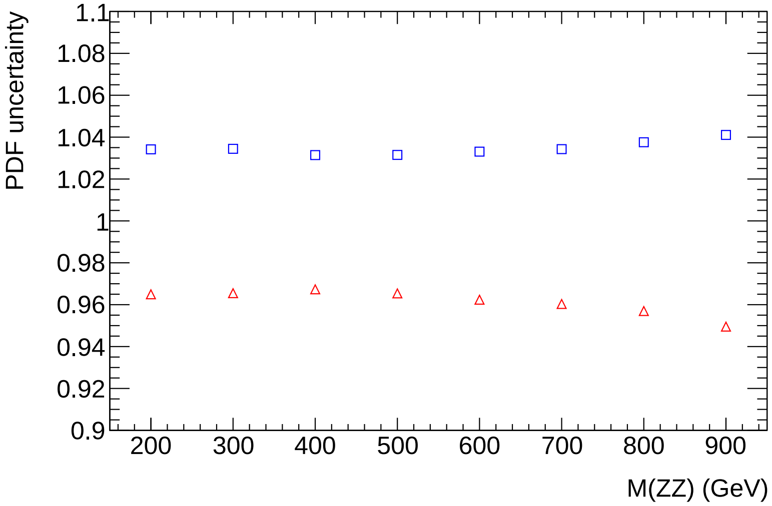

(a)

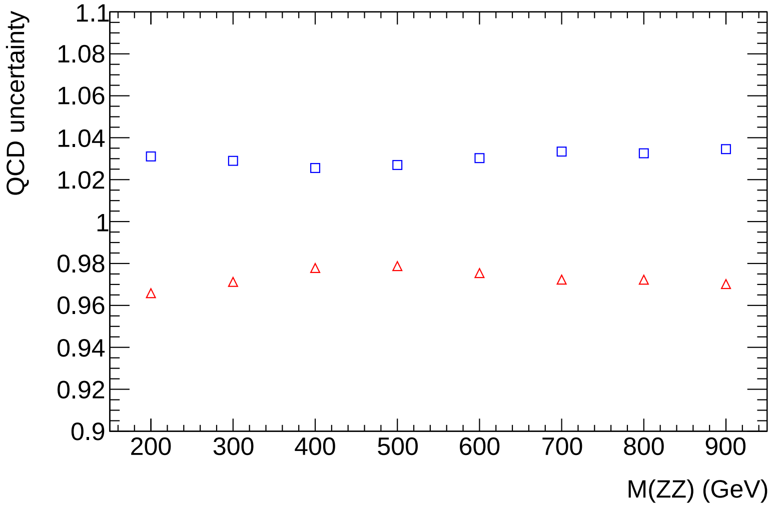

(b)

Figure 7.2: Theoretical systematic uncertainties on ZZ background due to QCD scale and PDF variations, as a function of the mass of the ZZ resonance.

7.2.1 Luminosity uncertainty

The uncertainty on the integrated luminosity is ±2.9% and is applied to signals and the background estimated from MC predictions. The method is estimated with the similar one in Ref. [72].

7.2.2 Pileup uncertainty

The pile-up re-weighting is applied to correct MC prediction to account for the data using μ (the average number of interactions per bunch crossing) and number of vertices distributions. The method is to assign different data μ scale values 1.0/1.0 and 1.0/1.23 and redo the pile-up re-weighting. The differences to the nominal results (1.0/1.16) are treated as systematic uncertainties.

7.2.3 Leptons

The systematic uncertainties for electron identification are considered for energy calibration, smearing, reconstruction and trigger efficiencies[73]. For muons, momentum calibration, smearing, reconstruction, identification, isolation and trigger efficiency are considered as the source for systematic uncertainties.

7.2.4 Jets

For uncertainties of jet energy scale and jet energy resolution, p_{T} and η dependence, pile-up conditions, flavor composition and high-pt jets are considered. Figure 7.3 and figure 7.4 show total uncertainties of jet energy scale and jet energy resolution, respectively.

In addition, the uncertainty of JVT efficiency is considered. The detail is described in Ref. [74].

7.2.5 Flavor tagging

A scale factor is applied to correct for the difference in b-tagging efficiencies between the data and the simulation since the b-jet veto is applied for both $Z + E_{\mathrm{T}}^{\mathrm{miss}}$ analyses. The uncertainties for the scale factor corrections on the tagging efficiency of bottom, charm and light jets are considered.

7.2.6 Missing transverse energy

In $Z + E_{\mathrm{T}}^{\mathrm{miss}}$ analyses, we estimate the systematic uncertainties on $E_{\mathrm{T}}^{\mathrm{miss}}$ soft term only for $E_{\mathrm{T}}^{\mathrm{miss}}$ since the effects on $E_{\mathrm{T}}^{\mathrm{miss}}$ from other terms are automatically considered when varying their corresponding objects uncertainties. The soft term uncertainties are obtained representing the uncertainties from the soft term resolution effect on the direction parallel

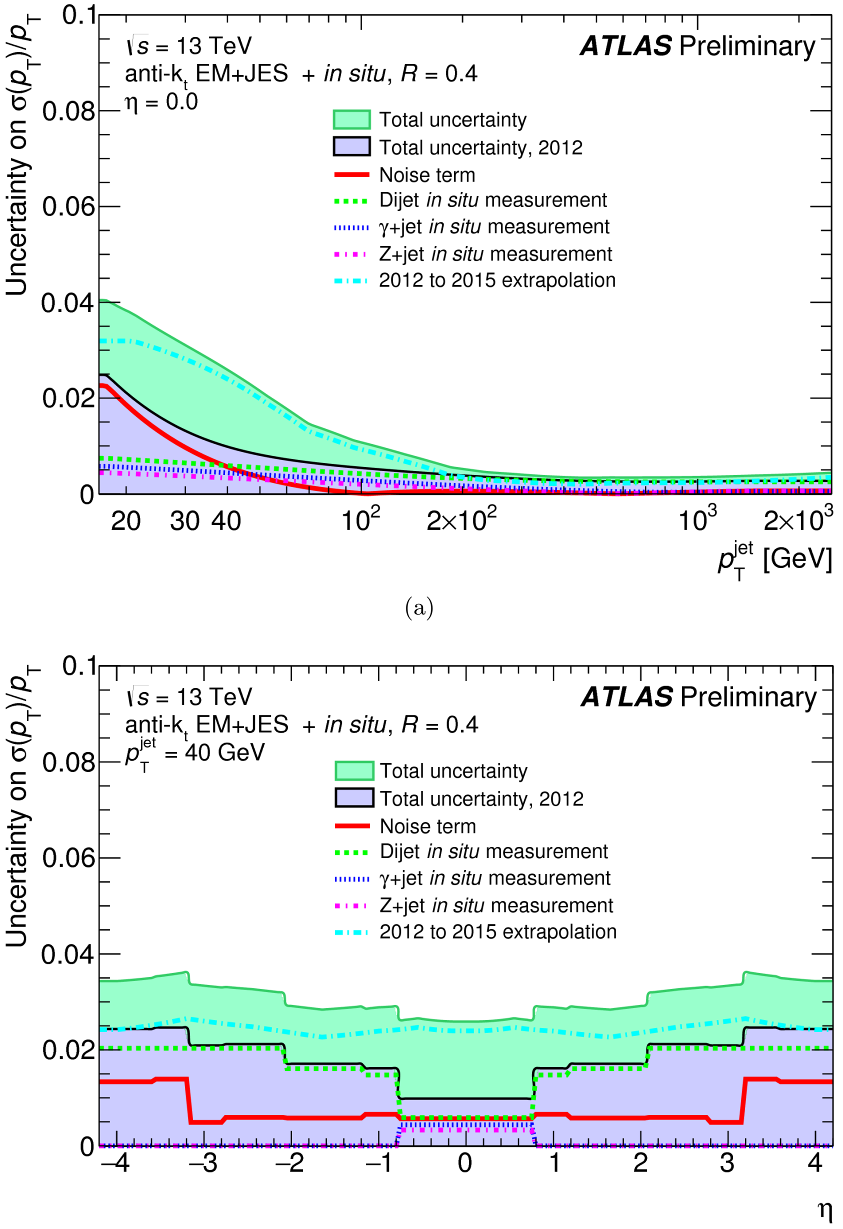

(a)

(b)

Figure 7.3: Final jet resolution uncertainties (a) as a function of jet p_{T} for jets of $\eta = 0$ and (b) as a function of η for jet p_{T} of 25 GeV[74].

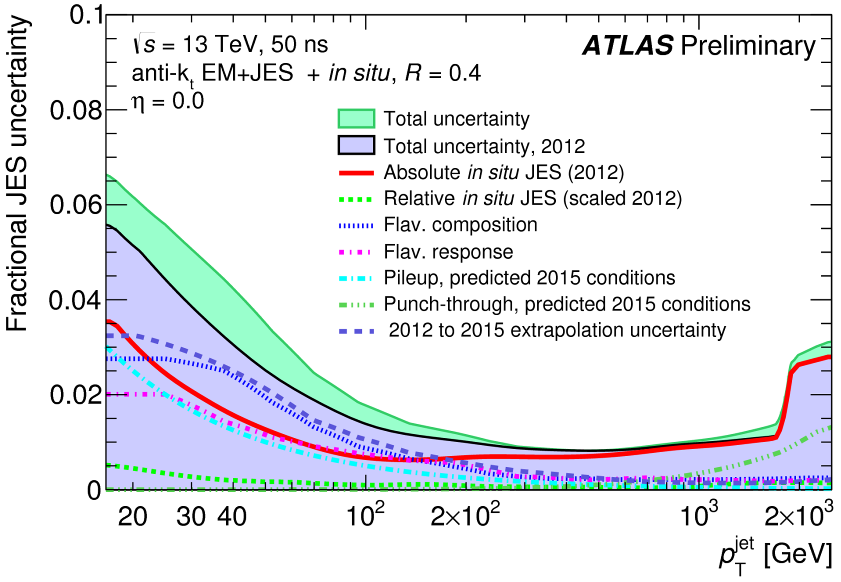

(a)

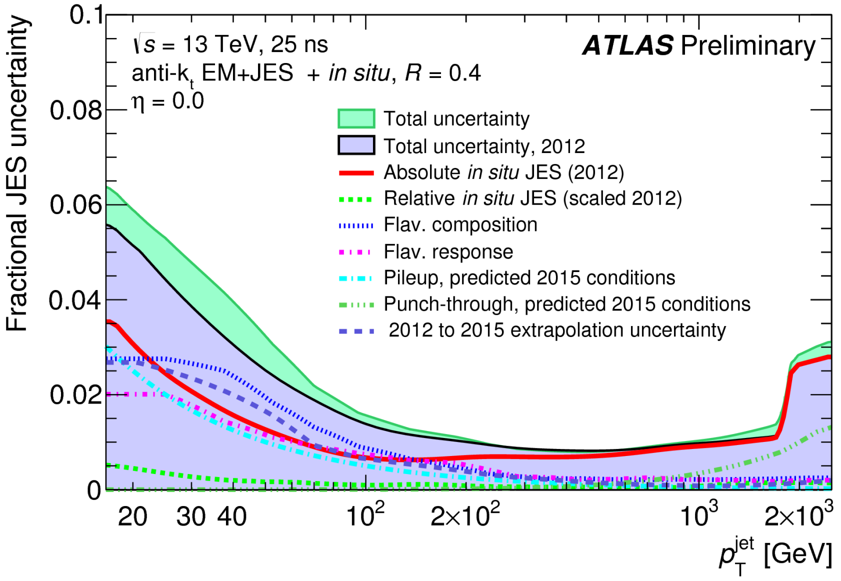

(b)

Figure 7.4: Final jet energy scale uncertainties as a function of jet p_{T} for jets of $\eta = 0$. Uncertainties are shown under the assumption of no knowledge of flavor. The total uncertainty is shown for the nominal data taking period with 25ns bunch spacing (a) and the early data taking period with 50ns bunch spacing (b)[74].

to the vector sum of hard objects $p_{\mathrm{T}}(p_{\mathrm{T}}^{hard})$, soft term resolution effect on the direction perpendicular to p_{T}^{hard} and the effect of soft term scale on the direction parallel to p_{T}^{hard}.

Chapter 8

Results

8.1 Likelihood definition

The m_T^{ZZ} and $E_{\mathrm{T}}^{\mathrm{miss}}$ distributions are used to set limits of the ZZ resonance and the dark matter searches, respectively. In each case, a profile-likelihood-ratio test statistic is used to check the compatibility between the data and predictions containing an injected signal contribution[75]. This section describes a brief introduction of limit setting method.

The statistical analysis of the data uses a binned likelihood function constructed as the product of Poisson probability terms,

$$Pois(n|\mu S + B) \prod_{b=1}^{n} \frac{\mu \nu_b^{\mathrm{sig}} + \nu_b^{\mathrm{bkg}}}{\mu S + B}, \tag{8.1}$$

where μ, the signal streangth parameter, multiples the expected signal yield ν_b^{sig} in each histogram bin b, and ν_b^{sig} represents the background content for bin b. The dependence of the signal and background predictions on the systematic uncertainties is described by a set of nuisance parameters (NP) θ, which are parameterised by Gaussian priors: the latter is used for normalization uncertainties in order to maintain a positive likelihood. The expected numbers of signal and background events in each bin are functions of θ and μ.

The priors act to constrain the NPs to their nominal values within their assigned uncertainties. They are implemented via so-called penalty or auxiliary measurements added to the likelihood which will always increase when any nuisance parameter is shifted from the nominal value. The likelihood function, $L(\mu, \theta)$, is therefore a function of μ and θ.

The nominal fit result in terms of μ and σ_μ is obtained by maximizing the likelihood function with respect to all parameters. This is referred to as the maximized log-likelihood value, MLL. The best statistic q_μ is then constructed according to the profile likelihood : $q_\mu = -2\ln(L(\mu, \hat{\hat{\theta}})/L(\hat{\mu}, \hat{\theta}))$, where $\hat{\mu}$ and $\hat{\theta}$ are the parameters that maximize the likelihood, and $\hat{\hat{\theta}}$ are the nuisance parameter values that maximize the likelihood for a given μ.

In the ZZ resonance search, the compatibility (p-value) between data and the assumed signal+background model with μ is tested using this test statistic. And any μ values that give p-value < 0.05 are excluded at 95% confidence level (CL). The observed 95% CL upper limit on production cross section of an additional heavy Higgs boson is then calculated as the observed upper limit on μ multiplying the predicted ggH production cross section as well as the branching fraction of the $H \rightarrow ZZ$ decay. The observed limit can be compared with the expected limit derived using an Asimov data-set created as the m_T distribution after profiling the background-only model to data. In this case, the $\pm 1\sigma$ and $\pm 2\sigma$ bands on the expected limits can also reported to test the compatibility between observed and expected limits. In all cases, the Asymptotic method [75] is used to find μ corresponding to p-value of 0.05 on the test statistic.

In the dark matter searches, the final discriminant distribution is $E_{\mathrm{T}}^{\mathrm{miss}}$. The corresponding limits on $\sigma(ZH \rightarrow \ell\ell + inv.)$ or mono-Z production cross section are calculated based on the limits on μ depending on the cross section for different theoretical models.

8.2 Fit inputs

A combined profile likelihood fit is performed for both the electron and muon channels. For each of these categories, the inputs to the likelihood are the final m_T^{ZZ} distributions for the ZZ resonance and the final $E_{\mathrm{T}}^{\mathrm{miss}}$ distributions for the dark matter searches.

In the ZZ resonance search, the fit range starts from 0 GeV and goes up to 1.5 TeV with a bin size of 50 GeV in most bins, except that for m_T^{ZZ} above 700 GeV, the distribution is binned as in order to maintain enough statistics in each high m_T^{ZZ} bins. The cut-off of 1500 GeV is chosen since the analysis is not sensitive for a ZZ resonance with $m_H > 1000$ GeV, and the cut-off has negligible impact on the signal and background yields. In any cases, the overflow events are included in the last bin.

In the dark matter searches, the fit range is from 90 GeV to 1000 GeV with various bin width. The bin boundaries are 90, 100, 120, 140, 160, 180, 200, 220, 240, 260, 280, 300, 1000 GeV, which are optimized in order to minimize the MC statistical uncertainty in each bin. The overflow events are added into the last bin.

Systematic uncertainties are considered using the m_T^{ZZ} and $E_{\mathrm{T}}^{\mathrm{miss}}$ distributions as $\pm 1\sigma$ variations.

As the background, the following processes are considered :

- ZZ background : The ZZ background is determined with the MC prediction, assigned full uncertainty including theoretical and experimental uncertainties.
- WZ background : The WZ background is determined with a partial data-driven method, assigned with data-driven uncertainty on the normalization as well as theoretical and experimental uncertainty on the shape.

- Top/$WW/Z\tau\tau$ backgrounds : The Top/$WW/Z\tau\tau$ backgrounds are determined using the $e\mu$ control region and the full uncertainty are extracted.
- W+jets background : The W+jets background is estimated using the fake-factor data-driven method.
- Z+jets background : The Z+jets background contribution in the current fit is determined with the ABCD method in a fully data-driven way and the MC shape has been used in the limit setting with considered shape uncertainty.

8.3 Results of the ZZ resonance search

This section contains the results of the ZZ resonance search. Observed and expected events after final selection are shown in Table 8.1. No significant excess of events is observed. Figure 8.1 shows the m_T^{ZZ} distributions in the ZZ resonance signal region in the ee, $\mu\mu$ and combined $ee + \mu\mu$ channels, respectively.

In the absence of a significant excess, limits are set on the existence of the new physics processes considered in this search. More specifically, upper limits on the production cross sections of the heavy Higgs boson and RS graviton are derived at 95% CL as a function the resonance mass using the signal region. The limits on $\sigma(pp \to H) \times BF(H \to ZZ)$ at 95% CL as a function of m_H from 300 GeV to 1 TeV are presented in Figure 8.2(a). The expected upper limits at 95% CL on $\sigma(pp \to H) \times BF(H \to ZZ)$ of a narrow width scalar boson decaying into ZZ are 107 and 53 fb at $m_H = 600$ GeV and 1 TeV, respectively. The observed limits are 69 and 37 fb for the respective mass points, and found to be consistent with the expectation within about one standard deviation. The results are also interpreted as a search for a RS graviton. The limits on $\sigma(pp \to G*) \times BF(G* \to ZZ)$ at 95% CL as a function of m_{G*} from 600 GeV to 1.2 TeV are shown in Figure 8.2(b). The predicted G* cross sections are also given in the figure, and the production of this particle is excluded up to 1.03 TeV using data and 1 TeV using the background-only expectation.

8.4 Results of the dark matter search

The $E_{\mathrm{T}}^{\mathrm{miss}}$ distributions after applying full event selections and with $ZH \to \ell\ell + inv.$ signals overlaid in signal regions are shown in Figure 8.3. The corresponding yields in signal regions for each background and signal are summarized in table 8.2. Since a significance excess does not exist, limits are set on the dark matter searches. The dark matter signal region is used to place the 95% CL limits on the production cross section of mono-Z signatures with different DM and mediator masses and ZH signal processes with the $Z \to \ell\ell$ and $H \to$ invisible decays. The cross section limit on the production of invisibly decaying Higgs boson associated with

Table 8.1: Observed data yields, signal expectations and estimated background contribution corresponding to 13.3 fb^{-1} in the ZZ resonance signal region. The first and second errors represent the statistical and systematic uncertainties, respectively. The systematic uncertainties of the MC-based predictions include the luminosity uncertainty. The total background prediction is given in the last row. The statistical uncertainty of the total background prediction is calculated as the quadratic sum of the statistical uncertainties from each background processes. To mimic the actual level of correlation between systematic uncertainties of each process, in the calculation of the systematic uncertainty of the total background estimate, the systematic uncertainties of MC-based estimates of the $qq \to ZZ$ and $t\bar{t}V/VVV$ backgrounds are first summed linearly and then quadratically combined with those uncertainties of predictions of other background processes.

ZZ Resonance Signal Region	ee	$\mu\mu$
Data	147	145
Signals		
Heavy Higgs ($m_H = 300$ GeV)	17.9 ± 0.6 ± 1.3	19.4 ± 0.6 ± 1.7
Heavy Higgs ($m_H = 600$ GeV)	29.6 ± 0.3 ± 1.6	28.5 ± 0.3 ± 2.1
Heavy Higgs ($m_H = 1$ TeV)	2.53 ± 0.03 ± 0.15	2.29 ± 0.02 ± 0.19
RS graviton ($m_{G^*} = 600$ GeV)	63.0 ± 1.3 ± 4.7	60.2 ± 1.2 ± 5.4
Backgrounds		
$qq \to ZZ$ (MC-based)	69.2 ± 1.3 ± 4.2	72.6 ± 1.3 ± 5.5
$gg \to ZZ$ (MC-based)	4.3 ± 0.1 ± 2.6	4.4 ± 0.1 ± 2.6
WZ (Data-driven)	35.3 ± 1.0 ± 2.6	39.9 ± 1.2 ± 2.6
$Z(\to ee, \mu\mu)$+jets (Data-driven)	14.8 ± 4.8 ± 9.7	14.6 ± 4.6 ± 7.0
non-resonant-$\ell\ell$ (Data-driven)	3.5 ± 1.3 ± 0.2	4.3 ± 1.6 ± 0.3
fake-lepton (Data-driven)	0.13 ± 0.03 ± 0.03	0.20 ± 0.27 ± 0.15
$t\bar{t}V/VVV$ (MC-based)	0.51 ± 0.02 ± 0.04	0.48 ± 0.02 ± 0.05
Total background	128 ± 5 ± 11	136 ± 5 ± 10

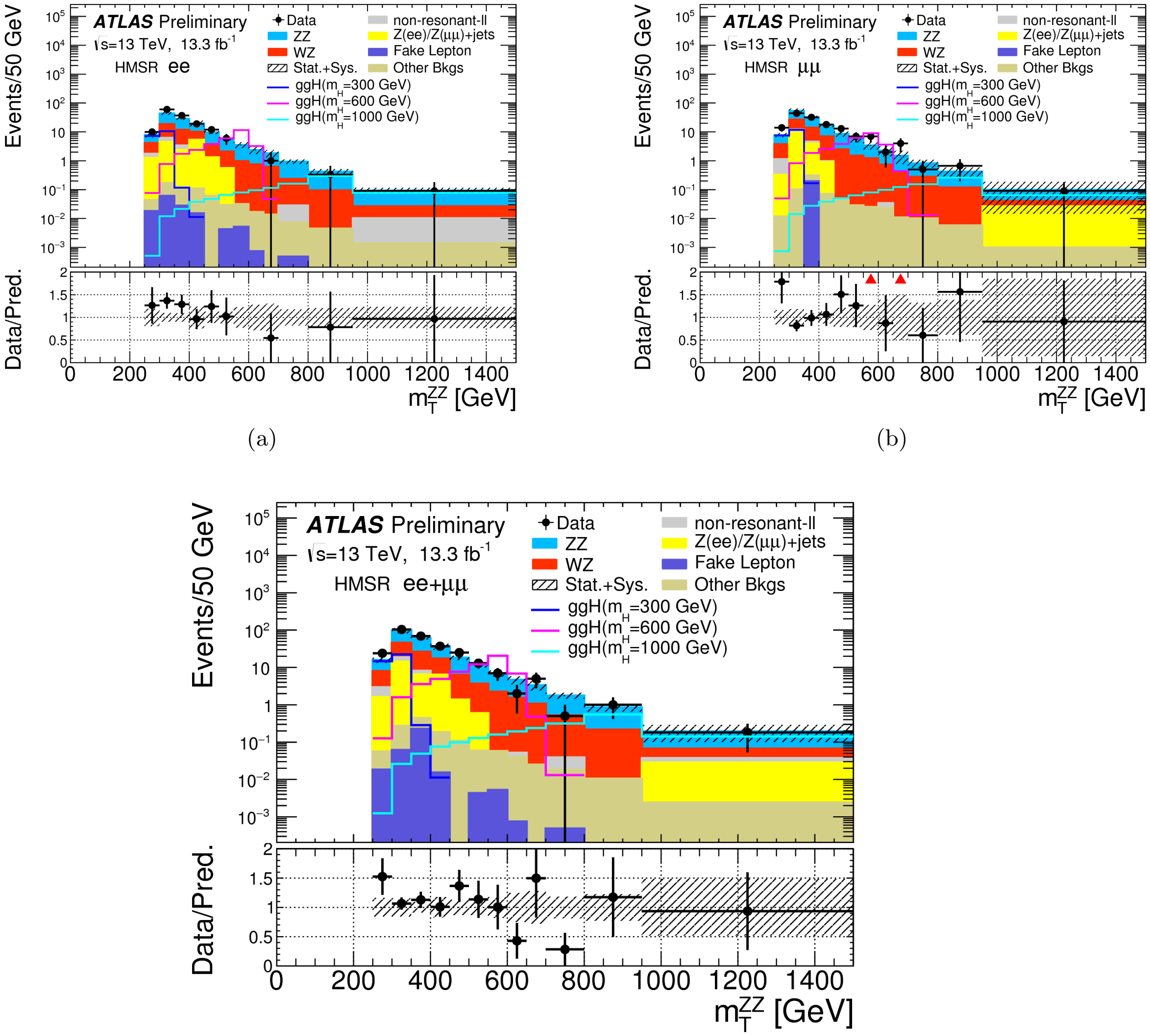

(a)

(b)

(c)

Figure 8.1: M_T^{ZZ} distribution in the ZZ resonance signal region for the (a)ee, (b)$\mu\mu$ and (c)combined $ee+\mu\mu$ channels. The stacked histograms represent the background predictions, while the blue, pink and cyan curves give the predicted signal distributions for a heavy Higgs boson with m_H = 300, 600 and 1000 GeV, respectively. The total uncertainty of the background expectation is shown in the gray shaded band. The number of entries in each bin corresponds to the number of events per 50 GeV.

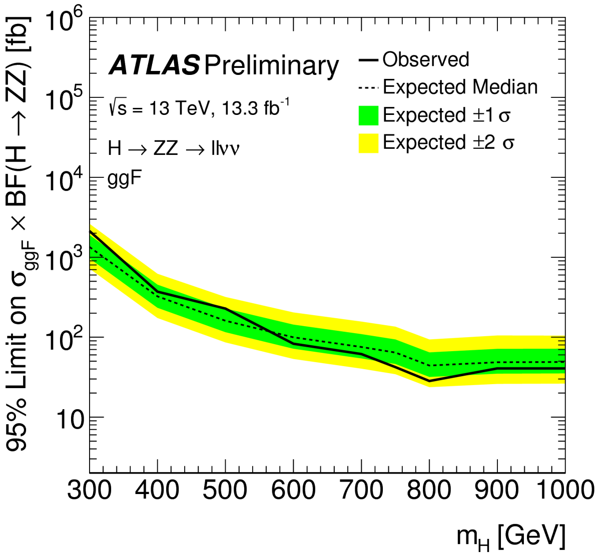

(a)

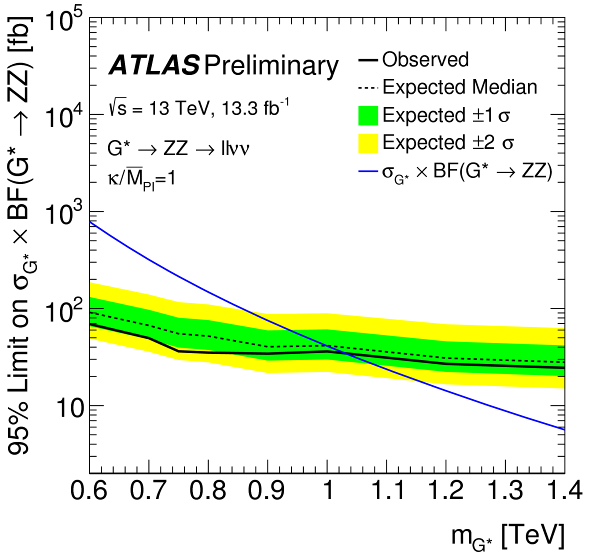

(b)

Figure 8.2: Limits on $\sigma(pp \to ZZ) \times BF(X \to ZZ)(X = H, G*)$ at 95% CL for (a) a narrow-width, heavy Higgs boson produced via gluon-gluon fusion and for (b) a RS graviton produced with $\kappa/\bar{M}_{Pl} = 1$(b). The green and yellow bands give the $\pm 1\sigma$ and $\pm 2\sigma$ uncertainties of the expected limits, respectively. The predicted production cross-sections as a function of the $G*$ mass are shown in the blue solid line.

a Z boson is further interpreted as the upper limit on the branching fraction of the $H \rightarrow$ invisible decay with $m_H = 125$ GeV.

Table 8.2: Observed data yields, signal expectations and estimated background contribution corresponding to 13.3 fb^{-1} in the dark matter search signal region. The first and second errors represent the statistical and systematic uncertainties, respectively. The systematic uncertainties of the MC-based predictions include the luminosity uncertainty. The total background prediction is given in the last row. The statistical uncertainty of the total background prediction is calculated as the quadratic sum of the statistical uncertainties from each background process. To mimic the actual level of correlation between systematic uncertainties of each process, in the calculation of the systematic uncertainty of the total background estimate, the systematic uncertainties of MC-based estimates of the $qq \rightarrow ZZ$ and $t\bar{t}V/VVV$ backgrounds are first summed linearly and then quadratically combined with uncertainties of predictions of other background processes.

Dark Matter Search Signal Region	ee	$\mu\mu$
Data	220	236
Signals		
ZH ($m_H = 125$ GeV) with BF($H \rightarrow inv.$)=100%	40.5 ± 1.2 ± 4.1	41.7 ± 1.2 ± 4.4
Mono-Z ($m_{DM} = 1$ GeV, $M_{med} = 10$ GeV)	175 ± 24 ± 14	169 ± 21 ± 22
Mono-Z ($m_{DM} = 50$ GeV, $M_{med} = 300$ GeV)	43.7 ± 2.3 ± 2.8	49.1 ± 2.6 ± 4.2
Backgrounds		
$qq \rightarrow ZZ$ (MC-based)	95.0 ± 1.5 ± 5.8	102.1 ± 1.6 ± 8.0
$gg \rightarrow ZZ$ (MC-based)	5.6 ± 0.1 ± 3.3	5.7 ± 0.1 ± 3.4
WZ (Data-driven)	44.0 ± 1.1 ± 3.3	50.5 ± 1.2 ± 3.3
$Z(\rightarrow ee, \mu\mu)$+jets (Data-driven)	23 ± 5 ± 11	16.9 ± 5.2 ± 6.7
non-resonant-$\ell\ell$ (Data-driven)	16.9 ± 2.8 ± 1.0	20.7 ± 3.4 ± 1.2
fake-lepton (Data-driven)	0.18 ± 0.04 ± 0.03	0.36 ± 0.46 ± 0.08
$t\bar{t}V/VVV$ (MC-based)	0.44 ± 0.02 ± 0.06	0.43 ± 0.02 ± 0.06
Total background	185 ± 6 ± 13	196 ± 7 ± 12

Table 8.3 shows the 95% CL upper limits on the production cross section of the $Z(\rightarrow \ell\ell)H(\rightarrow$invisible) processes and the $H \rightarrow$ invisible decay branching fraction. Figure 8.4 shows a distribution of the confidence levels corresponding to each value of upper limits on $\sigma(Z(\rightarrow \ell\ell)H(\rightarrow$ invisible)) normalized by the SM prediction of the ZH production cross section scanned from 0 to 1.4. The shown confidence levels can be interpreted as that on the upper limits of BF($H \rightarrow$ invisible), for the region with the x-axis value less than one. The expected and observed upper limit on BF($H \rightarrow$ invisible) at 95% CL is 65% and 98%, respectively. The observed limit is larger than expectation, and this is caused by the moderate data excess in the $E_{\mathrm{T}}^{\mathrm{miss}}$ distributions in both the ee and $\mu\mu$ channels, as shown in Figure 8.3.

Since we observe sizable data/MC discrepancy in $E_{\mathrm{T}}^{\mathrm{miss}}$ distribution, especially in 90 - 100 GeV bin, some dedicated studies have been done to check the origin and the properties of

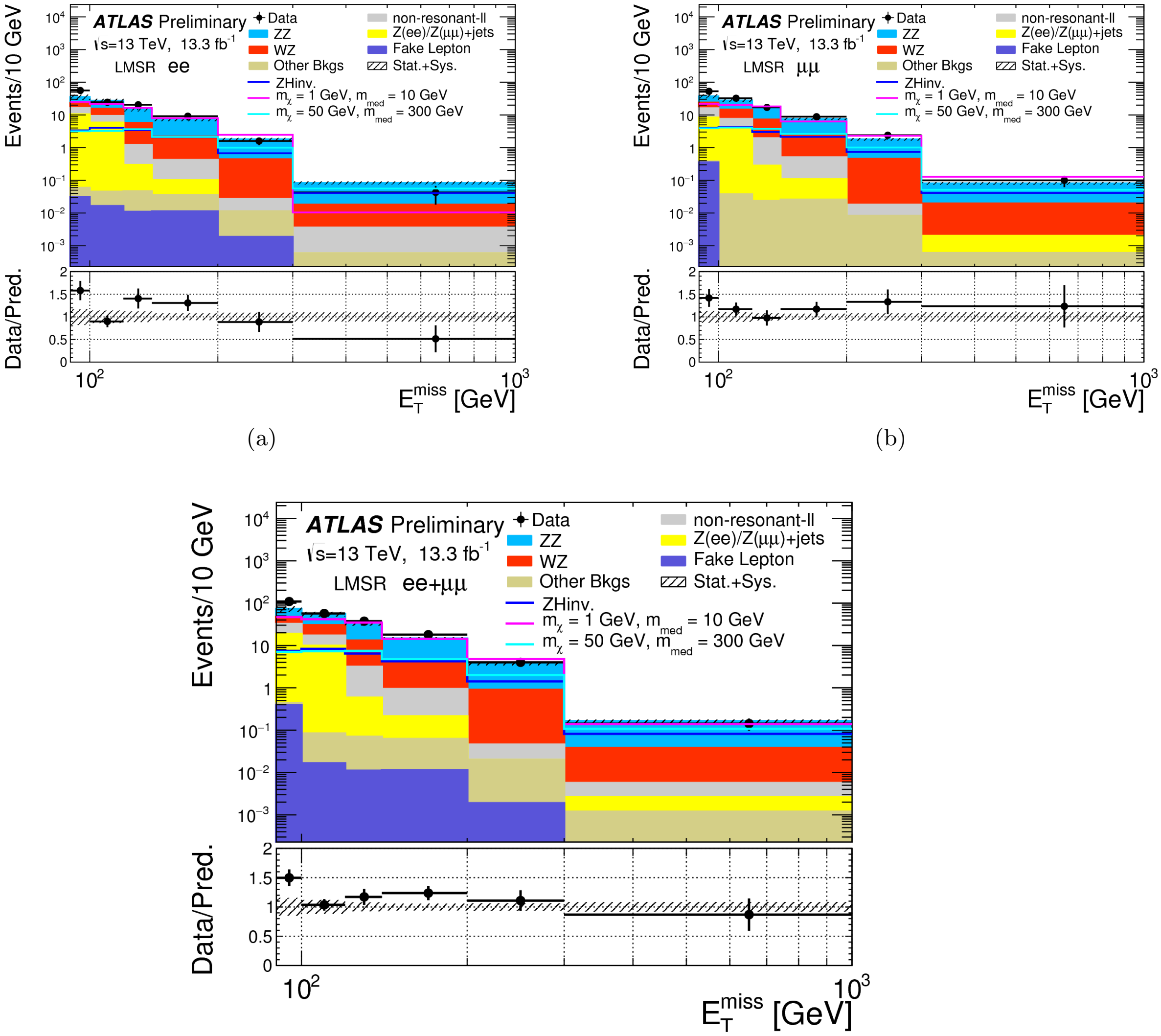

(a)

(b)

(c)

Figure 8.3: $E_{\mathrm{T}}^{\mathrm{miss}}$ distributions in the dark matter search region for the (a)ee, (b)$\mu\mu$ and (c) combined $ee + \mu\mu$ channels. The stacked histograms represent the background predictions, while the blue, pink and cyan curves give the predicted signal distributions for the $ZH \to \ell\ell + inv.$ process, and the mono-Z signatures with (m_X = 1 GeV, m_{med} = 10 GeV) and (m_X = 50 GeV, m_{med} = 300 GeV), respectively. The total uncertainty of the background expectation is shown in the gray shaded band. The number of entries in each bin corresponds to the number of events per 10 GeV.

these events. This study is described in Appendix C.3.

Table 8.3: The 95% CL upper limits on $\sigma(Z(\rightarrow \ell\ell)H(\rightarrow inv.))$ and branching fraction of the $H \rightarrow inv.$ decay. Both expected and observed limits are given, and the $\pm 1\sigma$ and $\pm 2\sigma$ variations of the expected limits are provided as well.

	Limits on $\sigma(Z(\rightarrow \ell\ell)H(\rightarrow inv.))$ [fb]		Limits on BF$(H \rightarrow inv.)$	
	Expected	Observed	Expected	Observed
Central Value	58	88	65%	98%
$(-1\sigma, +1\sigma)$	(41, 83)		(46%, 93%)	
$(-2\sigma, +2\sigma)$	(30, 115)		(34%, 100%)	

Figure 8.5 shows the exclusion limits for the mono-Z signals with a vector mediator and coupling parameters $g_X = 1.0$ and $g_q = 0.25$ in two-dimensional phase space of dark matter and mediator masses (m_X and m_{med}). The 2-dimensional contours are produced by interpolating between the cross section limits derived from a limited number of MC samples, and this causes the resulting contours to be slightly non-smooth.

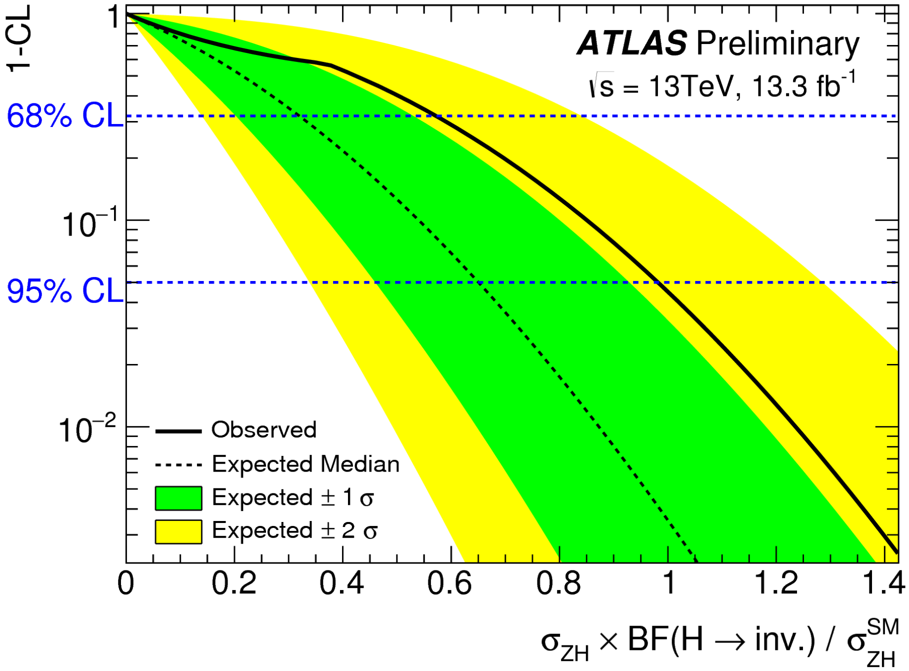

Figure 8.4: Confidence levels corresponding to upper limits on $\sigma_{ZH} \times BF(H \rightarrow inv.)/\sigma_{ZH}^{SM}$(with $m_H = 125$ GeV) scanned from 0 to 1.4. The expected and observed confidence levels are shown as the dashed black and solid black lines, respectively. The green and yellow bands give the $\pm 1\sigma$ and $\pm 2\sigma$ uncertainties of the expected confidence levels, respectively. The shown confidence levels can be interpreted as those on the upper limits on BF($H \rightarrow inv.$), for the region with the x-axis value less than one. The 95% CL upper limit on BF($H \rightarrow inv.$) can be read from the crossing points between the dashed blue 95% CL line and the respective confidence level curve.

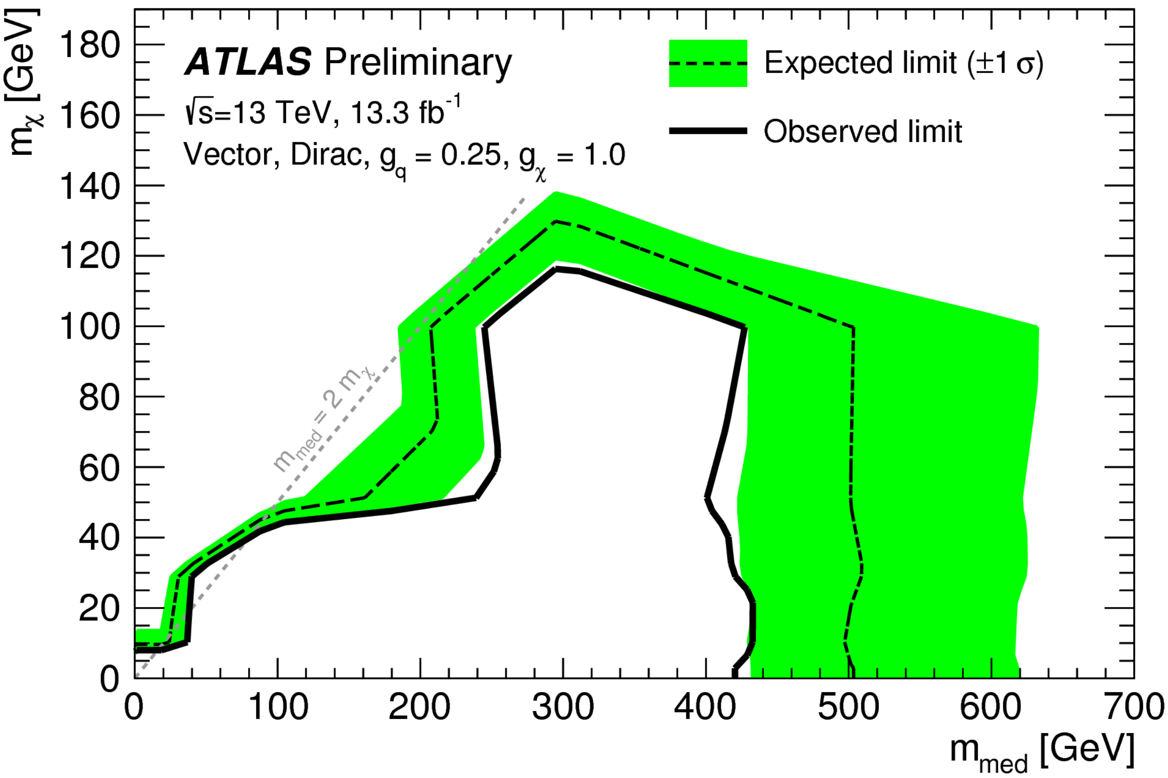

Figure 8.5: Exclusion limits for mono-Z dark matter signals with vector mediator and coupling parameters $g_x = 1.0$ and $g_q = 0.25$ in the 2-dimensional phase space of dark matter and mediator masses (m_X and m_{med}). The dashed gray line indicates the kinematic threshold where the mediator can decay on-shell into dark matter. The region below the dashed blue line is excluded at 95% CL based on the background only expectation, and the green band gives the 1 σ uncertainty of the expected exclusion limits. The phase space circled by the solid black line is excluded using data at 95% CL. The 2-dimensional contours are produced by interpolating between the cross section limits derived from a limited number of MC samples, and this causes the resulting contours to be slightly non-smooth.

Chapter 9

Conclusion

We have searched for physics beyond the standard model with a final state containing a Z boson and invisible particles. The analyses are especially optimized to address three searches : (1) new heavy particle resonances decaying to the $ZZ \rightarrow \ell\ell\nu\nu$ final state; (2) the decay of the 125 GeV/c^2 Higgs boson to invisible particles in the production channel $pp \rightarrow ZH$ with $Z \rightarrow \ell\ell$; and (3) production of dark matter particles in association with a Z boson with $Z \rightarrow \ell\ell$. The analysis has been performed using proton-proton collisions at a center-of-mass energy of 13 TeV corresponding to an integrated luminosity of 13.3 fb^{-1} collected with the ATLAS detector at the LHC.

No significant deviations from the Standard Model expectations are observed. We thus have placed constraints on new physics effects. For the new heavy resonance search, upper limits on the production cross section of a bulk Rundall-Sundrum graviton and the masses smaller than 1.03 TeV are excluded at the 95% confidence level (CL). An upper limit is also set on the branching fraction of the Higgs boson decays to invisible particles to be 98.2% at the 95% CL. Finally exclusion limits are placed on the dark matter production through a vector mediator in a 2-dimensional phase space of dark matter and mediator masses.

Appendix A

Distribution of variables used in event selection for events with $E_{\mathrm{T}}^{\mathrm{miss}} > 120$ GeV

This appendix contains plots to show the variables used in the event selection applying the cut on the missing transverse energy $E_{\mathrm{T}}^{\mathrm{miss}} > 120$ GeV.

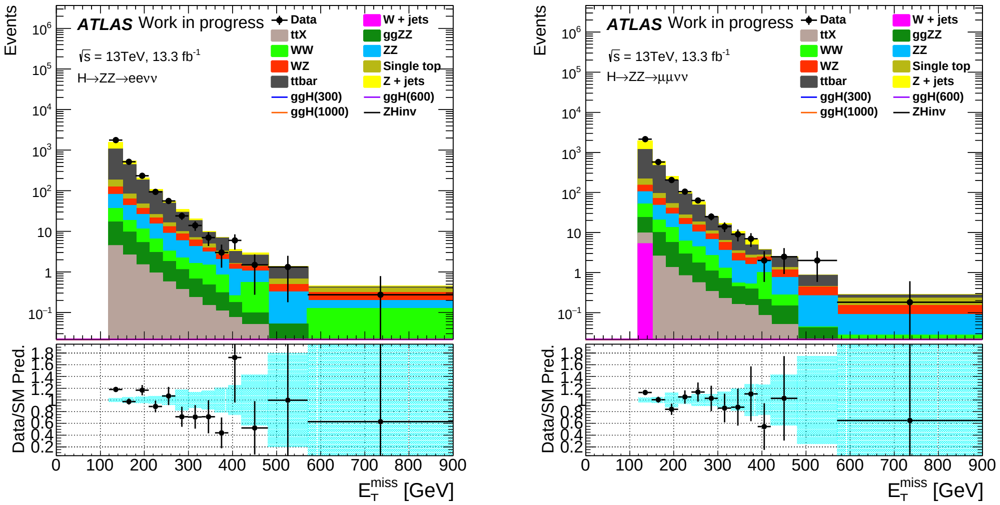

(a)

(b)

Figure A.1: Missing transverse energy distribution in the (a) electron channel and the (b) muon channel.

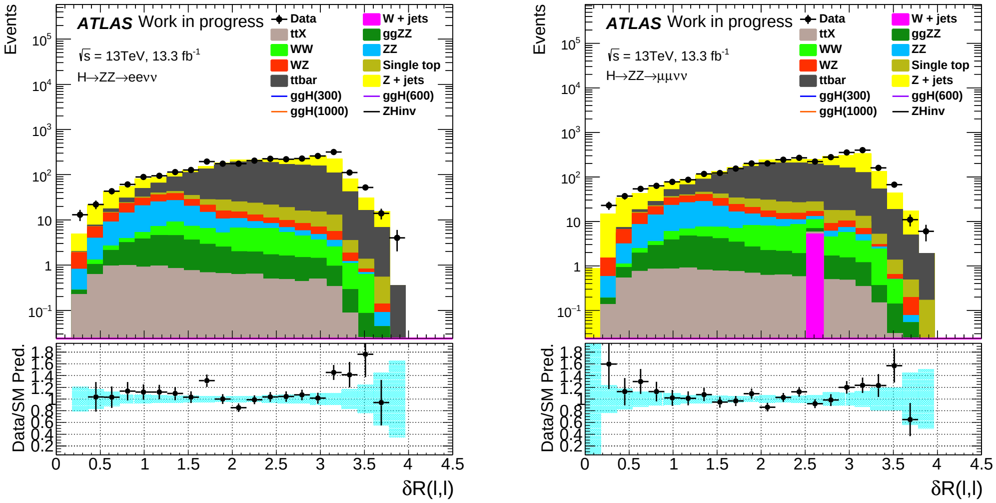

(a) (b)

Figure A.2: Distance between leptons (ΔR_{ll}) in the (a) electron channel and the (b) muon channel.

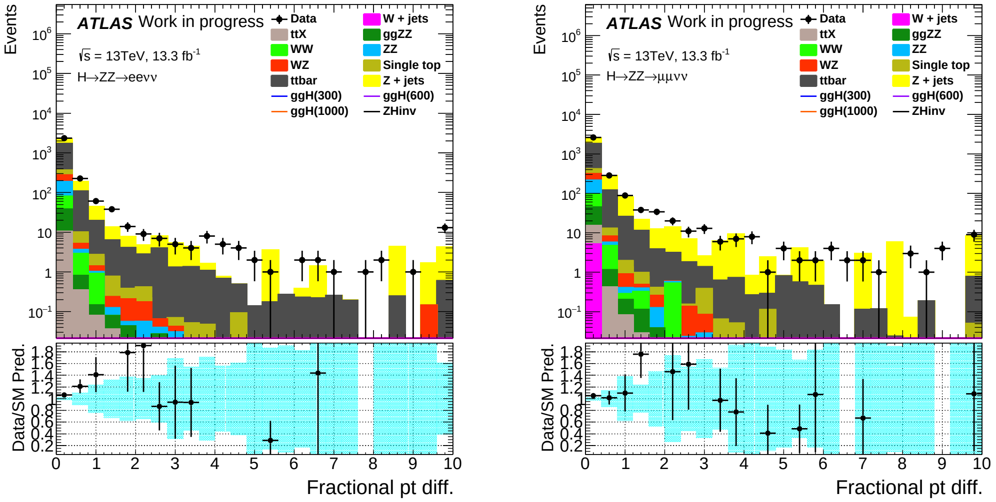

(a) (b)

Figure A.3: Fractional p_{T} difference distributions in the (a) electron channel and (b) muon channel.

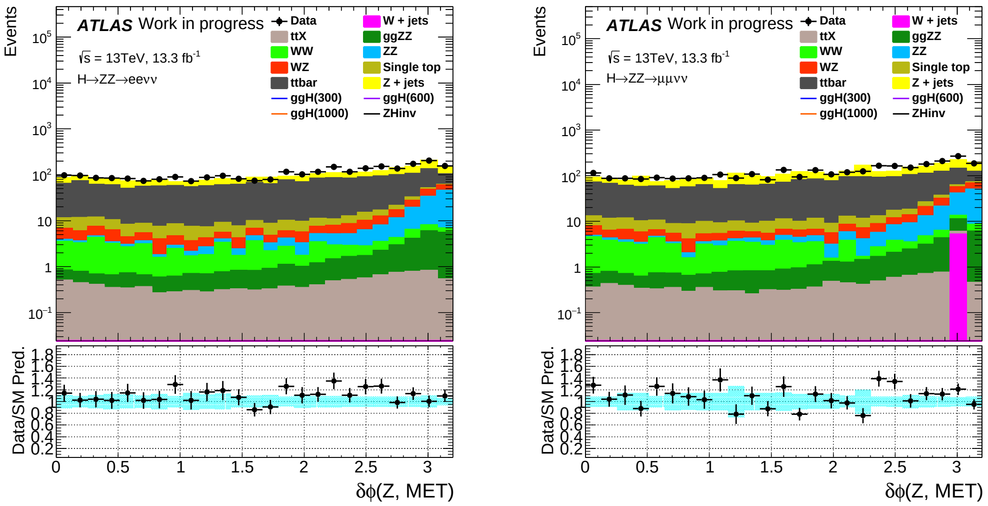

(a) (b)

Figure A.4: $\Delta\phi(Z, E_{\mathrm{T}}^{\mathrm{miss}})$ distributions in the (a) electron channel and (b) muon channel.

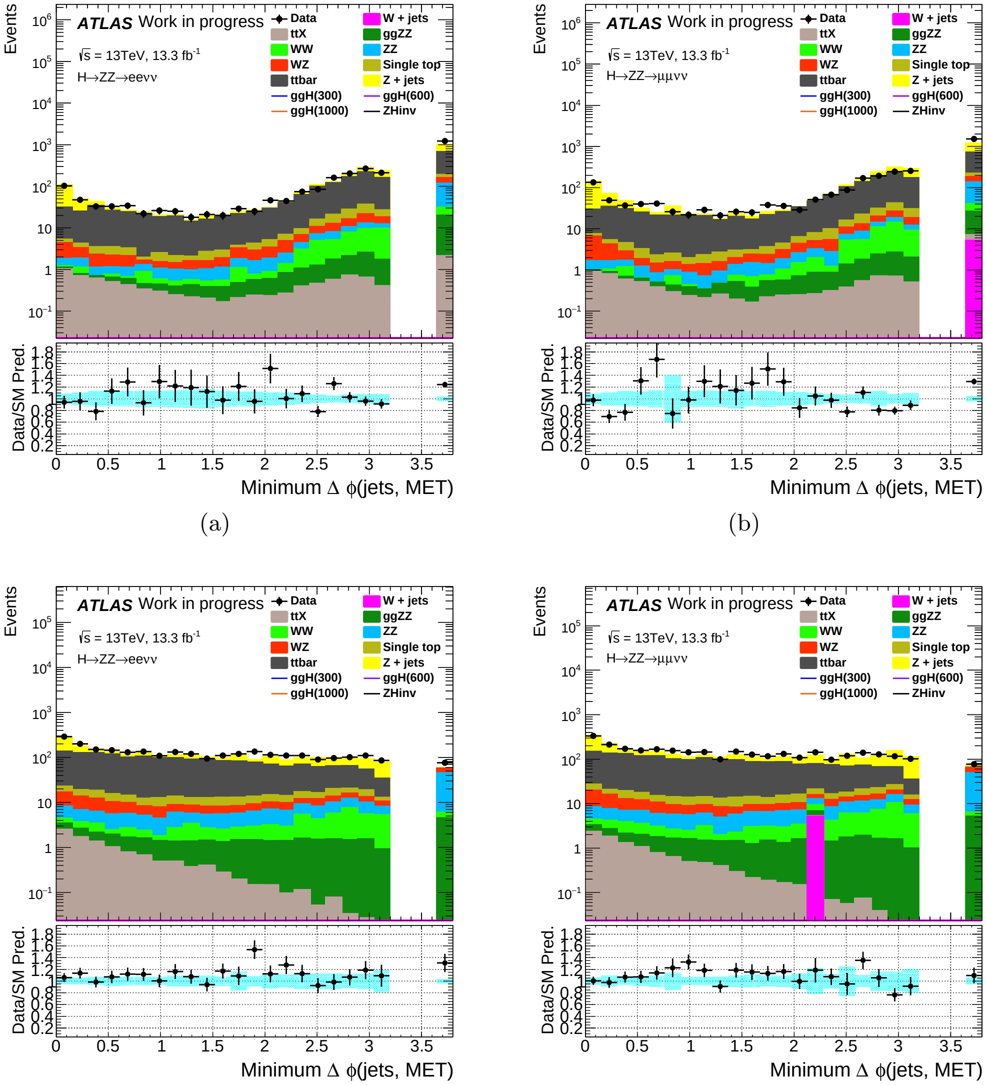

(a) (b)

(c) (d)

Figure A.5: Minimum $\Delta\phi(jets, E_{\mathrm{T}}^{\mathrm{miss}})$ distributions with events that have jets with $p_{\mathrm{T}} >$ 100 GeV (top two plots) or with $p_{\mathrm{T}} >$ 25 GeV in the electron channel (left two plots) and muon channel (right two plots). The events which do not have jets are added to the overflow bin.

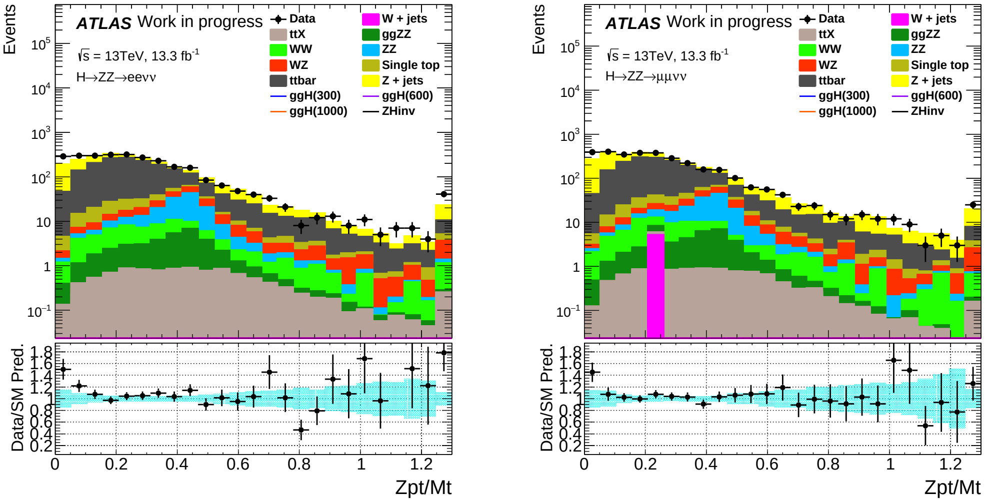

(a)

(b)

Figure A.6: $p_{\mathrm{T}}^{Z}/m_{T}^{ZZ}$ distributions in (a) the electron channel and (b) the muon channel.

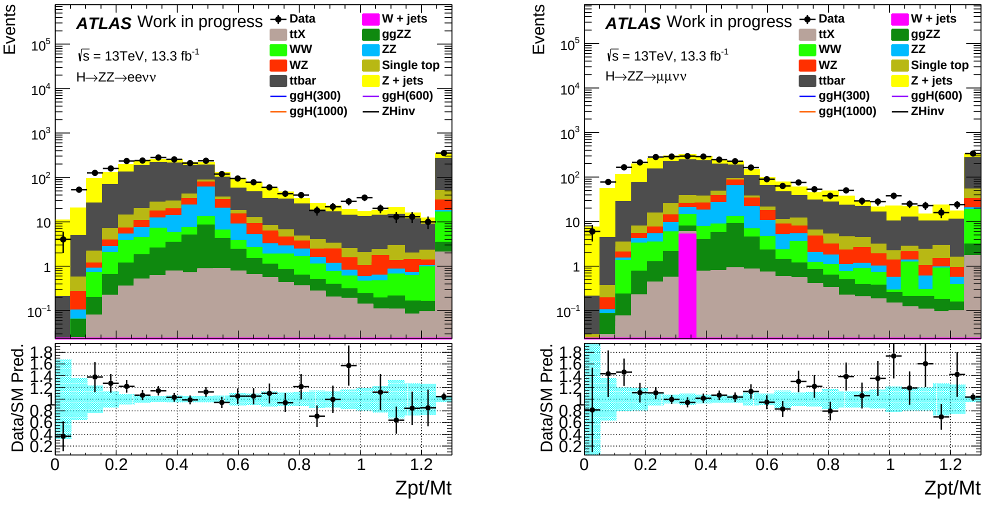

(a)

(b)

Figure A.7: p_{T}^{Z}/m_{T} distributions in (a) the electron channel and (b) the muon channel.

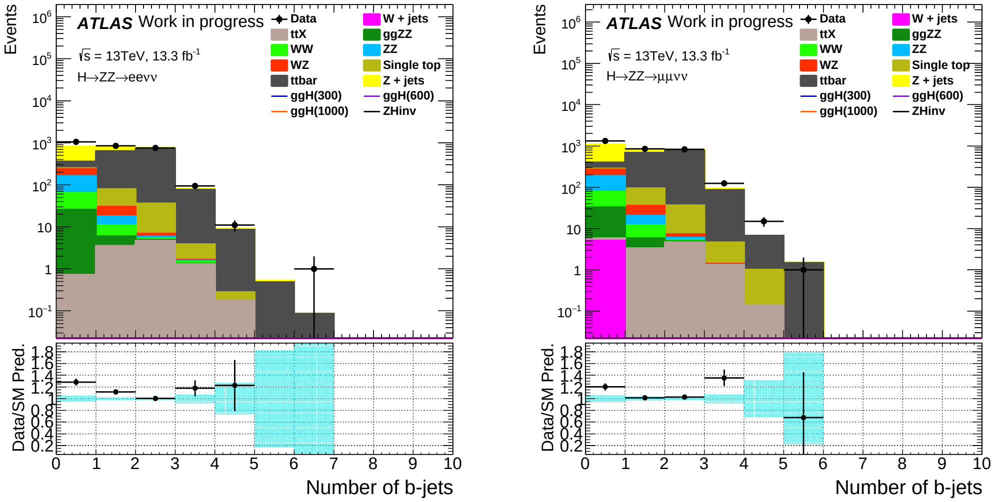

(a) (b)

Figure A.8: Number of b-tagged jets distributions in (a) the electron channel and (b) the muon channel.

Appendix B

Data-driven estimation of $ZZ \to \ell\ell\nu\nu$ background using $WZ \to \ell\nu\ell\ell$

B.1 Introduction

The $ZZ \to \ell\ell\nu\nu$ process is the dominant background in both $Z + E_{\mathrm{T}}^{\mathrm{miss}}$ analyses. In current status, $ZZ \to \ell\ell\nu\nu$ is estimated with MC prediction for both shape and normalization as described in section 7.1. Since the theoretical uncertainty of the ZZ background has large impact on the limit, it is preferred to replace the current estimation with data-driven estimation. If the data-driven method is difficult to adopt the analyses, MC prediction should be confirmed with data using control region.

An idea is to use 3l-CR for estimation of ZZ background. Kinematics of ZZ and WZ is expected to be similar due to the similar production diagrams, thus 3l-CR can be used to estimate of $ZZ \to \ell\ell\nu\nu$ background with data once we have enough statistics. In this method, lepton from W boson decay is treated as missing transverse momentum. With limited amount of data, this control region can be used to validate the $ZZ \to \ell\ell\nu\nu$ MC-based estimation.

B.2 Shape comparison and consideration of the correction

First of all, we tried to compare $WZ \to \ell\nu\ell\ell$ in 3l-CR with $ZZ \to \ell\ell\nu\nu$ with events that pass the Z boson mass requirement and third-lepton veto. Figure B.1 - figure B.2 show the comparison between $WZ \to \ell\nu\ell\ell$ MC and $ZZ \to \ell\ell\nu\nu$ in events applying Z mass requirement and third-lepton veto.

As can be seen in these plots, the large differences appear in distributions used for event selection, for example, $\Delta R_{\ell\ell}$, $\Delta\phi(Z, E_{\mathrm{T}}^{\mathrm{miss}})$, fractional p_{T} difference. Thus the method needs the function to correct the difference between $WZ \to \ell\nu\ell\ell$ and $ZZ \to \ell\ell\nu\nu$. In the $Z_{p_{\mathrm{T}}}$ dis-

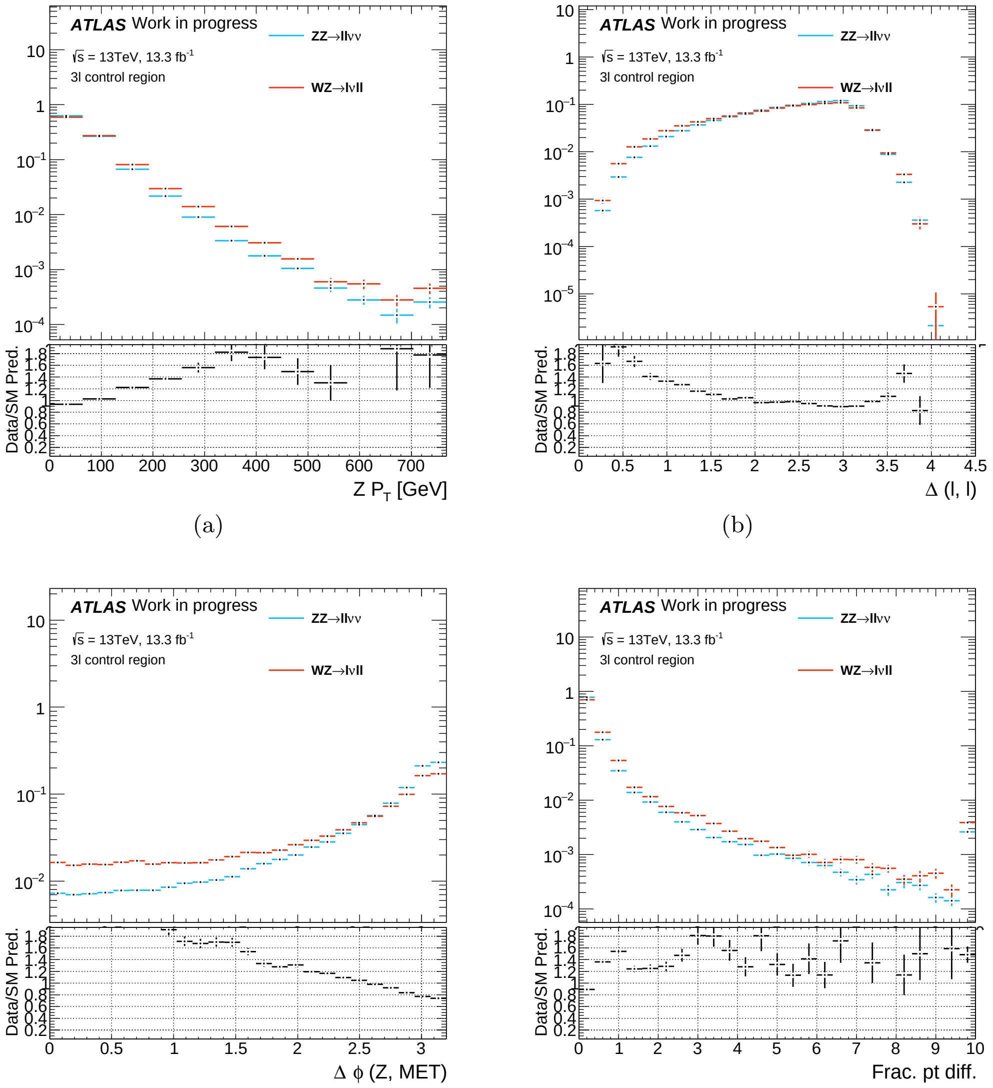

(a) (b)

(c) (d)

Figure B.1: $WZ \to \ell\nu\ell\ell$ in 3l-CR and $ZZ \to \ell\ell\nu\nu$ in signal region compared for (a) Z boson p_{T}, (b) $\Delta R_{\ell\ell}$, (c) $\Delta\phi(Z, E_{\mathrm{T}}^{\mathrm{miss}})$ and (d) fractional p_{T} difference. The events are applied with Z mass requirement and third-lepton veto.

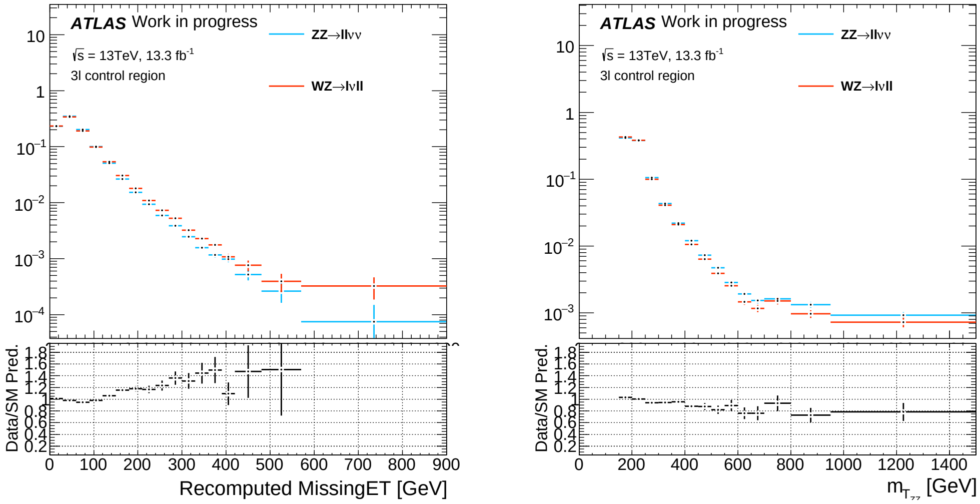

(a) (b)

Figure B.2: $WZ \to \ell\nu\ell\ell$ in 3l-CR and $ZZ \to \ell\ell\nu\nu$ in signal region compared for (a) $E_{\mathrm{T}}^{\mathrm{miss}}$ and (b) transverse mass of di-boson resonance. The events are applied Z mass requirement and third-lepton veto.

tribution, $WZ \to \ell\nu\ell\ell$ process is larger than $ZZ \to \ell\ell\nu\nu$ process in the high $Z_{p_{\mathrm{T}}}$ region. This difference is caused by $\hat{s}$ difference between WZ and ZZ processes from the mass difference between W and Z. For the other distributions, the reason of the difference can be considered the same since these variables are chosen to separate the signal and $ZZ \to \ell\ell\nu\nu$ background using their $\hat{s}$ difference. Thus, we take the transverse momentum of di-boson resonance as a correction function to directly correct for the $\hat{s}$ difference. Figure B.3 shows the transverse momentum of di-boson resonance. The correction function is a bin-by-bin re-weighting of the di-boson p_{T} distribution.

Figure B.4 - Figure B.5 show distributions with the correction applied. For most of variables, the difference is smaller than without the correction. In low $E_{\mathrm{T}}^{\mathrm{miss}}$ and m_T regions, the difference still exist. However, most of the events after all event selections are populated in high $E_{\mathrm{T}}^{\mathrm{miss}}$ and m_T regions, and therefore the difference can be ignored.

Figure B.6 - figure B.7 show the comparison between data in 3l-CR subtracted all the contribution except for WZ and $ZZ \to ll\nu\nu$ in events applying Z mass requirement and third-lepton veto. The behavior is really similar to comparison between simulations as shown in figure B.4 - figure B.5.

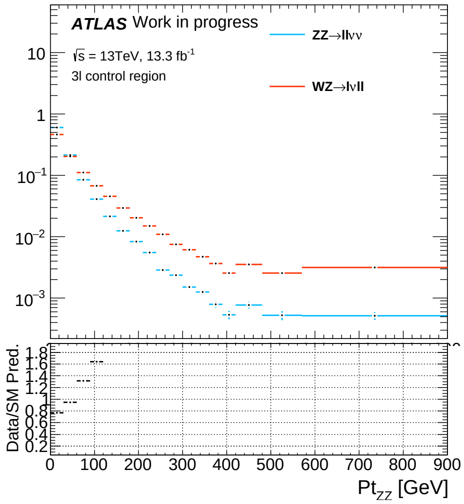

Figure B.3: $WZ \rightarrow \ell\nu\ell\ell$ in 3l-CR and $ZZ \rightarrow \ell\ell\nu\nu$ in signal region compared for transverse momentum of di-boson resonance. The events are applied with Z mass requirement and third-lepton veto.

B.3 Results

Figure B.8 shows the final $E_{\mathrm{T}}^{\mathrm{miss}}$ distribution with applying all requirements developed for the Higgs invisibly decaying analysis and the final m_T^{ZZ} distribution with applying all those the high mass Higgs analysis. The data have very similar in shape to the ZZ MC prediction. However, the statistics is not enough to compare the shapes in high $E_{\mathrm{T}}^{\mathrm{miss}}$ and m_T^{ZZ} regions. The shape difference between ZZ and WZ may be present, since $WZ \rightarrow \ell\nu\ell\ell$ process can be produced via s-channel in addition to t-channel. If the shapes turn out not in good agreement with each other as we collect more data, we need to develop different function.

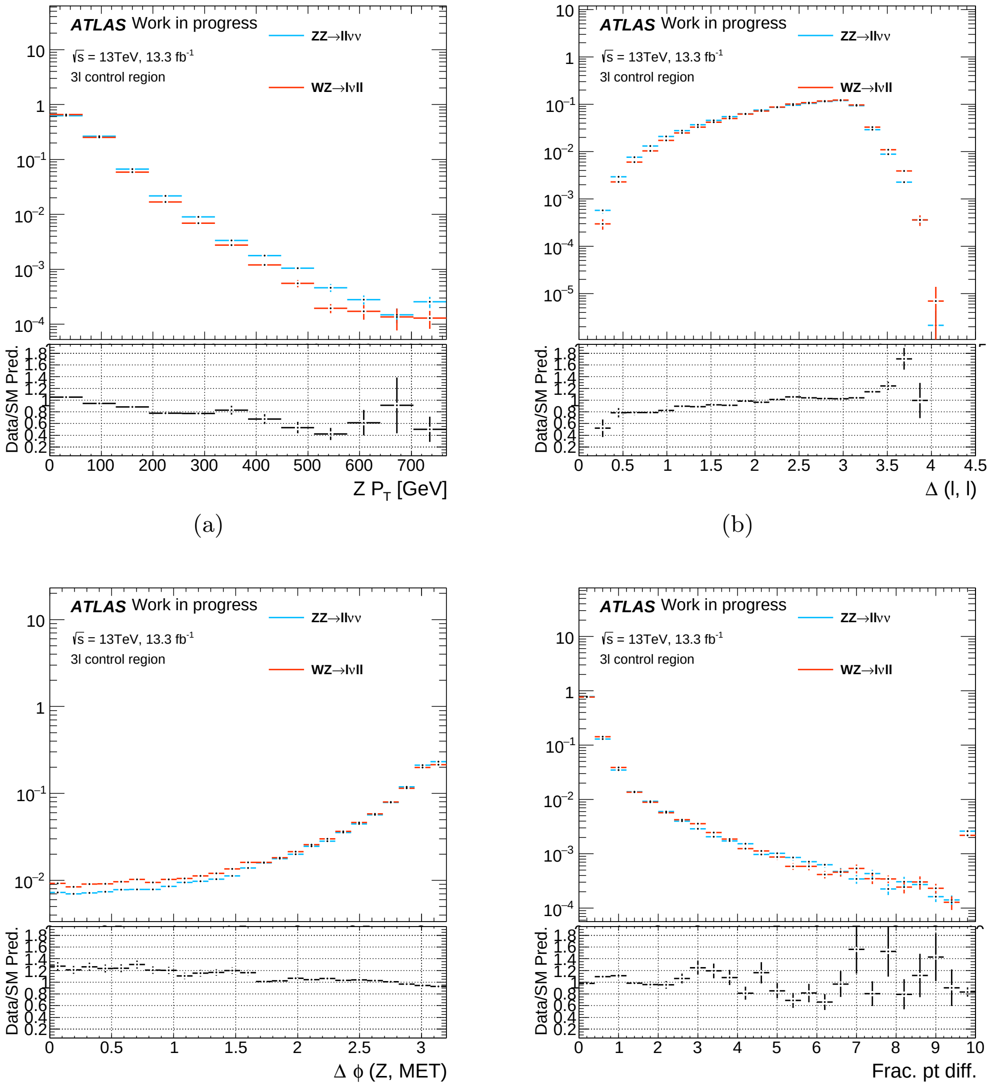

(a)

(b)

(c)

(d)

Figure B.4: $WZ \to \ell\nu\ell\ell$ in 3l-CR and $ZZ \to \ell\ell\nu\nu$ in signal region compared for (a) Z boson p_{T}, (b) $\Delta R_{\ell\ell}$, (c) $\Delta\phi(Z, E_{\mathrm{T}}^{\mathrm{miss}})$ and (d) fractional p_{T} difference. The events are applied with Z mass requirement and third-lepton veto.

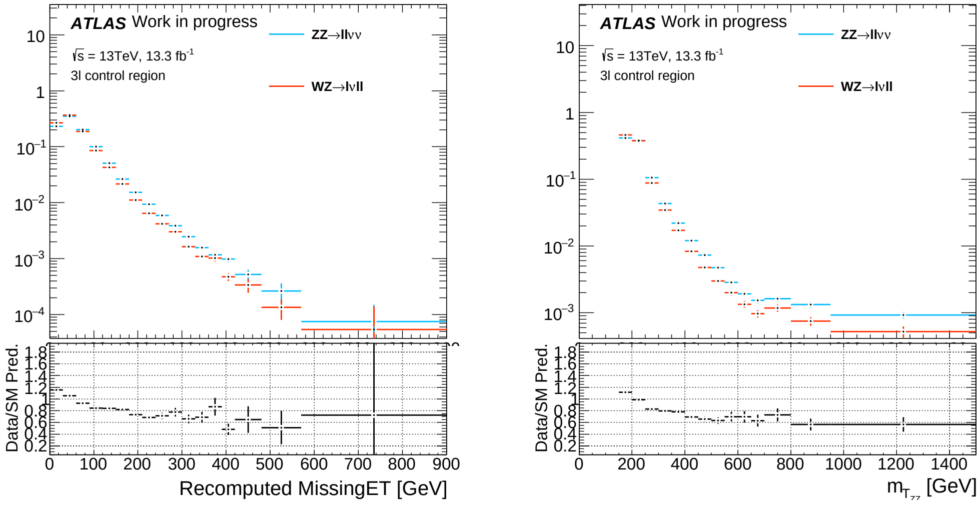

(a) (b)

Figure B.5: $WZ \rightarrow \ell\nu\ell\ell$ in 3l-CR and $ZZ \rightarrow \ell\ell\nu\nu$ in signal region compared for (a) $E_{\mathrm{T}}^{\mathrm{miss}}$ and (b) transverse mass of di-boson resonance. The events are applied Z mass requirement and third-lepton veto.

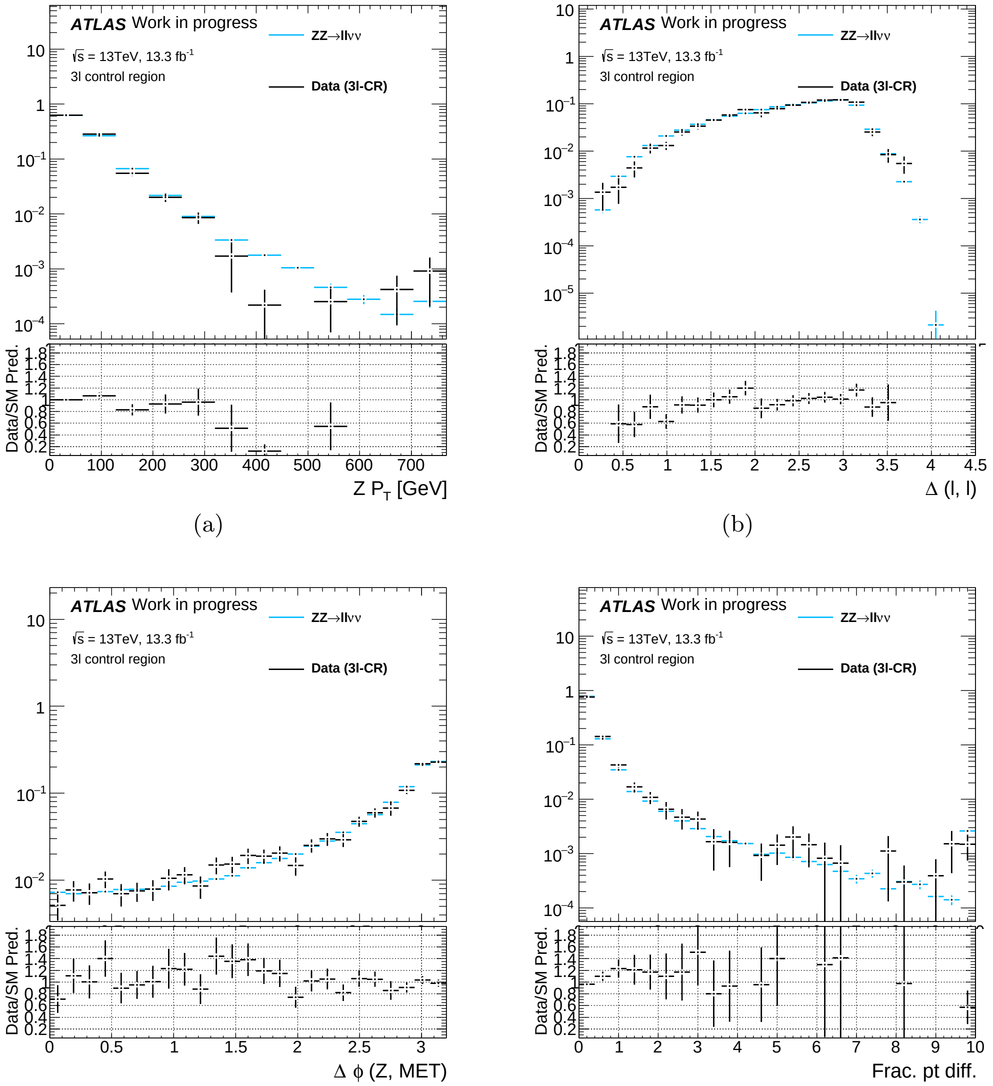

(a) (b)

(c) (d)

Figure B.6: The data in 3l-CR with all the MC contributions subtracted except for WZ process and $ZZ \to \ell\ell\nu\nu$ in signal region compared for (a) Z boson p_{T}, (b) $\Delta R_{\ell\ell}$, (c) $\Delta\phi(Z, E_{\mathrm{T}}^{\mathrm{miss}})$ and (d) fractional p_{T} difference. The events are applied Z mass requirement and third-lepton veto. Di-boson p_{T} re-weighting is applied.

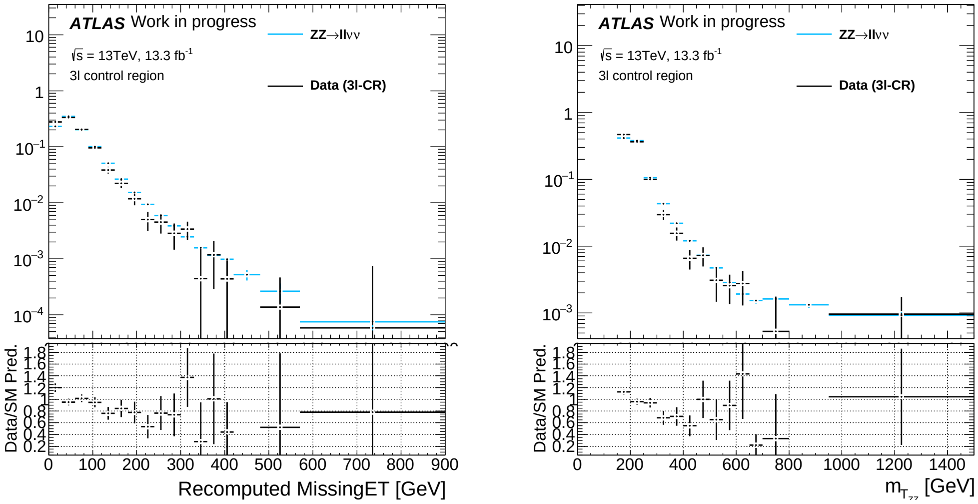

(a) (b)

Figure B.7: The data in 3l-CR with all the MC contributions subtracted except for WZ process and $ZZ \to \ell\ell\nu\nu$ in signal region compared for (a) $E_{\mathrm{T}}^{\mathrm{miss}}$ and (b) transverse mass of di-boson resonance. The events are applied Z mass requirement and third-lepton veto. Di-boson p_{T} re-weighting is applied.

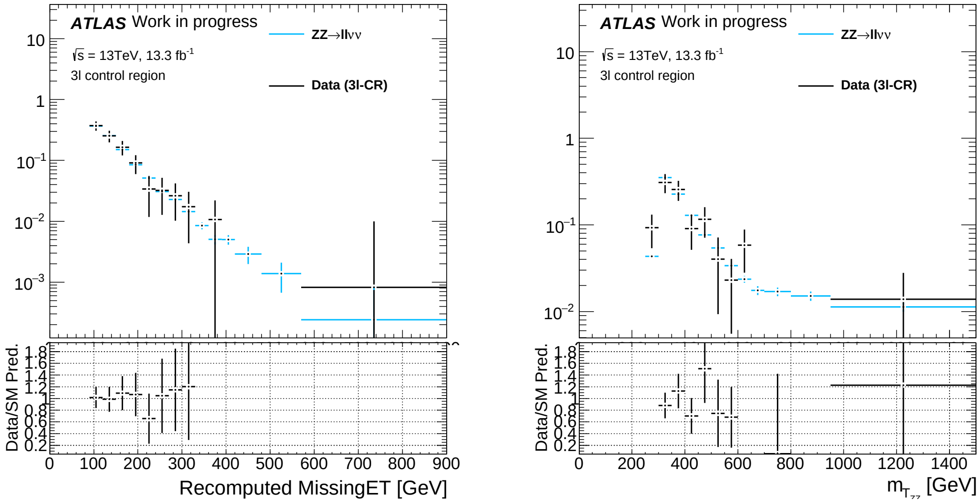

(a) (b)

Figure B.8: The data in 3l-CR with all the MC contributions subtracted except for WZ process and $ZZ \to \ell\ell\nu\nu$ in signal region compared for (a) $E_{\mathrm{T}}^{\mathrm{miss}}$ and (b) transverse mass of di-boson resonance with di-boson p_{T} re-weighting. For $E_{\mathrm{T}}^{\mathrm{miss}}$ distribution, all the dark matter searches event selections are applied. For m_T^{ZZ} distribution, all the ZZ resonance event selections are applied.

Appendix C

Study of $E_{\mathrm{T}}^{\mathrm{miss}}$ distribution in 90 - 100 GeV

Since we observe a sizable data/MC discrepancy in the $E_{\mathrm{T}}^{\mathrm{miss}}$ distribution, especially in 90 - 100 GeV bin, additional dedicated studies have been done to check the origin and the properties of these events.

C.1 Signal region plots for different period of Data

We split the data into two subsets : period A + B and period C + D, and check the kinematic distributions in these subsets. The results are shown in Figure C.1 for period A + B, Figure C.2 for period C + D. We observed a good data/MC agreement for period A and B only, slightly worse agreement for period C and D data. In data taking, period C and D tend to have higher pileup which may cause the data/MC discrepancy.

C.2 Events in first $E_{\mathrm{T}}^{\mathrm{miss}}$ bin

We studied the events with 90 GeV $< E_{\mathrm{T}}^{\mathrm{miss}} <$ 100 GeV to more detail checking the kinematic distribution. The results are shown in Figure C.3. Event excess comes in 0-jet bin, and the kinematics of these events are compatible with Z + jets events.

C.3 $ZH \rightarrow \ell\ell + inv.$ distribution excluding the events in the first $E_{\mathrm{T}}^{\mathrm{T}}$ bin

To evaluate how the excess in the first $E_{\mathrm{T}}^{\mathrm{miss}}$ bin affects the final results, we fit and derived the limit excluding the events in the first $E_{\mathrm{T}}^{\mathrm{miss}}$ bin. The resulting limits for the two cases are shown in Table C.1. No major differences is observed between the two cases.

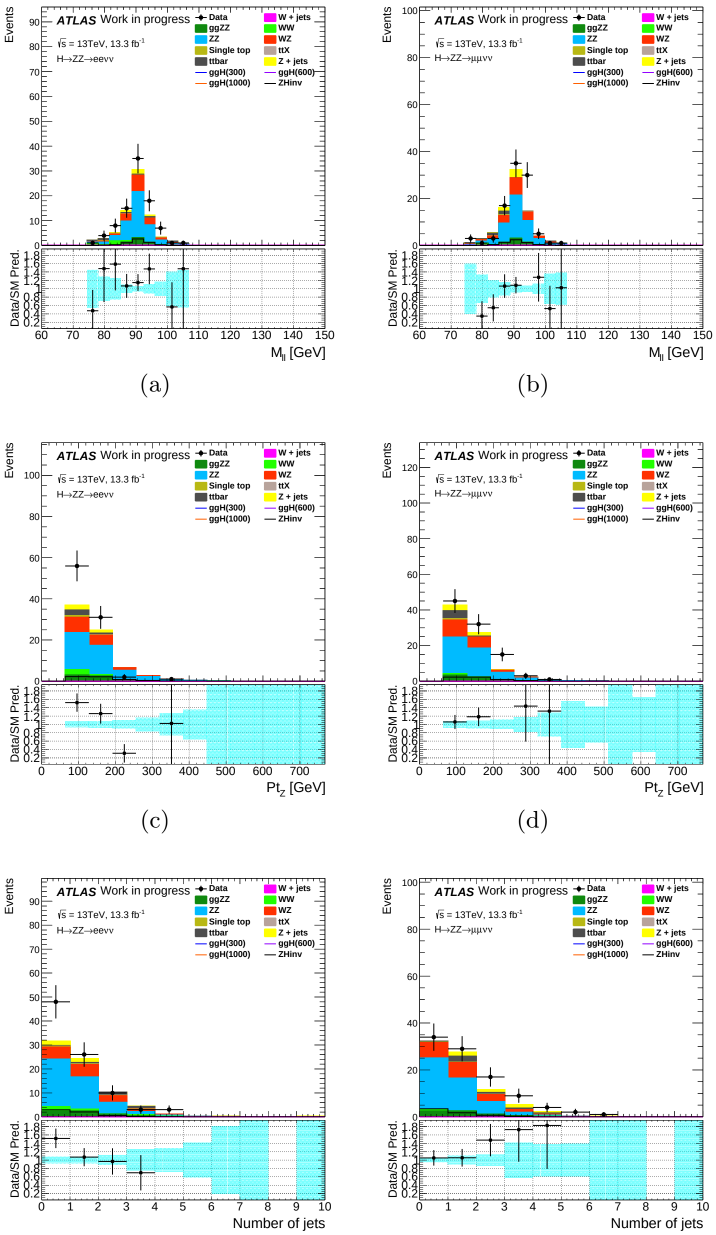

(a) (b)

(c) (d)

(e) (f)

Figure C.1: (a) and (b) Z mass distribution, (c) and (d) p_{T}^{Z} distribution, (e) and (f) number of jets distribution for ee and $\mu\mu$ channels, respectively after full event selection. The data are from 2016 period A and B. All the backgrounds are estimated from MC samples.

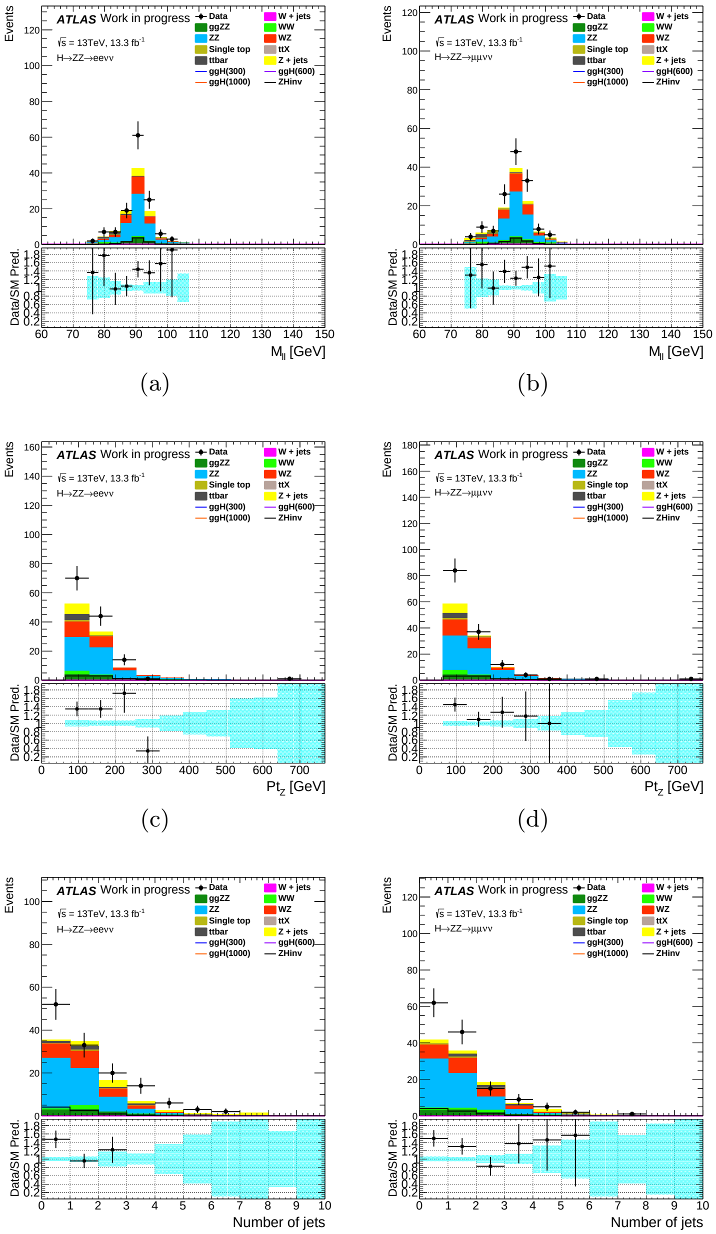

(a) (b)

(c) (d)

(e) (f)

Figure C.2: (a) and (b) Z mass distribution, (c) and (d) p_{T}^{Z} distribution, (e) and (f) number of jets distribution for ee and $\mu\mu$ channels, respectively after full event selection. The data are from 2016 period C and D. All the backgrounds are estimated from MC samples.

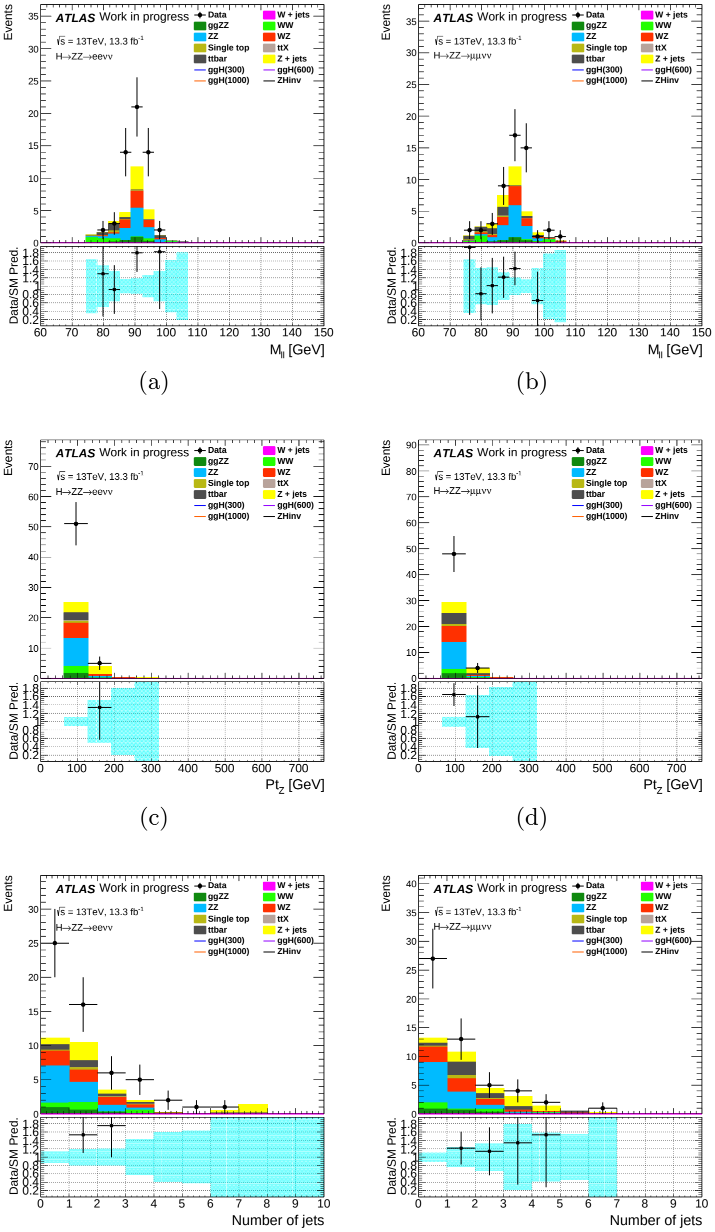

(a) (b)

(c) (d)

(e) (f)

Figure C.3: (a) and (b) Z mass distribution, (c) and (d) p_{T}^{Z} distribution, (e) and (f) number of jets distribution for ee and $\mu\mu$ channels, respectively after full event selection. All the backgrounds are estimated from MC samples.

Table C.1: The 95%CL upper limits on $BR(H \to inv.)$ for ee+$\mu\mu$ combined channel with the assumption of the Higgs boson is produced via SM $qq \to ZH$ process. The limits are derived in two cases: including events in first $E_{\mathrm{T}}^{\mathrm{miss}}$ bin and excluding. Both observed and expected limits are shown in table along with $\pm 1\sigma$ and $\pm 2\sigma$ error bands of expected limits. Both systematic uncertainties and statistical uncertainties are included in the fit.

Mass points	Exp. Limits	Exp. $+2\sigma$	Exp. $+1\sigma$	Exp. -1σ	Exp. -2σ	Obs. Limits
Include first $E_{\mathrm{T}}^{\mathrm{miss}}$ *bin*						
125 GeV	0.651103	1.28579	0.928875	0.460491	0.339554	0.982059
Exclude first $E_{\mathrm{T}}^{\mathrm{miss}}$ *bin*						
125 GeV	0.611507	1.21961	0.876266	0.432004	0.318242	0.976944

References

[1] A. Purcell, “A standard infographic for the standard model”, 2012, http://www.isgtw.org/spotlight/go-particle-quest-first-cern-hackfest.

[2] G. Aad *et al.*, “Observation of new particle in the search for the Standard Model Higgs boson with the ATLAS detector at the LHC”, Phys. Lett. B 716 (2012) 1.

[3] S. Chatrchyan *et al.*, “Observation of a new boson at a mass of 125 GeV with the CMS experiment at the LHC”, Phys. Lett. B 716 (2012) 30.

[4] K. G. Begeman, A. H. Broeils and R. H. Sanders, 1991, MNRAS, 249, 523.

[5] N. Jarosik *et al.*, “Seven-Year Wilkinson Microwave Anisotropy Probe (WMAP1) Observations: Sky Maps, Systematic Errors, and Basic Results”, arXiv:1001.4744v1 (2010).

[6] K. Sato and M. Kobayashi, Prog. Theor. Phys. 58 (1977) 1775.

[7] G. Branco *et al.*, “Theory and phenomenology of two-Higgs-doublet models”, Phys. Rept. 516 (2012) 1.

[8] G. Aad *et al.*, “Search for an additional, heavy Higgs boson in the $H \rightarrow ZZ$ decay channel at $\sqrt{s} = 8TeV$ in pp collision data with the ATLAS detector”, Eur. Phys. J. C 76 (2016) 45.

[9] James Stirling, “Parton luminosity and cross section plots”, http://www.hep.ph.ic.ac.uk/ wstirlin/plots/plots.html.

[10] L. Randall and R. Sundrum, “A Large mass hierarchy from a small extra dimension”, Phys. Rev. Lett. 83 (1999) 3370.

[11] E. Aprile *et al.*, “Dark Matter Results from 225 Live Days of XENON100 Data”, Phys. Rev. Lett. 109, 181301.

[12] A. Djouadi *et al.*, “Implications of LHC searches for Higgsportal dark matter“, Pyhs .Rev. Lett. B709 (2012) 6569.

[13] G. Aad *et al.*, "Constraints on new phenomena via Higgs boson couplings and invisible decays with the ATLAS detector", J. High Energ. Phys. (2015) 2015: 206. doi:10.1007/JHEP11(2015)206.

[14] J. Abdallah *et al.*, "Simplified Models for Dark Matter Searches at the LHC", Phys. Dark Univ. 8 (2015) 9.

[15] D. Abercrombie *et al.*, arXiv:1507.00966 [hep-ex].

[16] G. Aad *et al.*, "Search for new phenomena in final states with an energetic jet and large missing transverse momentum in pp collisions at 13 TeV using the ATLAS detector", Phys. Rev. D94 (2016) 032005

[17] L. Evans and P. Bryant, Lhc machine, Journal of Instrumentation, 3:S08001, 2008.

[18] J. Pequenao, Computer generated image of the whole ATLAS detector, 2008.

[19] G. Aad *et al.*, "ATLAS pixel detector: Technical design report", CERN-LHCC-98-13, 1998.

[20] G. Aad *et al.*, "ATLAS pixel detector electronics and sensors", JINST, 3 : P07007,2008.

[21] Capeans. M, Darbo. G, Einsweiller. K, Elsing. M, Flick. T, Garcia-Sciveres. M, Gemme. C, Pernegger. H, Rohne. O, Vuillermet. R, "ATLAS Insertable B-Layer Technical Design Report", https://cds.cern.ch/record/1291633.

[22] A. Abdesselam, T. Akimoto, P. P. Allport, J. Alonso, B. Anderson *et al.*, "The barrel modules of the ATLAS semiconductor tracker", Nucl. Instrum. Meth., A 568:642-671,2006.

[23] A. Abdesselam *et al.*, "The ATLAS semiconductor tracker end-cap module", Nucl. Instrum. Meth., A 575:353-389, 2007.

[24] E. Abat *et al.*, "The ATLAS Transition Radiation Tracker (TRT) proportional drifttube: Design and performance", JINST, 3:P02013, 2008.

[25] G. Aielli, A. Aloisio, M. Alviggi, V. Aprodu, V. Bocci *et al.*, "The RPC first level muon trigger in the barrel of the ATLAS experiment", Nucl. Phys. Proc. Suppl., 158:11-15, 2006.

[26] S. Majewski, Georges Charpak, A. Breskin, and G. Mikenberg, "A thin multiwire chamber operating in the high multiplication mode", Nucl. Instrum. Meth., 217:265-271, 1983.

[27] Theodoros Argyropoulos, Ketevi Adikle Assamagan, Brian Hugues Benedict, Valeri Chernyatin, Elliot Cheu *et al.*, "Cathode strip chambers in ATLAS : Installation, commissioning and in situ performance", IEEE Trans. Nucl. Sci., 56:1568-1574, 2009.

[28] F. Bauer, U. Bratzler, H. Dietl, H. Kroha, T. Lagouri *et al.*, “Construction and test of MDT chambers for the ATLAS muon spectrometer”, Nucl. Instrum. Meth., A 461:17-20, 2001.

[29] R. Blair, J. Dawson, G. Drake, W. Haberichter, J. Schlereth, J. Zhang, M. Abolins, Y. Ermoline, and B. Pope, “The ATLAS High Level Trigger Region of Interest Builder”, Journal of Instrumentation 3 110 no. 04, (2008) P04001.

[30] G. Aad *et al.*, “Muon reconstruction performance of the ATLAS detector in proton-proton collision data at $\sqrt{s}$ =13 TeV”, Eur. Phys. J. C76(2016) 292.

[31] G. Aad *et al.*, “Electron efficiency measurements with the ATLAS detector using the 2015 LHC proton-proton collision data”, ATLAS-CONF-2016-024.

[32] G. Aad *et al.*, “Selection of jets produced in 13TeV proton-proton collisions with the ATLAS detector”, ATLAS-CONF-2015-029.

[33] G. Aad *et al.*, “Optimisation of the ATLAS b-tagging performance for the 2016 LHC Run”, ATL-PHYS-PUB-2016-012.

[34] T. Cornelissen *et al.*, “The global χ^2 track fitter in ATLAS”, J. Phys. Conf. Ser. 119 (2008) 032013.

[35] M. Cacciari, G. P. Salam and G. Soyez, “The anti-kt jet clustering algorithm”, JHEP 0804 (2008) 063.

[36] G. Aad *et al.*, “Expected performance of the ATLAS b-tagging algorithms in Run-2”, ATLAS-PUB-2015-022 (https://cds.cern.ch/record/2037697).

[37] The G. Aad *et al.*, “Tagging and suppression of pileup jets with the ATLAS detector”, ATLAS-CONF-2014-018, 2014, url: http://cds.cern.ch/record/1700870.

[38] M. Cacciari and G. P. Salam, “Pileup subtraction using jet areas”, Phys. Lett. B659 (2008) 119126.

[39] M. Cacciari, G. P. Salam and G. Soyez, “The Catchment Area of Jets”, JHEP 0804 (2008) 005.

[40] G. Aad, *et al.*, “Measurement of $W^{\pm}$ and Z-boson production cross sections in pp collisions at $\sqrt{s}$ = 13 TeV with the ATLAS detector”, Physics Letters B 759 (2016) 601621.

[41] G. Aad *et al.*, “Performance of missing transverse momentum reconstruction for the ATLAS detector in the first proton-proton collisions at at $\sqrt{s}$= 13 TeV”, ATL-PHYS-PUB-2015-027.

[42] S. Agostinelli *et al.*, "GEANT4: A simulation toolkit, Nucl. Instrum. Meth". A506 (2003) 250.

[43] S. Alioli *et al.*, "NLO Higgs boson production via gluon fusion matched with shower in POWHEG", JHEP 04 (2009) 002.

[44] T. Sjostrand, S. Mrenna and P. Skands, "A Brief Introduction to PYTHIA 8.1", Comput. Phys. Comm. 178 (2008) 852.

[45] D. J. Lange, "The EvtGen particle decay simulation package", Nucl. Instrum. Meth. A 462 (2001) 152.

[46] H.-L. Lai *et al.*, "New parton distributions for collider physics", Phys. Rev. D 82 (2010) 074024.

[47] J. Alwall *et al.*, "The automated computation of tree-level and next-to-leading order differential cross sections, and their matching to parton shower simulations", JHEP 07 (2014) 079.

[48] G. Aad *et al.*, "ATLAS Pythia 8 tunes to 7 TeV data", ATL-PHYS-PUB-2014-021 (2014), url: http://cdsweb.cern.ch/record/1966419.

[49] R. D. Ball *et al.*, "Parton distributions for the LHC Run II", JHEP 04 (2015) 040.

[50] K. Hamilton, P. Nason and G. Zanderighi, "MINLO: Multi-scale improved NLO", JHEP 10 (2015) 155.

[51] S. Heinemeyer *et al.*, Handbook of the LHC Higgs cross sections: 3. Higgs Properties, CERN-2013-004 (2013), arXiv: 1307.1347 [hep-ph].

[52] S. Dittmaier *et al.*, Handbook of LHC Higgs Cross Sections: 1. Inclusive Observables, CERN-2011-002 (2011), arXiv: 1101.0593 [hep-ph].

[53] LHC Higgs Cross Section Working Group,
http://twiki.cern.ch/twiki/bin/view/LHCPhysics/CERNYellowReportPageAt13TeV.

[54] J. Alwall *et al.*, "MadGraph 5 : Going Beyond", JHEP 06 (2011) 128.

[55] P. Nason, "A new method for combining NLO QCD with shower Monte Carlo algorithms", JHEP 0411 (2004) 040.

[56] M. Grazzini, S. Kallweit, D. Rathlev, "ZZ production at the LHC: fiducial cross sections and distributions in NNLO QCD", Phys. Lett. B 750 (2015) 407.

[57] B. Biedermann *et al.*, "Electroweak corrections to $pp \to \mu^+\mu^-e^+e^- + X$ at the LHC - a Higgs background study", FR-PHENO-2016-002, ICCUB-16-003 (2016).

[58] N. Kauer and G. Passarino, "Inadequacy of zero-width approximation for a light Higgs boson signal", JHEP 08 (2012) 116.

[59] N. Kauer, "Interference effects for $H \to WW/ZZ \to \nu\bar{\nu}$ searches in gluon fusion at the LHC", JHEP 12 (2013) 082.

[60] C. S. Li *et al.*, "Soft gluon resummation in the signal-background interference process of $gg(\to h) \to ZZ$", JHEP 08 (2015) 065.

[61] M. Grazzini *et al.*, "$W^{\pm}Z$ production at hadron colliders in NNLO QCD", ZU-TH-15-16, MITP-16-037, NSF-KITP-16-046, DESY-16-074 (2016), arXiv: 1604.08576 [hep-ph].

[62] G. Aad *et al.*, "Measurements of $W^{\pm}Z$ production cross sections in pp collisions at $\sqrt{s} = 8$ TeV with the ATLAS detector and limits on anomalous gauge boson self-couplings", Phys. Rev. D 93 (2016) 092004.

[63] G. Aad *et al.*, "Measurement of the $W^{\pm}Z$ boson pair-production cross section in pp collisions at $\sqrt{s} = 13$ TeV with the ATLAS Detector", submitted to Phys. Lett. B (2016).

[64] ATLAS Muon Trigger Public Results Web Site,
https://twiki.cern.ch/twiki/bin/view/AtlasPublic/MuonTriggerPublicResults

[65] ATLAS Egamma Trigger Public Results Web Site,
https://twiki.cern.ch/twiki/bin/view/AtlasPublic/EgammaTriggerPublicResults

[66] F. Caola *et al.*, "QCD Corrections to ZZ Production in Gluon Fusion at the LHC", Phys. Rev. D92.9 (2015) 094028.

[67] F. Caola *et al.*, "QCD Corrections to W^+W^- production through fluon fusions", arXiv:1511.08617[hep-ph].

[68] Kirill Melnikov, Matthew Dowling, "Production of two Z-bosons in fluon fusion in the heavy top quark approximation", Phys.Lett.B 744 (2015) 43.

[69] Marco Bonvini, Fabrizio Caola, Kirill Melnikov, Giovanni Ridolfi, "Signal-background interference effects for $gg \to H \to W^+W^-$ beyond leading order", Phys.Lett.D 88 (2013).

[70] Sheng Li *et al.*, "Soft gluon resummation in the signal-background interference process of $gg \to h* \to ZZ$", JHEP (2015), arXiv:1504.02388v2[hep-ph]

[71] G. Aad *et al.*, "Constraints on the off-shell Higgs boson signal strength in the high-mass ZZ and WW final states with the ATLAS detector", Eur. Phys. J. C 75 (2015) 335.

[72] G. Aad *et al.*, "Improved luminosity determination in pp collisions at $\sqrt{s} = 7$ TeV using the ATLAS detector at the LHC", Eur. Phys. J. C 73 (2013) 2518.

[73] G. Aad *et al.*, “2015 start-up trigger menu and initial performance assessment of the ATLAS trigger using Run-2 data”, ATL-DAQ-PUB-2016-001 (2016), url: http://cdsweb.cern.ch/record/2136007.

[74] G. Aad *et al.*, “Jet Calibration and Systematic Uncertainties for Jets Reconstructed in the ATLAS Detector at $\sqrt{s} = 13$ TeV”, ATL-PHYS-PUB-2015-015 (2015), url: http://cdsweb.cern.ch/record/2028594.

[75] G. Cowan *et al.*, “Asymptotic formulae for likelihood-based tests of new physics”, Eur. Phys. J. C 71 (2011) 1554, [Erratum: Eur. Phys. J. C 73,2501(2013)].